Exploring Ultrafast Molecular Dynamics in Asymmetric Laser Fields

Kelsie Jean Betsch
Charlottesville, VA

B.A. Augustana College, 2005

A Dissertation presented to the Graduate Faculty
of the University of Virginia in Candidacy for the Degree of
Doctor of Philosophy

Department of Physics

University of Virginia
May, 2010

_____

_____

_____

_____

Abstract

We explore the effects of asymmetric laser pulses, those with a distinct, controllable difference in the up vs. down direction, on the combined electronic and nuclear dynamics of atomic and molecular processes such as nonsequential double ionization and multielectron dissociative ionization.

First, we use a two-color laser field to explore the directional fragment emission from multielectron dissociative ionization in N_2, O_2, CO, and CO_2. We find a robust, phase-dependent directional ejection of highly-charged fragments from asymmetric dissociation channels in all of these molecules. Moreover, after adopting an independent phase calibration, for all channels observed, the fragment with the highest ionization potential is preferentially emitted in the direction opposite to the laser field maximum. This is precisely opposite to predictions based on the standard model of enhanced ionization, although recent developments indicate that a sign error in the independent phase calibration may have been found.

In collaboration with a group of scientists lead by Dr. Matthias Kling at the Max Planck Institute for Quantum Optics (MPQ) in Garching, Germany, we develop a method to "tag" every < 5 fs laser pulse with the carrier-envelope phase, and demonstrate the effectiveness of this technique by studying the carrier-envelope phase dependence of nonsequential double ionization in argon. Using this method, we are able to extend data acquisition times to several days, greatly improving statistics, while requiring significantly less effort than traditional methods of phase stabilization.

With the use of two < 5 fs laser pulses in a pump-probe geometry, we, in collaboration with Dr. Kling's group at MPQ, study the dynamics of multielectron dissociative ionization in N_2 and O_2. We find evidence of electron localization into the $N_2(2,0)$ channel after ionization by the pump pulse followed by ionization of the neutral atom by the probe pulse in the delay-dependent production of the $N_2(2,1)$ channel. Similar electron localization and

ionization of the neutral is observed in the production of the $N_2(1,1)$ channel. Using the phase tagging technique, we find no statistically significant directional fragment emission from N_2 or O_2 when induced by few-cycle laser pulses.

Contents

List of Figures

List of Tables

Acknowledgements

First and foremost, I must thank my family. Thank you, Mom and Dad, for giving me the freedom to be a child and to explore at will. I honestly did grow up believing that I could be and do anything that I wanted to, and for encouraging that, I am grateful. Allie and Angie, it pleases me so much to see the both of you engaged in careers that you enjoy so. I hope that you have all the happiness and success that I have had.

I have had much help and company in the lab over the years, and I would be remiss not to thank those of you who have spent time with me in the lab. Dan and Brett, thank you for all that you taught me about the Chemistry lab before you left. Mary, I thank you for your words of wisdom and for the countless times that you said, "Oh, I understand". All the best to you and the pets. Greg, thank you for making me think like a chemist again.

A large portion of this work was performed in conjunction with the research group of Dr. Matthias Kling at the Max Planck Institute for Quantum Optics (MPQ) in Garching, Germany. A big thank you goes out to all of the group members at MPQ who made me feel more at home in three months than I thought possible: Oliver, Matthias Kübel, Frederik, Adrian, Boris, Yingying, Sergey, and Irina. Sarah and Simon, thank you for your cheerful help and the shared cups of tea.

Matthias, you have a quality that draws enthusiasm from people and brings your research group to life. Thank you for extending the opportunity to work with you and for making it so easy to share my ideas with you; I heartily enjoyed my time at MPQ.

Nora - we take the best data ever! After 5 years apart, it was great to work together again. I look forward to the next time... All the best to you and Matthias, now and for your future.

The staff in the Physics Department at UVA is wonderful. Chris, you are a font of wisdom and a visit with you was always refreshing. I would like to thank Dave for teaching me enough machining skills to impress my father. Tammie, Dawn, Suzie, and Beth - you make the department a friendly place do such a good job taking care of us physicists. Thanks for putting up with us! Patti, Gwen, Faye, Shawn and Bryan - you make the physics department work. Thank you for the work that you do.

I have a long list of teachers that have encouraged me throughout the past 20 years, and you have made me want to affect future students in the same way. Mr. Thimjon, the trig identities notecard from your class was with me when I took my graduate school qualifying exam. Dr. Moore, Dr. Duffy-Matzner, Dr. Hanson, Dr. Viste, and Dr. Weisshaar thank to for believing in the ability of undergraduate students and for providing me with the scientific

skills that I rely upon every day. I would like to thank Dr. Earl for the hand-written note that sold me on Augustana College. Dr. Wells. Eric. I *highly* doubt that I would be a physicist if it were not for you. Thank you for being a wonderful mentor and friend. Dr. Rick Marshall, it was a pleasure teaching for you. I learned so much about being a good educator from you, and I appreciate your friendship and expertise in all matters electronic.

Naturally, I would not be writing this today if it were not for the guidance of my research advisor, Dr. Robert Jones. Throughout the past five years, you have provided an exceptional environment of resources and opportunities, and I am very privileged to have been able to benefit from that. You are a good scientist, with high standards and lots of energy, which makes working for you a rewarding opportunity. Thank you.

Lastly, I must thank my husband Brady. You have been exceedingly supportive and patient throughout this whole adventure. Thank you for telling me all of the tough things that I needed to hear, especially when I did not want to hear them. Thank you for letting me complain to you and then helping me see the good side. Knowing that you are proud of me means more than I can ever tell you. The past 10 years have been wonderful, and I am excited to spend the future with you, wherever it may take us.

Funding for this research has been provided by the U.S. Department of Energy Basic Energy Sciences.

Chapter 1

Introduction

1.1 Motivations

Over the past few decades, the development of ultrashort laser pulses, those with durations on the picosecond (1 ps = 10^{-12}s) or femtosecond (1 fs = 10^{-15}s) timescale, has revolutionized the field of experimental atomic and molecular physics. The electric fields produced at the foci of these ps and fs pulses are on the same order as intra-atomic and intra-molecular fields, enabling the pulses to non-resonantly remove electrons and initiate complex intra-molecular dynamics. Ultrashort laser pulses have also made it possible to study the combined laser-induced electronic and nuclear dynamics occurring on the timescales of molecular dissociations. Recently, pulses with sub-5 fs duration have been reliably produced, allowing the study of dynamics in even the smallest, fastest diatomic molecules. It is also possible to tailor the electric fields of laser pulses to further dictate atomic ionization and molecular dynamics. A fundamental control knob is the relative electric field strength in the "up" vs. "down" direction. Application of such controlled, asymmetric laser fields to molecules has the ability to control the spatial emission of fragments and the localization of the electrons

in the dissociation process.

There are two common methods of creating asymmetric laser fields, i.e. those with a distinct, controllable difference in the electric field in the up vs. down directions. The first, developed within the past 10 years with the production of near-IR few-cycle laser pulses [1], exploits the asymmetric nature of few-cycle pulses. By locking and controlling the phase of each laser pulse, which requires tremendous effort and is limited in duration by the stability of the lock, this method has been used to study a wide range of atomic and molecular processes, such as attosecond (10^{-18}s) pulse generation [2], above threshold and non-sequential double ionization from atoms [3–5], and electron localization in the dissociation of H_2 [6–8] and CO [9].

A second method for creating asymmetric laser fields is to use a coherent superposition of light at a fundamental frequency, ω, and its second harmonic, 2ω. This method has the advantage of not requiring special efforts to create and stabilize few-cycle pulses. Above threshold ionization [10, 11], high harmonic generation [12, 13], the dissociation of singly charged fragments from small [14–19] and large molecules [20], and even field-free spatial orientation of molecules [21, 22] have all been investigated with two-color fields.

For the most part, the research involving molecular dissociations in asymmetric laser fields has focused on the simple molecule H_2 and its isotopologues, D_2 and HD, or emission of singly-charged ionic fragments. The theoretical study of these few-body systems is possible, although there is still an ongoing debate regarding the electron localization in and directional fragment emission from these systems [14–16, 23, 24]. Extending the study to the controlled production of highly-charged fragments from multielectron molecules coupled with the ability to time-resolve the dynamics may provide insight into the validity of commonly held notions about molecular dissociation processes.

1.2 Atoms in Laser Fields

When an atom is placed in a laser field, the optical field distorts the Coulombic potential well seen by the outermost electrons. Although the laser field oscillates at the frequency of the radiation, $f = \omega/2\pi$, as long as $\hbar\omega << \text{IP}$, where IP is the ionization potential of the atom, we can represent the laser-atom interaction at one specific instant in time as the sum of the atomic potential and a static field, as shown in Figure 1.1. (If the laser frequency does not satisfy the low frequency limit $\hbar\omega <<$IP, an electron will not have time to tunnel through the atomic potential within one optical cycle, and this model is invalid. This regime is discussed below.) The laser field has the effect of raising the atomic barrier on the upfield side and lowering it on the downfield side. If the laser field is sufficiently strong, the potential barrier may be lowered enough to allow the valence electron to either tunnel through or (for even higher field strengths) fly above the barrier. This tunnel- or "over the barrier" ionization mechanism is applicable if the frequency of the radiation is much lower than the Kepler frequency of the electron and the intensity is significantly greater than 10^{13} W/cm^2. Within this regime, the oscillating field can be thought of as changing slowly on the timescale of electronic motion, and the tunneling rate can be determined under quasi-static conditions using semi-classical methods. For a given electron energy, the tunnel ionization rate is remarkably well predicted by the formula developed by Ammosov, Delone and Kraĭnove [25]. The ADK tunneling rate, given below in Equation 1.1, is mostly determined by the ionization potential of the atom, IP, and the electric field strength of the laser, F:

$$\omega = \left(\frac{3e}{\pi}\right)^{1/2} \frac{Z^2}{(n^*)^{4.5}} \left(\frac{4eZ^3}{(n^*)^4 F}\right)^{2n^*-1.5} \exp\left(-\frac{2Z^3}{3(n^*)^3 F}\right) \tag{1.1}$$

where e is the electron charge, Z is the charge remaining on the ionic core, and $n^* = Z/\sqrt{2IP}$

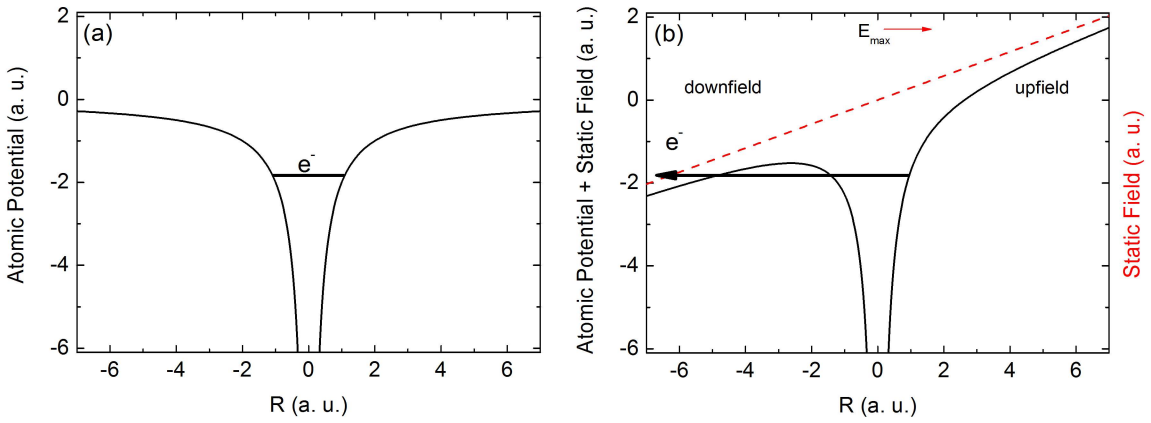

Figure 1.1: The potential well of (a) a bare atom and (b) an atom placed in a static field, which is a representation of the laser field at a particular instant in time. If the field is sufficiently strong, the electron may tunnel through or fly over the lowered barrier.

is the effective principle quantum number. Atomic units are used in Equation 1.1 and throughout the remainder of this dissertation, unless otherwise specified.

If the frequency of the radiation is too rapid to allow tunneling within the timescale of one optical cycle, the ionization is conveniently thought of as a multiphoton process. The electron absorbs many photons such that it then has enough energy to be free from the atomic potential. This is known as multiphoton ionization.

Today's laser technology extends into both the tunneling and multiphoton regimes, the boundary between which is determined by the Keldysh parameter [26], γ

$$\gamma = \omega \frac{\sqrt{2 m_e IP}}{eE} = \sqrt{\frac{IP}{2U_p}} \tag{1.2}$$

where ω is the angular frequency of the laser field, IP is the ionization potential of the atom, E and U_p are the strength and ponderomotive potential of the laser field, and e and m_e are the electron mass and charge, respectively. The Keldysh, or adiabaticity, parameter

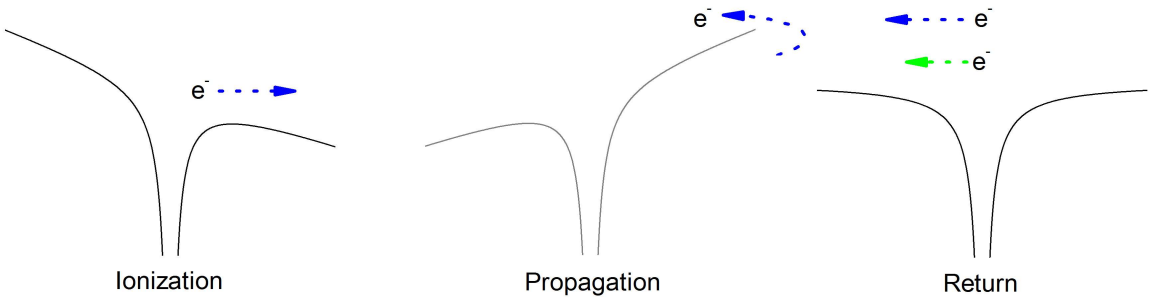

Figure 1.2: Cartoon outlining the three major steps leading to many phenomena of atoms in oscillating electric fields.

is essentially the ratio of the laser field frequency to the tunneling frequency; $\gamma >> 1$ is classified as the multiphoton regime, and $\gamma << 1$ as the tunneling regime.

Typically, after ionization, the electron will propagate away from the atomic core in the laser's electric field, as shown in the cartoon in Figure 1.2. In some instances, the electron will have acquired so much momentum that it breaks free of the atomic potential entirely, and has no further interaction with the core. However, for lower initial electron momentum, when the laser field switches direction, the electron may be turned around and accelerated back towards the atomic core. The mathematics behind electron ionization and propagation in an oscillating field are discussed in Appendix B. What happens upon the electron's return to the core dictates the subsequent process, be it high harmonic generation, above threshold ionization, or nonsequential double ionization.

1.2.1 High Harmonic Generation

If, upon its return, the electron recombines with the ionic core, it can emit a single photon with energy equivalent to the sum of the kinetic energy gained by the electron in the laser field and the ionization potential. This process is known as high harmonic generation (HHG) [27], and is a widely understood process and a common research topic [28].

1.2.2 Above-Threshold Ionization

One strong field atomic process that will be relevant to the work in this dissertation is above threshold ionization (ATI). In 1979, Agostini *et. al.* reported the first observation of discrete absorption of photons above the number necessary for ionization [29]. The electron energy spectrum consists of a series of discrete lines separated by the photon energy, $\hbar\omega$. In strong field multiphoton ionization (the first step in ATI), ionization can occur during each electric field cycle, and for a multicycle pulse, interference between ionization events in different optical periods results in discrete peaks in the electron energy spectrum. Ionized electrons may obtain multiple-10s of eV of energy after backscattering upon return to the ionic potential [30, 31]. These high-energy backscattered electrons will be used in the determination of the carrier-envelope phase of ultrashort pulses, described in Chapter 4. For a recent review of ATI, see [32].

1.2.3 Nonsequential Double Ionization

In the early 1980s, it was observed that, for linearly-polarized laser fields within a certain intensity regime, the rates of doubly-charged ion production from rare gas atoms were several orders of magnitude higher than expected from single-active-electron models assuming sequential removal of electrons [33, 34]. The first recoil-ion momentum distributions recorded in 2000 supported the theoretical idea that these anomalously high yields were explained by the recollision model [27, 35], in which the electron, when it returns to the ion core, uses its energy to liberate a second electron. This process, referred to as nonsequential double ionization (NSDI), is shown in the right most panel in Figure 1.2, and it will be studied in Chapter 4.

1.3 Diatomic Molecules in Laser Fields

Many of the basic phenomena occurring from atoms placed in laser fields, such as high harmonic generation and nonsequential double ionization, also occur for molecules in laser fields. However, molecules also exhibit vibrational and rotational motion, which adds structure and complexity to observed phenomena. For example, the yields from HHG in molecules can be increased if the molecular sample is pre-aligned with a weak laser pulse, making use of the rotational motion available in molecular samples. Additionally, after ionization, molecules can dissociate into constituent fragments. Laser-induced dissociation events have been studied for over two decades. Let us now consider some of the basic features, different from those in atoms, for diatomic molecules in laser fields.

Consider a diatomic molecule placed in a laser field. If the electric field is polarized perpendicular to the molecular axis, the potential well seen by an outer-shell electron is similar to that of an atom (see Figure 1.1). However, if the laser field is polarized along the internuclear axis, the laser field acts over the length of the molecule, and the potential well surrounding each nucleus is distorted, as in Figure 1.3a. At small internuclear separation (panel (a)), the inner potential barrier is far below the energy levels of valence electrons, so it has little effect and ionization is nearly atomic-like. As the internuclear distance is increased (e.g. the molecule is dissociating), the inner potential barrier is raised, eventually separating the molecule into two atoms (Figure 1.3c). The interplay between the internuclear separation and the laser field leads to some ionization effects not observed in atoms. For example, attempts to modify the atomic ADK tunneling rate for molecules have failed to produce uniformly good agreement with molecule-specific experimental observations [36].

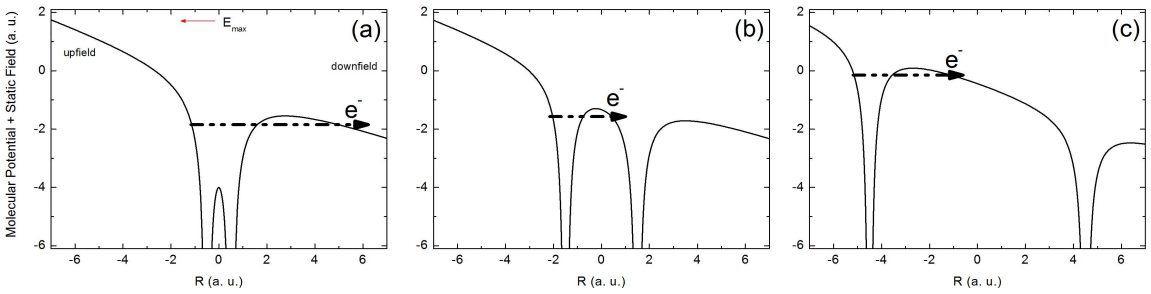

Figure 1.3: The double Coulomb potential of a diatomic molecule in an external laser field. (a) At small internuclear separation, the inner barrier is well below the electron's energy level, and the well looks atomic-like. (b) Increasing the internuclear separation raises the inner barrier, but the electron can still tunnel between the two wells. The ionization rate is enhanced over atomic-like rates due to suppression of the inner barrier by the neighboring atom. (c) At large internuclear separation, the electron can no longer tunnel through the wide inner barrier to the neighboring well, and ionization is again atomic-like.

1.3.1 Multielectron Dissociative Ionization

The simplest way to induce molecular dissociation is through absorption of a single photon. If the energy of a single photon is less than the ionization potential of the highest lying electron, $\hbar\omega < IP$, then the absorption of many electrons is required. When this first electron has been liberated, a dissociative potential curve may be populated, leading to the production of an atom plus a singly-charged ion. Dissociation can also occur if a large number of electrons are simultaneously torn away from the molecule while still at its equilibrium internuclear separation. Then, in a classical picture, the two positively charged ions strongly repel each other in a process hereafter referred to as Coulomb explosion. This process of multielectron dissociative ionization (MEDI) was first observed more than 20 years ago by using ps laser pulses to dissociate molecular nitrogen [37], and with the intense laser fields available from ps and fs lasers, it is common to observe the large kinetic energy release (KER) associated with MEDI and Coulomb repulsion.

Enhanced Ionization

While the kinetic energy releases are large, they are uniformly less than would be predicted by Coulomb repulsion at the equilibrium internuclear separation, R_e. A more sophisticated 2-step Coulomb explosion model was developed to explain this discrepancy [38, 39]. In the model, the laser field removes one or two electrons while the molecule is at R_e. The bond is now weakened, and the two nuclei begin to move apart. If the laser field is still present when the internuclear distance reaches a critical value, R_c, additional electrons are easily removed, and Coulomb explosion at R_c ensues. The rapid removal of electrons at R_c is facilitated by tunneling ionization through the inner potential barrier between the separating charges. This model, referred to as enhanced ionization (EI), has successfully explained the experimentally-observed reduced KERs [39], and pump-probe experiments have provided convincing evidence for the presence of enhanced ionization at R_c in molecular iodine [40]. The EI model will be a topic of discussion in Chapters 3 and 5.

It is also worth noting that molecules need not always dissociate into symmetric fragments. By definition, a heteronuclear diatomic will always produce two different fragments, and even a homonuclear diatomic can produce charge-asymmetric dissociation products. A molecule in the process of undergoing an asymmetric dissociation will experience different potential well distortions if the field is applied in one direction vs. the other, which is illustrated in Figure 1.4. The behavior of these asymmetric dissociation events induced by asymmetric laser fields will be discussed at length in Chapters 3 and 5. We now turn our attention to the nature of the asymmetric laser fields which we have used in the study of molecular dynamics.

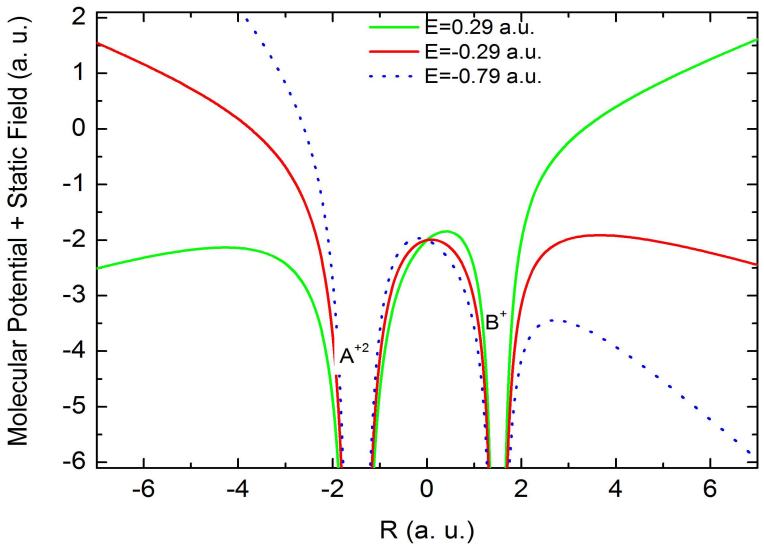

Figure 1.4: An asymmetric molecule in the presence of three fields. Increasing the field strength (red vs. dotted blue curves) lowers the outer the barrier significantly. Reversing the direction of the field (red and green curves) results in different heights of the inner and outer barriers. For a symmetric molecule, there would be no difference in the barrier heights from the green and red curves.

1.4 Asymmetric Laser Fields

A laser pulse is composed of two parts: the carrier wave, which oscillates with the frequency of the radiation, and the envelope, which governs the overall "shape" of the pulse. Typically, the time-dependent electric field of a linearly-polarized pulse can be represented mathematically as

$$E(t) = E_0(t)\cos(\omega t + \phi) \tag{1.3}$$

where $E_0(t)$ is the envelope function, ω is the angular frequency of the radiation, and ϕ is known as the carrier-envelope phase shift. For very long pulses, in which the envelope varies slowly compared to the frequency, the carrier wave oscillates many times within the pulse, and there is no inherent directionality to the field; the laser pulse would have equal peak amplitudes and spend the same amount of time pointing in the forwards and backwards directions. Such symmetric pulses lead to spatially symmetric atomic and molecular ionization and dissociation events.

However, laser pulses that have a preferred directionality, or a distinct, controllable difference in the electric field in one direction versus the other, are powerful tools for controlling atomic and molecular processes. In the static field picture, as in Figure 1.4, the electric field is now stronger in one spatial direction, further breaking the symmetry of the situation. We refer to such laser pulses as "asymmetric" laser fields. There are two primary ways to create asymmetric laser pulses. The first method stems from shortening the pulse duration, and the second method employs the mixing of two laser fields.

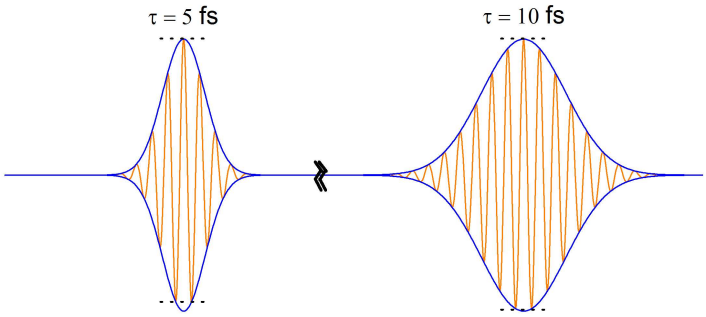

Figure 1.5: Few cycle 800 nm pulses of 5 fs and 10 fs duration. Increasing the pulse duration reduces the up/down asymmetry of the electric field.

1.4.1 Few-Cycle Pulses

Figure 1.5 compares an 800 nm laser pulse of two durations: 5 fs and 10 fs. From this, one can see that by decreasing the duration of the pulse, the difference in the maxima of the electric field in the up vs. down direction is increased. If the pulse duration is decreased so much as to allow only 2-3 oscillations of the carrier wave (one cycle of 800 nm light is 2.6 fs), the carrier-envelope (CE) phase, ϕ, which is illustrated in Figure 1.6, becomes a prominent factor controlling the electric field. By changing ϕ by π, the directionality of the field maximum is changed from up to down. In the intermediate case, $\phi = \pm\pi/2$, shown in the leftmost panel of Figure 1.6, the peak electric fields are the same in both directions, but multiple half-cycles of the field are often important in atomic and molecular processes, so even these *sine*-like pulses are of interest. Some of the technology required for few-cycle pulse generation and phase control is described in Chapter 2 and Appendix A.

1.4.2 Two-Color Laser Fields

Long before the technology for few-cycle pulses was developed, researchers had been creating asymmetric laser fields by combining a laser pulse at a fundamental frequency ω with its

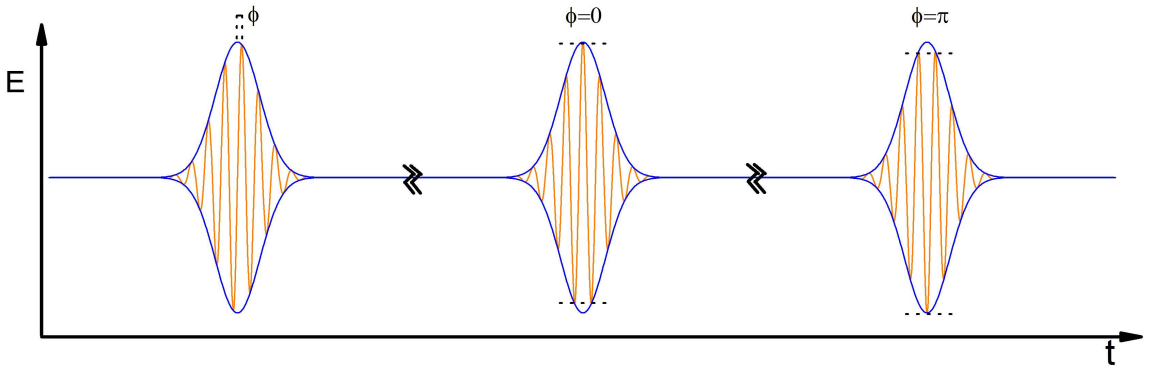

Figure 1.6: An 800 nm, 5 fs laser pulse for three values of ϕ, which is defined as the phase difference between the carrier wave (orange) and the envelope (blue) in the leftmost figure. The pulse envelope is assumed to be Gaussian. Changing ϕ by π reverses the directionality of the field.

second harmonic at frequency 2ω. A linearly-polarized two-color field takes the form

$$E(t) = E_\omega(t)cos(\omega t) + E_{2\omega}(t)cos(2\omega t + \phi), \tag{1.4}$$

where $E_\omega(t)$ and $E_{2\omega}(t)$ are the time-dependent pulse envelopes of the two components. Changing the relative phase between the fundamental and second harmonic, ϕ, by π reverses the direction of the maximum field, and a combination of ϕ and the ratio $E_{2\omega}/E_\omega$ controls the magnitude of the asymmetry. Figure 1.7 illustrates a 30 fs 800 nm + 400 nm two-color field for several values of ϕ.

One distinct advantage of the two-color field approach is the high degree of laser field asymmetry available. We can quantify the field asymmetry by defining the up vs. down laser field asymmetry as

$$\text{Field Asymmetry} = \frac{E^+_{max} - E^-_{max}}{E^+_{max} + E^-_{max}} \tag{1.5}$$

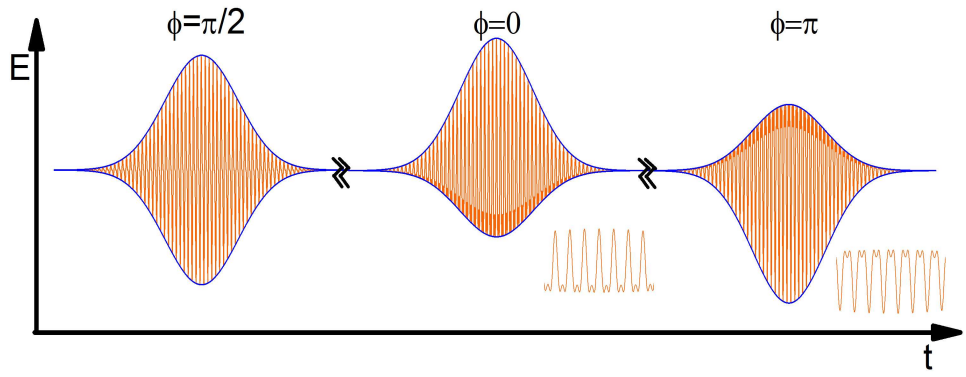

Figure 1.7: Two-color laser pulses for three different relative phases, ϕ, between the 800 nm and 400 nm components. The insets are expanded around the $t = 0$ (the peaks) for the $\phi = 0$ and $\phi = \pi$ pulses. $E_{2\omega}(t)/E_{\omega}(t)$=0.5.

where E^{+}_{max} and E^{-}_{max} are the peak amplitudes in the up and down directions, respectively. Figure 1.8a shows the laser field asymmetry for a two-color field for several second harmonic-to-fundamental electric field ratios, $E_{2\omega}/E_{\omega}$. $E_{2\omega}/E_{\omega} \geq 0.3$, or two-color field asymmetries ≥ 0.3, are readily achievable in the experiments described in this dissertation. The asymmetry of a few-cycle laser pulse drops off drastically as the duration increases, as shown in Figure 1.8b. The few-cycle, 750 nm pulses used in experiments in this dissertation fall close to $\tau = 2$, where τ is the pulse duration in units of optical cycles, and have a maximal field asymmetry of ≈ 0.03. This is a drastic reduction in laser field asymmetry compared to those available with two-color fields. However, the < 5 fs pulses have the advantage of being able to localize the asymmetry to a particular instant in time, and their short duration allows them to be used to time-resolve intra-molecular dynamics occurring on the ≈ 25 fs timescale, which are obscured by the two-color fields used in this work.

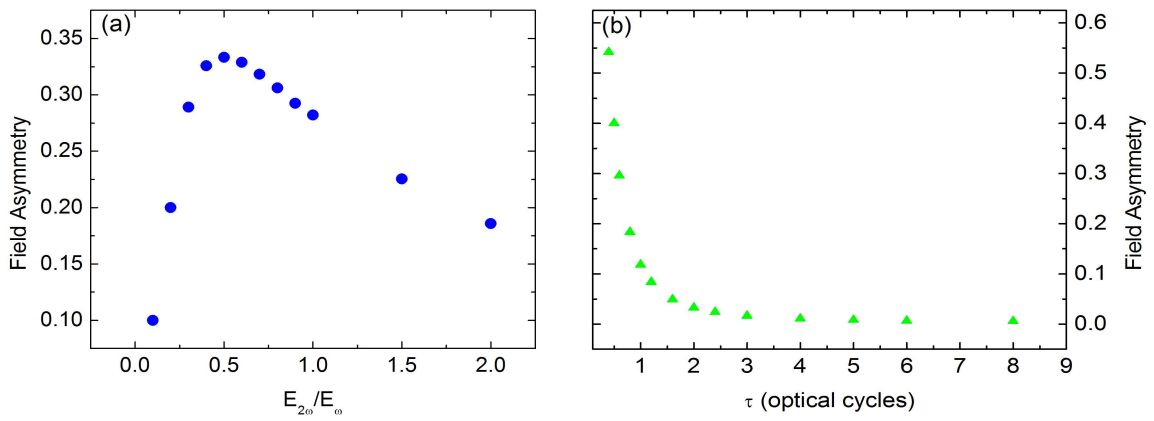

Figure 1.8: (a) The up vs. down laser field asymmetry, as defined by Equation 1.5, for a two-color pulse for several electric field ratios, $E_{2\omega}/E_{\omega}$. The relative phase, ϕ, is 0. (b) The up vs. down laser field asymmetry for a single-color pulse of varying durations. τ is the full-width half-max of the Gaussian field envelope in units of the optical cycle of the radiation.

1.5 Summary

This dissertation discusses several experiments involving the application of asymmetric laser fields to a variety of atoms and diatomic and triatomic molecules. First, Chapter 2 outlines the laboratory equipment necessary for the production of ultrashort laser pulses and the construction of ultrahigh vacuum chambers, in which the laser-matter interactions are explored. It also provides an introduction to the two techniques and three software packages used for data collection.

Secondly, in Chapter 3, we describe experiments involving molecular dissociations in two-color laser fields. The asymmetry of the field induces a strong directionality to the highly-charged fragments originating from N_2, O_2, CO and CO_2. An initial independent phase calibration suggests that the phase of the observed asymmetry was opposite to predictions based upon the EI model. More recent developments indicate that a π discrepancy in

this phase calibration may have been found, suggesting that the observed phase may be in agreement with the EI model.

The following two chapters address experiments involving the use of few-cycle laser pulses to probe electronic and nuclear dynamics. In Chapter 4, we describe a novel method of "tagging" each event with the carrier-envelope phase of the instigating ultrashort laser pulse. This technique is then applied to the study of nonsequential double ionization of argon atoms. Chapter 5 discusses experiments utilizing two ultrashort laser pulses in a pump-probe geometry to study the dynamics of molecular dissociations in N_2 and O_2. Evidence of charge localization into the $N_2(2,0)$ channel and subsequent ionization of the neutral atom is observed in the delay-dependent production of the $N_2(2,1)$ channel. The phase tagging technique is also used to study the origins of the laser-induced directional asymmetries observed in the two-color field experiments.

Chapter 2

Experimental Setup

2.1 Introduction

Two primary locations were used for the acquisition of the data presented in this dissertation. First of all, the resources in Room 204 of the Chemistry Building on the University of Virginia's Charlottesville campus were used to perform the long ($\sim$ 40 fs) pulse, two-color laser field experiments. Secondly, the resources at the AS-1 beamline located at the Max Planck Institute for Quantum Optics (MPQ) in Garching, Germany were utilized to perform the short ($\sim$ 5 fs), few-cycle pulse, pump-probe experiments. The principal elements of both experimental setups are similar and will be presented here. Relevant distinctions between the two configurations will also be addressed, and a complete summary of the resources available at each site can be found at the end of this chapter in Table 2.1.

2.2 Ultrashort Laser Pulse Production

Generation of the intense ultrashort laser pulses proceeds through a multi-step process known as chirped pulse amplification (CPA) [41]. Briefly, the light from a CW pump laser

is used to generate ultrashort, broad-bandwidth seed pulses in a laser oscillator. Then, one of these pulses is selected from the pulse train and temporally broadened. It, along with light from a second pump laser, then enters the laser amplifier, and the resulting output pulses are temporally compressed to as short as 20 fs. The basic components of the UVA and MPQ systems are the same; here, we will describe the UVA setup in detail, and the differences in the MPQ setup will be discussed briefly in Sect.2.2.9.

2.2.1 Verdi V-6

One of several pump lasers used in the production of ultrashort laser pulses, a Coherent Verdi V-6 is used to pump the Ti:Sapphire oscillator at each location. The Verdi is a solid-state, diode-pumped, neodymium-doped yttrium orthovanadate (Nd:YVO_4) continuous wave (CW) laser [42]. Inside the power supply, a laser diode bar is used to convert electrical power into laser light. The wavelength of this light is selected by temperature tuning of the diode bar to match the strong absorption band in the Nd ions inside the vanadate host crystal. Light from the diode bar is transmitted through a fiber optic cable assembly to the laser head, where it is inserted into the end-pumped ring cavity. In this design, light from the diode bar propagates along the optical axis of the gain medium, and one distinct benefit is the single-mode (TEM_{00}) laser output, which is crucial if the oscillator is to be carrier-evelope phase locked. A small fraction of the light at the fundamental wavelength of 1064 nm is frequency doubled in a lithium triborate (LBO) crystal. By controlling the temperature of the LBO crystal, the phase matching condition can be reached and the second harmonic generation process optimized, producing a beam of light at 532 nm containing up to 6.50 W of CW light. Typically, the diode current is set such that the output power is approximately 5.50 W, all of which is used to pump the Ti:Sapphire oscillator.

2.2.2 Evolution-30

We employ an Evolution-30 manufactured by Positive Light, Inc. [43], another diode-pumped solid state laser, as an optical pump for the Ti:Sapphire crystals in the ultrafast laser amplifier. The laser gain medium, neodymium-doped yttrium lithium fluoride (Nd:$LiYF_4$ or Nd:YLF) is pumped by twelve aluminum gallium arsenide (AlGaAs) laser diode arrays. Much like the Verdi V-6, the strong transition of the gain medium lies in the near infrared region of the optical spectrum and lases at 1053 nm, and a temperature-controlled LBO crystal is used to frequency double this light. The laser cavity is acousto-optically Q-switched at a rate of 1 kHz via a trigger from an external DG535 Digital Delay/Pulse Generator [44] that is synchronized to the oscillator pulse train. After exiting the cavity through a dichroic mirror, the laser output consists of a train of 200 ns pulses at 527 nm with up to 20 mJ of energy per pulse.

2.2.3 Ti:Sapphire Oscillator

In the UVA setup, a Ti:Sapphire-based Femtosource Scientific s200 oscillator from Femtolasers [45], pumped by the Verdi V-6, generates the ultrashort laser pulses used to seed the multipass amplifier. Specially designed chirped multilayer dielectric mirrors are used for broadband intra-cavity group-delay-dispersion (GDD) control, obviating the need for intracavity prisms, and, thus, allowing for shorter pulse duration and improved quality and stability. As shown in Figure 2.1, one of the mirrors inside the laser head is mounted on a piezoelectric transducer which, in conjunction with a series of electronics modules, allows for the possibility of locking the laser repetition rate. Once self-modelocking is initiated, the oscillator produces pulses approximately 26 fs in duration at a repetition rate of 200 MHz with a bandwidth of 36 nm centered at 795 nm. The typical per-pulse energy is 3-4 nJ

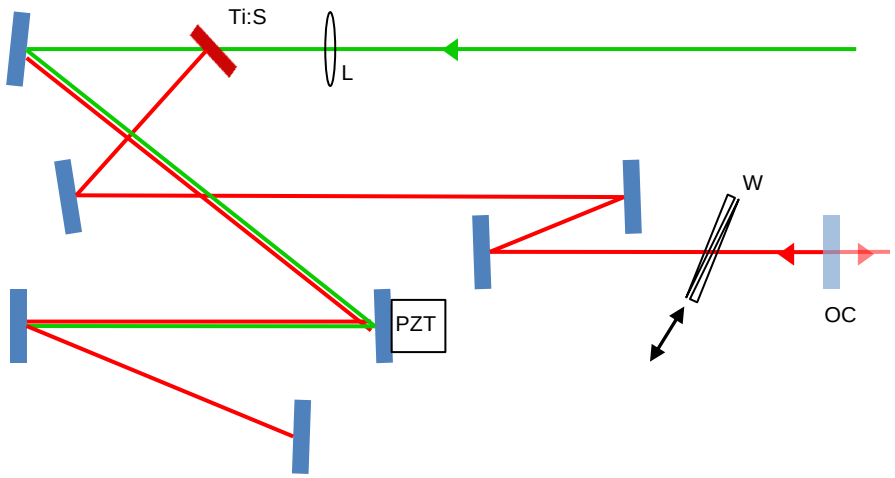

Figure 2.1: Layout of the Femtosource Scientific s200 Oscillator. L: lens, Ti:S: Titanium-sapphire crystal, PZT: piezoelectric transducer, W: glass wedges, OC: output coupler.

/ pulse. Approximately 30% of this light is diverted by a beamsplitter and can be focused into a photonic crystal fiber followed by a nonlinear f-to-2f interferometer [46] to create the optical signal for carrier-envelope phase (CEP) locking. The remaining light provides the seed light for the 30 fs laser amplifier. Neither the repetition rate nor the CEP locking techniques were utilized for the few-cycle or two-color measurements. For further discussion regarding the implementation of these techniques, see Appendix A.

2.2.4 Grating Stretcher

Due to their damage thresholds, the optics in the multipass amplifier cavity cannot amplify such a (temporally) short pulse as the oscillator provides. To avoid such damage, the seed pulse is temporally lengthened, or "chirped," by several orders of magnitude from its initial 26 fs duration and then sent into the amplifier cavity. After amplification, the pulse

is temporally compressed to the nominal 40 fs duration. This commonly used three-step process is known as chirped pulse amplification (CPA) [41]. A grating-based stretcher from KMLabs [47] is used to provide the temporal broadening for the CPA scheme. Figure 2.2 gives an overhead view of the stretcher layout. The seed beam diffracts from a grating which spatially separates the frequency components present in the light. Then this spatially dispersed light is reflected by a curved mirror to collimate the light, folded back upon itself, and reflected off of the grating again. A retro-reflecting mirror sends the light back through the same path, where the grating now reassembles all of the frequencies into the original spatial mode. Slightly different path lengths for the "redder" and "bluer" frequencies result in their temporal separation at the output, with the red frequencies arriving ahead of the blue. Temporal separation due to the group velocity dispersion adds "linear chirp" to the pulse; when the redder frequencies arrive before the bluer frequencies, this is called a "positive chirp." This specific stretcher can pass a bandwidth from 720 nm to 880 nm, and it stretches our initial 26 fs pulse to approximately 300 ps.

2.2.5 Pockels Cell

A laser amplifier is used to generate higher-energy pulses at a lower (kHz-level) repetition rate than that at which the oscillator runs. This is done by selecting only one out of every 200,000 of the oscillator pulses for amplification. By polarizing the oscillator pulses vertically, then using a brief application of high voltage to a Pockels cell [48] to rotate the polarization of one pulse by 90° followed by a polarizer to separate out the un-rotated pulses, only one oscillator pulse is passed into the amplifier cavity. If one places the Pockels cell before the grating stretcher, one can take advantage of the reduced grating efficiency for vertically polarized light, further increasing the extinction of unwanted pulses.

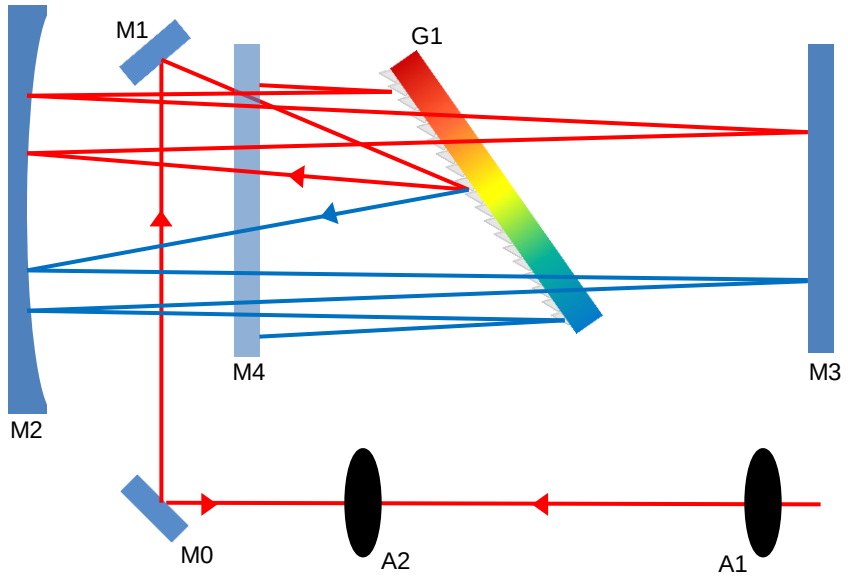

Figure 2.2: Schematic of the grating stretcher, as viewed from the top. A1,A2: apertures for alignment purposes, M0,M1: steering mirrors, G1: grating, M2: curved mirror, M3: fold mirror, and M4: retro-reflecting mirror. The beam path is A1, A2, M0, M1, G1, M2, M3, M2, G1, M4, G1, M2, M3, M2, G1, M1, M0, A2, A1. The retro-reflected beam is slightly lower than the incoming beam, and the transparency of M4 and G1 is to indicate that the beam passes above, and not through, these optics [47].

2.2.6 Laser Amplifier

The home-built laser amplifier consists of two stages: a multipass cavity followed by a bowtie-shaped linear amplifier. Pump light at 527 nm from the Evolution pump laser and the temporally chirped seed pulses from the oscillator are focused into the Ti:Sapphire crystal of the multipass amplifier. Pulses circulate in this cavity 8 times (four of which are illustrated in Figure 2.3) before they exit the cavity and enter the linear amplifier. A mask consisting of an array of holes spatially filters the beam after each pass to eliminate the unwanted effects of thermal lensing. Two series of $\lambda/2$ plates and polarizing beam splitters allow for control of the amount of pump light sent into each amplifier. After two passes through the linear amplifier crystal, the laser power is increased by a factor of two over that exiting from the multipass amplifier. A telescope composed of two curved mirrors adjusts the exiting laser beam to be slightly diverging as it exits the laser amplifier.

2.2.7 Grating Compressor

The third stage in the CPA scheme is temporal compression of the chirped, amplified pulse. For this task, we use a grating-based compressor, also from KMLabs [47], that is designed to complement our stretcher. Figure 2.4 depicts the overhead view of the compressor design. A simple grating pair now imparts a negative chirp to the pulse, and by tuning the relative angle between the gratings in the stretcher and compressor, one can compensate for second order dispersion in the system. With this angle set, one can change the distance between the gratings inside the compressor to compensate for linear chirp, resulting in output pulses of approximately 40 fs duration at a repetition rate of 1 kHz. Due to the gratings, the compressor has an efficiency of 50-60%. Typical output laser energy, as measured after the compressor, is 0.57 mJ/pulse from the multipass amplifier only and 1.2 mJ/pulse with the

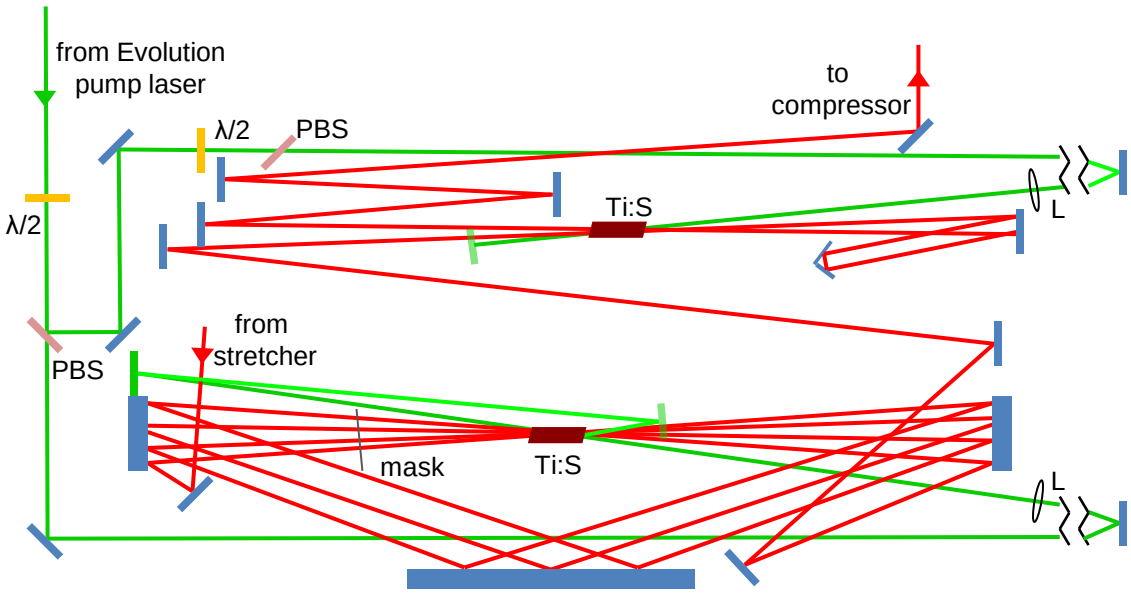

Figure 2.3: Overhead view of the multipass and bowtie amplifier. Ti:S: Ti:Sapphire crystal, L: lens, $\lambda/2$: half-wave plate, PBS: polarizing beam splitter. Some angles are enlarged and only half of the passes around the multipass cavity are illustrated for visibility. The green pump beam paths are continuous, although they are broken in this figure to save space, as indicated by the vertical "Zs".

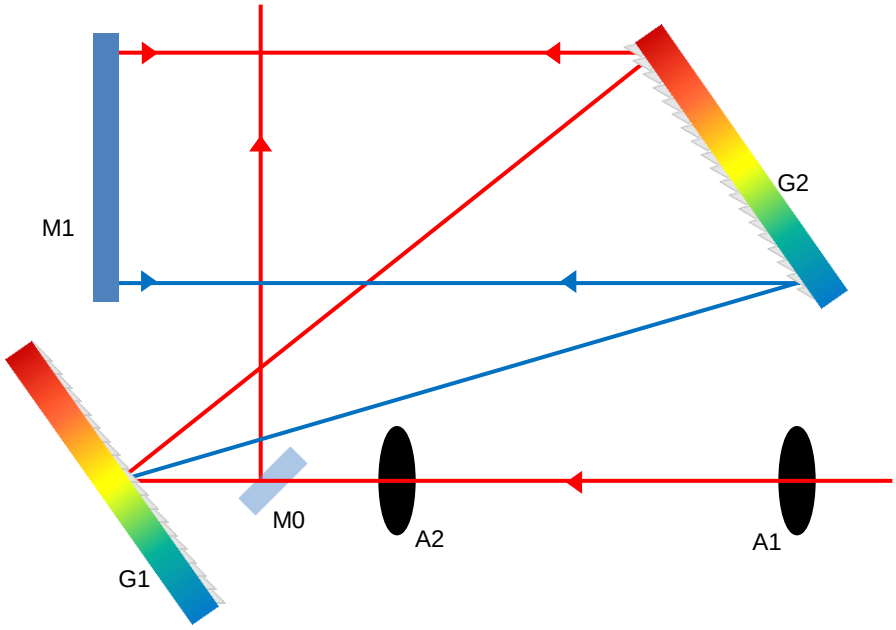

Figure 2.4: Schematic of the grating compressor, as viewed from the top. A1,A2: apertures for alignment purposes, M0: pickoff mirror, G1, G2: gratings, and M1: retro-reflecting rooftop mirror. The beam path is A1, A2, G1, G2, M1, G2, G1, M0. The retro-reflected beam is lower than the incoming beam, and the transparency of M0 is to indicate that the beam passes above, and not through, this mirror [47].

linear amplifier operating at peak performance.

2.2.8 Timing Electronics

In order to achieve amplification in the laser amplifier, it is crucial that the pump and seed laser pulses arrive in the Ti:Sapphire gain medium at specific times. To ensure correct timing, a photodiode collects the 200 MHz optical signal from the oscillator pulse train, and a series of signal amplifiers and frequency dividers is used to derive a 1 kHz master trigger signal suitable for externally triggering the DG535. First, the photodiode signal is amplified with a SRS SR445 DC-300 MHz amplifier. After passing through a BLP-300

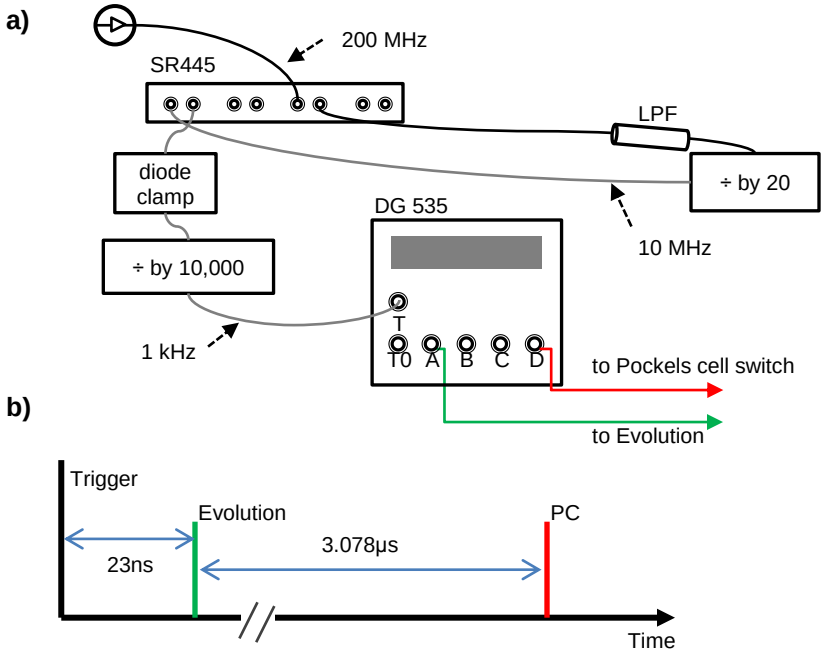

Figure 2.5: a) Block diagram of the master laser trigger creation at UVA. The pulse frequencies at various stages are indicated by dashed arrows. The triangle inside a circle represents a photodiode, and the SR445 is a four-channel amplifier, as indicated by the spacing of the pairs of input and output ports. LPF: low pass filter. b) Timing diagram for Evolution (green) and Pockels cell (PC, red) triggers, as sent by the DG535.

low-pass filter from Mini Circuits, the signal is sent through a home-built frequency divider that divides the signal down to 10 MHz. The 10 MHz signal is amplified again and sent through a diode clamp which restores any DC offset that the signal may have. Finallly, a PRL-230 frequency divider from Pulse Research Labs (Model PRL-230) divides the signal by 10,000. This 1 kHz signal provides the master trigger for the DG535, which is then used to create the appropriate delays between trigger pulses sent to the Evolution and the Pockels cell switch. A block diagram and timing scheme can be found in Figure 2.5.

2.2.9 AS-1 Beamline at MPQ

While the basic idea of the laser system at the AS-1 beamline at the Max Planck Institute for Quantum Optics is the same as in the Chemistry lab at UVA, there are differences in the design specifics. At AS-1, the chirped pulse amplification system is the Femptopower compact Pro system from Femtolasers [49]. The oscillator generates sub-12 fs pulses with bandwidth >100 nm at a repetition rate of 78 MHz. A compact glass rod-based, rather than a larger, grating-based, stretcher is used to chirp the pulses, before propagation into the single-stage 9-pass amplifier, which is pumped by a Nd:YLF pump laser at 527 nm from Photonics Industries [50]. All of the pulses propagate around the amplifier cavity four times, and after the fourth pass, the beam is sent through a Pockels cell to select only one pulse for further amplification. This design helps to minimize the amount of amplified spontaneous emission (ASE) present in the output pulse. After amplification, a prism-based compressor, chosen because it is less lossy than grating-based compressors, is used to compress the pulse duration to 30 fs. Typical operation yields ∼1 mJ/pulse at a repetition rate of 3 kHz. Further pulse compression down to 20 fs is achieved with a set of chirped mirrors.

At this point, the laser pulses are focused into a 1 m long neon-filled hollow core fiber (HCF, inner diameter: 250 μm; 3.2 bar Ne gas) where they are spectrally broadened through self phase modulation (SPM) [51]. This process also adds chirp to the pulses, so a set of 8 multilayer dielectric dispersion compensating mirrors is used to temporally compress the pulses. As is illustrated in Figure 2.6b, many layers of dielectric material are deposited on the mirror substrate, each of which reflects a certain wavelength of light, thereby increasing the optical path length of the long-wavelength components of the pulse. By adjusting the number of reflections, the positive chirp imparted by the SPM process, as well as from other optical elements in the beam path, can be compensated for. Daily fine-tuning of the chirp

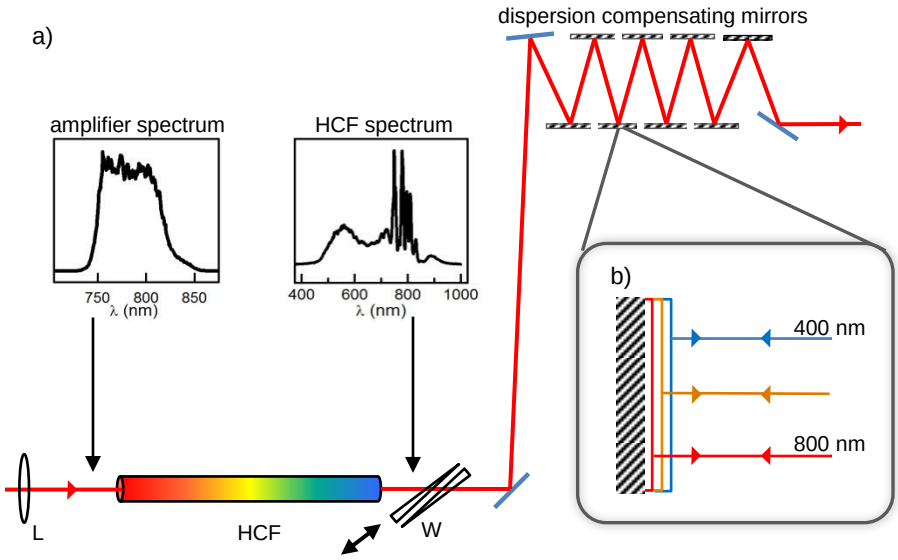

Figure 2.6: a) Schematic of the hollow core fiber and chirped mirror compressor at MPQ. b) Illustration of the group delay compensating mirrors. HCF: hollow core fiber; L: lens; W: glass wedge.

is achieved by varying the amount of glass in the beam path with a moveable wedge. The spectrum of the output pulses covers the range from 450 to 950 nm, and pulse durations of 4-5 fs and energies of 0.4 mJ are easily achievable provided the coupling of the beam into the HCF is properly stabilized with an active feedback loop [52].

2.2.10 Laser Pulse Diagnostics

Once the laser pulses are created, we use several instruments to monitor pulse characteristics such as duration, spectrum, and chirp. These instruments are based primarily upon the grating spectrometer.

Grating Spectrometer

Prior to amplification, a small amount of light from the Femtosource Ti:Sapphire laser oscillator in the UVA Chemistry lab is directed into a grating spectrometer, illustrated in Figure 2.7. The spectral components are spatially dispersed by the grating and imaged by a line camera. Saturation of the line camera is avoided by covering the narrow (50 μm wide) entrance slit with neutral density filters. By using this geometry and an array-type detector, each spectral component is collected for every laser shot. Viewing the camera output on an oscilloscope allows daily monitoring of the intensity spectrum, including central frequency and bandwidth, of the seed laser pulses. This same grating spectrometer can also be used to measure the spectrum of the amplified laser pulses.

Several miniature USB spectrometers from Ocean Optics [53] are used at MPQ. Fundamentally, the optics are the same, but light is coupled into the spectrometer via a fiber optic cable pointed at the light source, and the spectrum is displayed on a PC.

Single Shot Autocorrelator

Routine monitoring of the temporal duration of the pulses output from the hollow core fiber at MPQ is performed with a single-shot autocorrelator [54], illustrated in Figure 2.8. A small portion of the light is split, creating two beams that are then crossed inside a frequency doubling crystal. This crossed geometry results in a temporal delay between the two pulses which varies along the spatial axis transverse to the beam propagation. Second harmonic generation (SHG) occurs when portions of the two beams overlap spatially and temporally inside the crystal, so the temporal delay results in a spatial intensity distribution of the generated second-harmonic beam. Imaging this spatial intensity variation by a CCD camera thus illustrates the temporal width of the input pulse. The diameter of the SHG

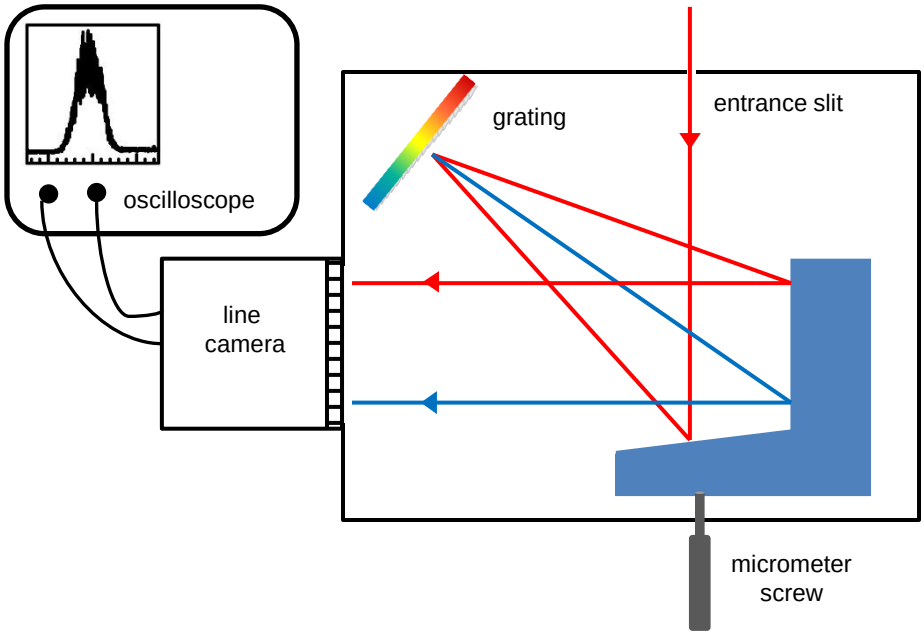

Figure 2.7: Grating spectrometer geometry. Turning the micrometer screw adjusts the position of the spectral components on the line camera.

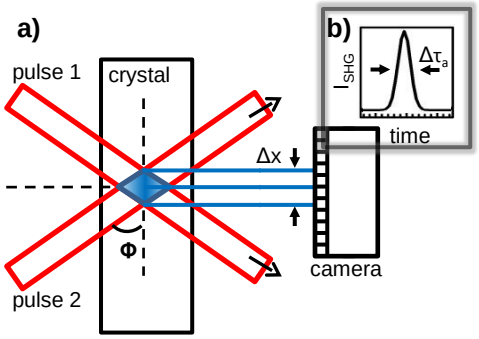

Figure 2.8: a) In the single-shot autocorrelator, each laser pulse is split into two pulses, which are then crossed inside a non-linear crystal. Light at the second harmonic is generated when the two pulses arrive inside the crystal at the same location and time. The crossed geometry results in a spatially varying SHG signal. b) An example autocorrelation trace illustrating the relationship between beam width and pulse duration.

beam, Δx, is related to the width of the autocorrelation trace, $\Delta\tau_a$, via

$$\Delta x = \frac{\Delta\tau_a v_g}{\sin\Phi} \tag{2.1}$$

where v_g is the pulse's group velocity and 2Φ is the crossing angle of the beams [54].

Frequency Resolved Optical Gating (FROG)

While the single-shot autocorrelator is a convenient way to monitor the pulse duration, it is unable to provide phase information, such as possible chirp, about the pulse. Trebino and coworkers [55] developed a family of techniques that provide both pulse duration and phase characteristics, known as Frequency Resolved Optical Gating (FROG). At UVA, we use a FROG apparatus based upon second harmonic generation (SHG FROG), which is a direct combination of the single-shot autocorrelator and the grating spectrometer. With the output from a 2-dimensional CCD camera imaged on a small television screen, we see a frequency-versus-delay spectrogram of the pulse shape in real time. The FROG is used to optimize the grating separation in the compressor to achieve the shortest pulse duration and to optimize the relative angles of incidence in the stretcher and compressor to minimize third order spectral dispersion. The camera output can also be sent to a computer, where the beam information is captured using Spiricon's LBA-PC software [56], and then an iterative phase retrieval program from Femtosoft Technologies [57] can be used to recover the time-dependent electric field, E(t), of the pulse.

2.3 Ultra High Vacuum Chambers

Atomic and molecular studies require laser light/matter interaction regions that contain only high purity target species. Thus, we employ stainless steel ultra high vacuum chambers to

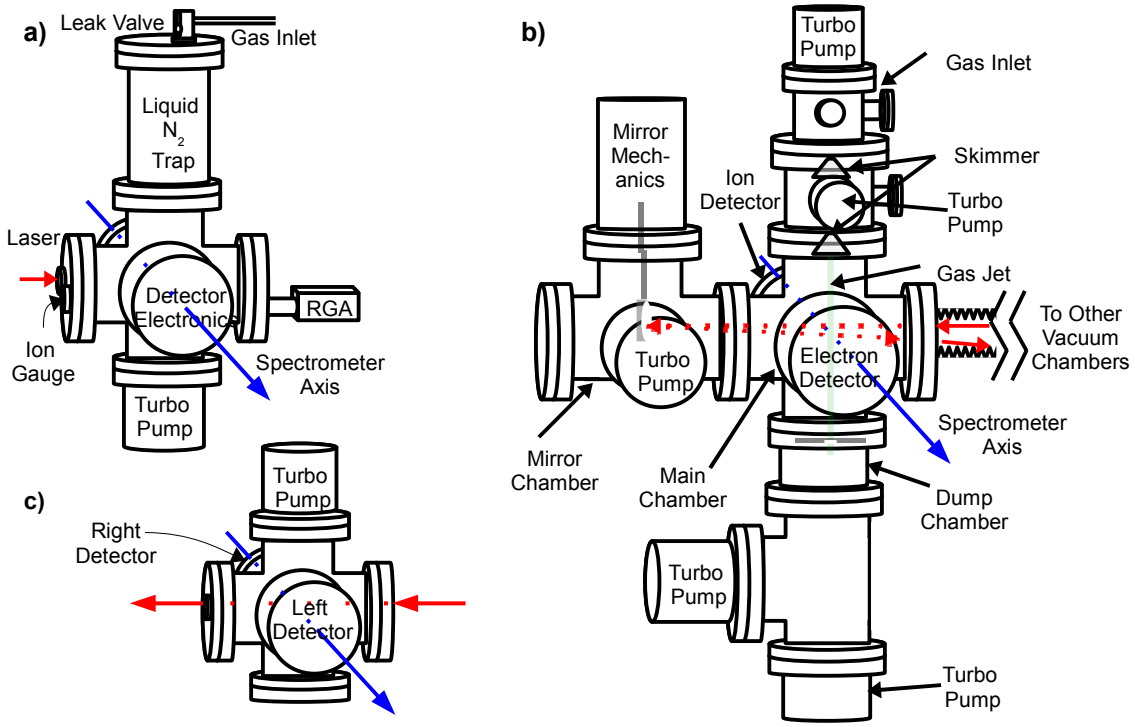

Figure 2.9: Diagram of the ultra high vacuum chambers. The main experimental chambers at a) UVA and b) MPQ. c) The stereo ATI chamber used at MPQ to measure the carrier envelope phase of each laser pulse.

house the interaction regions. Several components are required to establish the environment, including gas inlet lines, a liquid nitrogen cold trap, vacuum pumps, pressure gauges, and an interlock system. Figure 2.9 illustrates the basic chamber designs. The chambers are pumped out to a base pressure as low as 4×10^{-10} Torr, and then the target gas is introduced, either effusively (at UVA) or through a supersonic jet (at MPQ).

2.3.1 Vacuum Pumps

Roughing Pumps

There are several instances in which we require a rough vacuum, specifically to pump impurities out of the sample gas lines before filling the vacuum chamber and to bring the foreline section of the turbomolecular pumps to a rough vacuum. To meet these needs, we use several dual-stage rotary vane pumps from Varian Vacuum Technologies [58]. Typically, these pumps are able to create a vacuum down to 2×10^{-2} Torr. In order to reduce oil contamination, the rouging pumps on the AS-1 beamline are of the dry scroll variety, and similar pressures are obtained.

Turbomolecular Pumps

Rotary vane roughing pumps are only able to create a pressure as low as a few mTorr. In order to create a higher vacuum, at UVA we use a Turbo-V 1000HT turbo-molecular pump from Varian Vacuum Products [59]. Within the pump, a high frequency motor drives a turbine that is fitted with eight bladed stages located prior to four Macrotorr stages. High precision lubricated ceramic ball bearings support the turbine rotor. The pump itself is driven by an accompanying turbo pump controller [60], which is interlocked to the other vacuum components (see Section 2.3.3). The controller is equipped with a soft start procedure that slowly ramps up the turbine rotation rate, and it also monitors the amount of current being drawn by and the temperature of the pump. Under normal, full speed operation, the turbine rotation rate is 633 Hz. With proper backing, the turbo pump is able to reach a vacuum as low as 4×10^{-10} Torr. The foreline of the turbo pump also contains a dual pneumatic- and electrically-operated valve [61], which is included in the vacuum interlock circuitry. Five turbo pumps of varying sizes from a variety of manufacturers such

as Varian, Leybold, and Pfeiffer are used on the experimental chamber at MPQ. While the pumps' specifics may be different, they all operate on the same principle and work together to maintain chamber pressures on the order of 10^{-9} to 10^{-10} Torr.

2.3.2 Gauges

In order to monitor the vacuum in the various regions of the vacuum chamber system, we use several gauges. The pressures sensed by the thermocouple and nude ion gauges are read out by Varian's senTorr Gauge Controller [62]. This controller is added to the interlock circuitry, to which it provides set point relays to alert the system of excessive chamber or foreline pressures.

Thermocouple Gauges

For measuring the rough vacuum in the gas inlet lines and monitoring the pressure backing the turbo pumps, we use Varian Model 531 thermocouple gauges. Thermocouple gauges are based on the idea that gas will conduct heat away from a hot wire. For a fixed heater power, the temperature, which depends upon the conductivity of the gas, is monitored and converted to a voltage output by the thermocouple. Lower pressure will result in less heat being dissipated by the gas and, therefore, a higher temperature and higher voltage. This voltage is then converted into a pressure reading by the senTorr gauge controller. These thermocouples are able to measure pressures between 1×10^{-3} and 2 Torr.

Nude Ion Gauge

Pressures inside the high vacuum chamber fall far below the detection limit of thermocouple gauges, so nude ionization gauges are used instead. The 580 nude ionization gauge from Varian [63] is based upon the Bayard-Alpert gauge design, in which a hot filament (cath-

ode) produces electrons and accelerates them towards a positively charged cylindrical grid (anode). Within the volume of the grid, the electrons collide with gas molecules and ionize them. The resulting molecular cations are attracted to a wire at near-ground potential (but negatively charged with respect to the grid) running along the center axis of the grid, and the resulting current flow is directly proportional to the number of molecules present. This design allows pressure detection as low as 4×10^{-10} Torr.

Residual Gas Analyzer (RGA)

In some instances, it is desirable to know the composition of the gas within the vacuum chamber in addition to the total gas pressure. The molecular composition can be determined by a residual gas analyzer (RGA) [64]. Like the nude ion gauge, the Stanford Research Systems (SRS) RGA200 ionizes a small fraction of the residual molecules present inside the high vacuum chamber. It then uses a quadrupole mass spectrometer to temporally separate the ions according to their charge-to-mass ratios, allowing for identification of the molecules. If properly calibrated, the RGA can also provide concentrations or absolute partial pressures of the constituent molecules. The SRS RGA is completed with a Windows software package to initiate the measurements and perform analysis.

2.3.3 Interlocks

A central interlock box provides a series of voltage relays that control AC power to the turbo pump, nude ion gauge, pneumatic valve, and high voltage power supplies. In the event of a fault by any of the interlocked vacuum components, a power outage, an increase in chamber or foreline pressure above a desired set point, or compressed air failure, the pneumatic valve will close, sealing off the chamber, the turbo pump will spin down, and a rough vacuum will be maintained inside the chamber. Maintaining at least a rough vacuum

is essential for the storage of the microchannel plates (MCPs) inside the chamber.

2.3.4 Liquid Nitrogen Cold Trap

At times it is advantageous to perform experiments on gas samples below room temperature. By adjusting the leak valve on the UVA chamber, one can direct the gas molecules through a thin copper tube that is wrapped around a canister filled with liquid nitrogen. The thermal contact between the two metals will serve to cool the target gas molecules prior to their introduction into the interaction region. Filling the trap with liquid N_2 also serves to freeze out some of the water that may be contaminating the chamber.

2.3.5 Supersonic Jet in MPQ Chamber

The chamber at MPQ houses a true COld Target Recoil Ion Momentum Spectrometry (COLTRIMS) setup [65], one of the key components to which is a cold target gas. This is achieved through supersonic expansion of the target gas through a small, adjustable orifice [66]. As long as the orifice diameter is much larger than the mean free path of the gas in the reservoir, the gas molecules undergo many collisions with one another as they exit through the orifice, causing cooling during the expansion process. When expanded from a reservoir into vacuum, the final temperature of the gas is related to the initial pressure, p_0, and temperature, T_0, by

$$\frac{T_f}{T_0} = \left(\frac{p_f}{p_0}\right)^{(\gamma-1)/\gamma} \tag{2.2}$$

where γ is the heat capacity ratio, C_p/C_V, of the gas. As illustrated in Figure 2.9, the target gas is introduced into the top portion of the chamber to a pressure of 0.5-1$\times 10^{-3}$ mbar. Typical pressures in the first expansion chamber are on the order of 5 $\times 10^{-9}$ mbar,

which, according to Equation 2.2, leads to final gas temperatures below 10 K for the atoms and small diatomic molecules used in this work. Adjusting the backing pressure and size of the slit affords some control over the degree of cooling. The orifice is followed by two cone-shaped skimmers to allow only the central, coldest portion of the molecular beam to enter the interaction chamber.

2.4 Detection Hardware

Detecting the laser-matter interaction events created inside the high vacuum chambers requires an array of hardware. Ions or electrons created in the event are guided toward a charged particle detector by an electromagnetic field. The detector then sends electrical signals though a variety of electronics for amplification, noise discrimination and filtering before they are finally recorded with a PC or displayed on an oscilloscope.

2.4.1 Time-of-Flight Mass Spectrometer

The ions that are created during the laser-matter interaction event are extracted from the interaction region and accelerated towards the ion detector by an applied electric field. In such a situation, the acceleration of a charged particle due to the applied electric field is proportional to the particle's charge-to-mass ratio. Specifically, along the spectrometer axis, which we will call $\hat{z}$,

$$F_z = ma_z = qE_z = \frac{qV}{l} \tag{2.3}$$

where F_z is the force felt by the charged particle, m and q are the particle's mass and charge, respectively, V is the applied voltage, and l is the distance over which the voltage is applied. From this, it is obvious that

$$a_z = \frac{qV}{ml} \tag{2.4}$$

Recall that, for a particle with zero initial momentum, the equation of motion is

$$z = \frac{1}{2} a_z t^2 \tag{2.5}$$

where z is the distance traveled by the ion in electric field. Substituting Equation 2.4 in for a_z and solving for the time-of-flight, we find

$$t = \sqrt{\frac{2z}{a_z}} = \sqrt{\frac{2mlz}{qV}} \propto \sqrt{\frac{m}{q}}. \tag{2.6}$$

While the details are slightly more complex for a spectrometer that includes a field-free drift region, such as the UVA spectrometer, it remains that a particle's time-of-flight depends upon its mass-to-charge ratio and the applied field. By appropriately selecting the applied voltage, one can separate different ionic species for study. The resolutions for the UVA and MPQ spectrometers are even sufficient to identify specific dissociation channels within the same fragment ion species.

The spectrometer at the University of Virginia is built in a single-stage Wiley-McLaren design [67], with a 10.6 cm extraction region followed by a 21.7 cm field-free drift region. A series of spectrometer plates connected by voltage dividers maintain a homogeneous electric field along the spectrometer axis. Typically, voltages between 250 V and 1.5 kV are applied across the extraction region; voltages below 250 V are not recommended, as the field may not be strong enough to contain ions with initial momentum imparted by the molecular dissociation event directed away from the detector.

At MPQ, we have available a two-sided spectrometer, which allows for the simultaneous

collection of both ions and electrons. It consists of only an extraction region with a total length of 32.64 cm. Should electron detection be necessary, a magnetic field is applied - in addition to the electric field for ion extraction - by a pair of Helmholtz coils to confine the electrons and guide them towards the electron detector. Depending upon the species of interest, applied electric fields range widely from $\sim$ 1 to 40 V / cm.

Note that both spectrometers are designed with wide-aperture spectrometer plates. This facilitates the collection of ions emitted into the full 4π solid angle, allowing for full 3D fragment momentum to be calculated.

2.4.2 Microchannel Plates

The ions and electrons created in the atomic ionizations and molecular dissociations under study here are created with so little kinetic energy that they would never be able to produce a signal from any detector by themselves. Rather, we must use some sort of electron multiplier to facilitate their detection. Microchannel plates are composed of millions of tiny glass capillaries, fused together in a hexagonal close packed array, and then sliced into thin plates [68], illustrated in Figure 2.11. The substrate is reduced in a hydrogen-rich environment, making it conductive, so each hole, or channel, acts as an electron multiplier. By applying a voltage across the MCP, primary electrons produced by charged particles or photons incident in a channel are accelerated down the channel, where further interactions with the walls of the channel create secondary electrons. At the channel's end, these electrons emerge as a temporally- and spatially- localized distribution. Stacking two or three MCPs in a chevron or "Z" pattern improves gain and helps to eliminate ion feedback at the expense of some resolution [68]. Both the University of Virginia and the AS-1 MCPs are of the Z-stack configuration, although plate diameter, channel size, and resolution vary.

Cautionary note: too much ion current can damage and lead to dead spots on the MCPs.

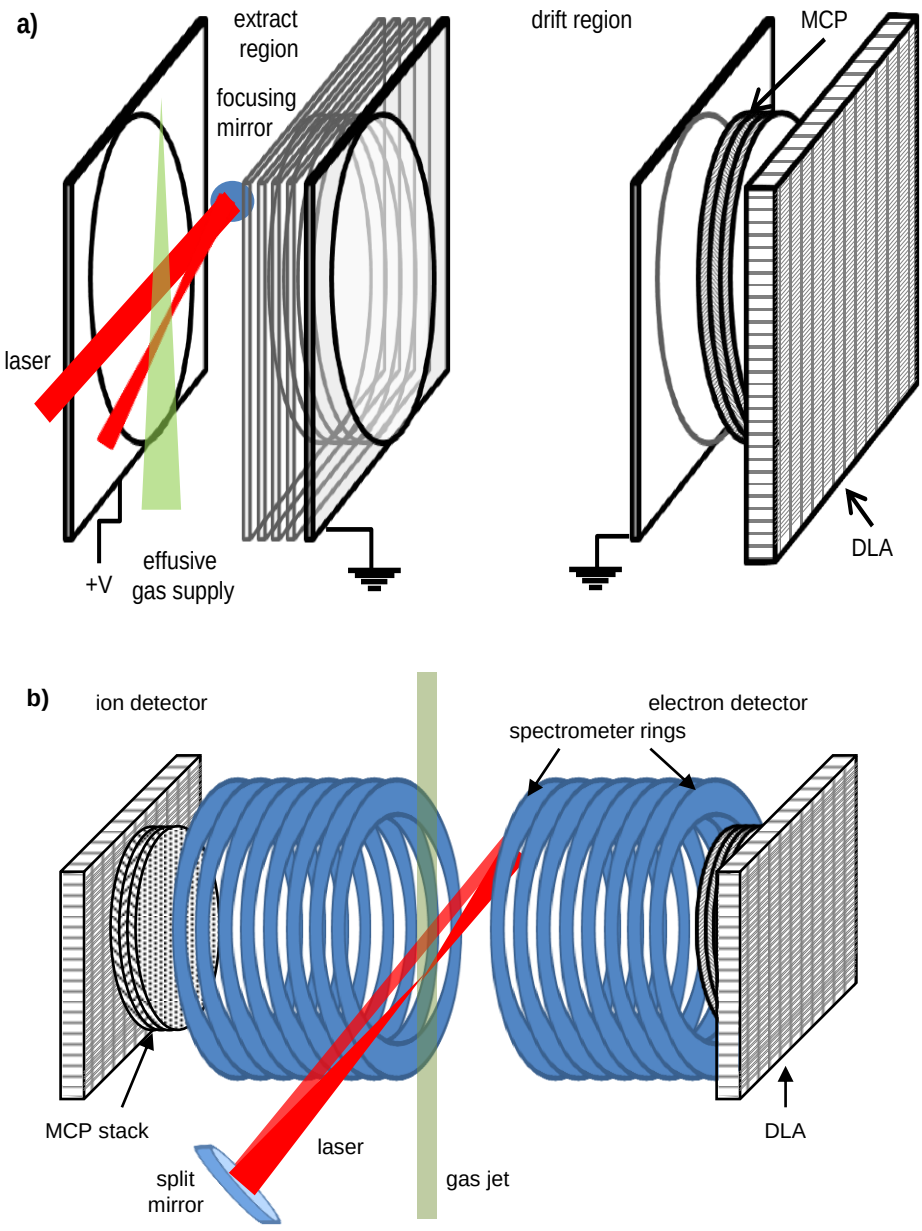

Figure 2.10: Diagram of the a) chemistry and b) MPQ time-of-flight spectrometers. The chemistry chamber's spectrometer is single-sided, but it incorporates a field-free drift region, whereas the MPQ spectrometer is symmetric about the interaction region, allowing for detection of both ions and electrons simultaneously.

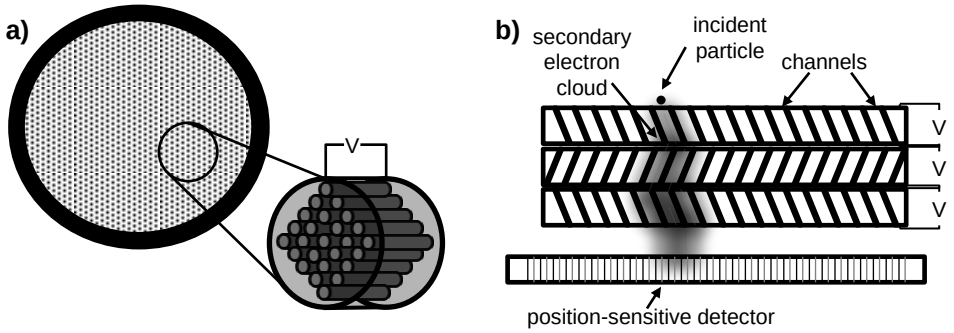

Figure 2.11: a) Front and perspective view of a single microchannel plate. b) Side view of three MCPs in a Z-stack configuration. Slightly offsetting the bottom two plates allows electrons from the first plate to fill multiple channels, increasing the gain.

When working with highly-charged fragments, an abundance of lower-charged fragments and molecular ions are also created. The molecular ions are particularly damaging, as they tend to have low transverse momentum, causing them to exclusively hit one location on the detector. Therefore, in order to eliminate unnecessary current from these lower charged ions, a high voltage switch is placed between the high voltage power supply and the MCPs, and it is used to switch off the voltage before their arrival, preventing loss of MCP emission efficiency.

2.4.3 Time-of-Flight Detection Electronics

After sending the MCP signal through a Stanford Research Systems (SRS) Model SR240 fast preamplifier [69] and into an oscilloscope, one sees the time-of-flight spectrum of the ions present inside the chamber. Viewing this is a fast and easy way to optimize experimental parameters such as laser intensity and chirp, gas pressure, and spectrometer voltage. If position and momentum information of the particles is not required, meaningful time-of-flight data can be collected by sending the amplified MCP signal through an SRS SR250 fast gated integrator and boxcar averager [69], followed by an SRS SR245 Computer Interface

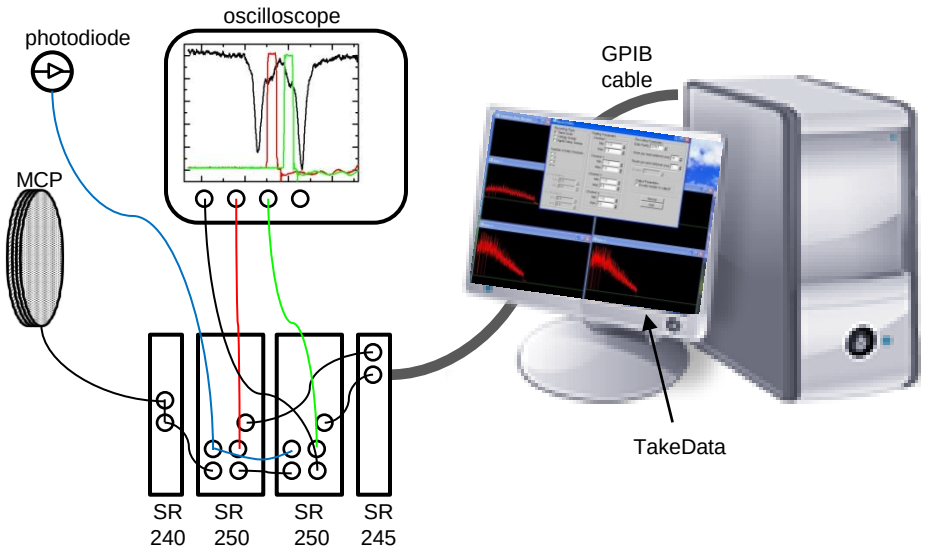

Figure 2.12: Diagram of the current mode detection scheme. The signal from the back MCP plate inside the vacuum chamber is amplified and then sent through a chain of boxcar integrators. A photodiode sensing the laser pulse itself provides the master trigger. Both the time of flight signal (black wire) and each of the boxcar's gates (red and green wires) can be viewed on an oscilloscope, and the resulting gated, averaged signals are sent from the SR245 computer interface unit to the computer via GPIB cable.

module [69], and finally collecting it through the TakeData program, which outlined in Section 2.5.1. With the boxcar averager, one can set a window, or gate, of interest around the desired time-of-flight peak. The boxcar averager then integrates the area under the gated curve for every laser shot, averages a specified number of laser shots, and outputs this integrated signal to the SR245. One can daisy chain boxcar units for simultaneous data collection of up to four ion species or time-of-flight peaks. We refer to this data collection method as "current mode," as it is based upon a signal containing many ions in each time-of-flight peak, creating a continuous ion current within each laser shot; it is illustrated in Figure 2.12.

2.4.4 Stereo-ATI Electron Detection

Microchannel plates are used as the sole means of detecting electrons ejected from xenon atoms in the stereo-ATI phase meter at the Max Plank Institute [70]. Details of this technique are discussed at length in Chapter 4. Briefly, electrons from the ionization events are ejected towards opposite sides of the vacuum chamber, which is lined with μ-metal shielding to cancel outside fields and ensure electron containment and collection (see Figure 2.9 c)). The ion currents from the left and right detectors, which are located symmetrically about the ionization region, are input into a specially designed electronic circuit that places two time of flight gates on each of the left and right signals, integrates these signals, and then calculates the asymmetry parameter, β,

$$\beta_1 = \frac{L_1 - R_1}{L_1 + R_1} \tag{2.7}$$

for each time of flight region, designated here by the subscript. Combining the asymmetry parameters for regions 1 and 2 allows determination of the carrier envelope phase for each laser pulse. This information is collected through an amplitude-to-digital converter (ADC) card (see Section 2.4.7) for each event in the data acquisition.

2.4.5 Delay Line Anode

We employ a delay line anode (DLA) as a detector to interpret the two-dimensional position information available from the MCPs' localized electron shower. The DLA is mounted directly behind the MCP stack and consists of two pairs of wires tightly wound, one pair in the $\hat{x}$ direction and one in the $\hat{y}$ direction, around a 10 cm square ceramic form. Within each wire pair, one wire is the signal wire and the other is the reference. Using a voltage supply followed by a voltage divider, 400 V is placed on the signal wire and 350 V on the reference

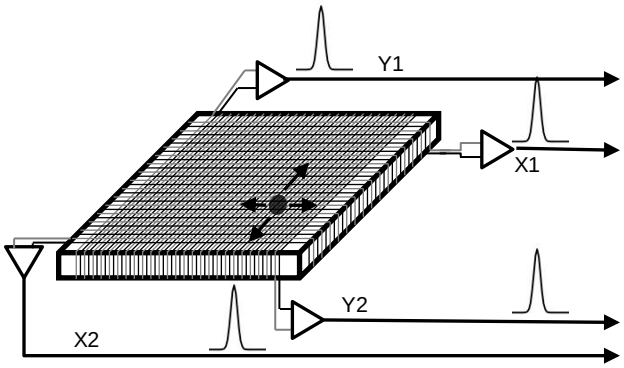

Figure 2.13: Diagram of delay line detector. Pairs of signal (black) and reference (gray) wires are wrapped orthogonally around a 10 cm × 10 cm ceramic plate. A localized electron shower from the MCPs creates a signal which propagates to both ends of each wire, and a differential amplifier amplifies each of the four signals.

wire; the more-highly charged signal wire will preferentially collect the electron shower from MCPs, and the two signals will amplified in the subsequent differential amplifiers. When it hits the wires, an electron shower will create a current that will travel in both directions along the vertical and horizontal wire pairs. The sum of the arrival times of the signal at each end of a wire is constant $t_{Xtot} = t_{X1} + t_{X2}$, and subtraction of the arrival times locates the spatial position of the initial ion hit in that dimension, $\Delta t_X = t_{X1} - t_{X2}$. Although the delay line anode has the capability of detecting multiple hits per laser shot, in order to achieve clean, high-quality data, it is important to keep the count rates to only a few hits per laser shot to prevent convolution of the X1, X2, Y1, and Y2 information of multiple hits. This data collection technique is referred to as "count mode."

2.4.6 Position- and Time-Sensitive Fast Electronics

After they have been differentially amplified, the X1, X2, Y1, and Y2 delay line signals are sent into separate channels of an Ortec Model 935 Quad Constant Fraction Discriminator (CFD) [71]. This unit produces standard NIM output pulses for input pulses of varying amplitudes and widths. By selecting a timing point on each pulse that is independent of pulse amplitude, the timing of the output pulse is locked to that of the input pulse. Adjusting the threshold knob rejects low-level noise, so this unit also acts as a filter for valid hits. The master trigger for count mode data collection is derived from the laser pulse itself, as seen by a photodiode. The signal from this photodiode is also sent first through a CFD to prepare a standard signal for the subsequent electronics.

Next, a Phillips Scientific (PS) Model 794 Quad Gate/Delay Generator [72] is used to create a time window around the ion time-of-flight peaks of interest in much the same way as when using the boxcar averager in the current mode scheme. This gate signal and the X1, X2, Y1, and Y2 signals from the CFD channels are logically combined in the four channels of a PS Model 752 Quad Two-Fold Logic Unit [73], which outputs a NIM pulse if and only if a delay line signal arrives within the specified time window. A second PS 794 is used to create a start signal for the TDC card from the discriminated photodiode trigger.

TDC Cards

Time-to-digital converter (TDC) cards provide the interface between the electronics modules and the data collection software. They function by subtracting the time between a signal and reference pulse and converting that to a number value. The UVA TDC card has eight LEMO ports for delay line and timing signals (channels 1-4 are used for the delay line signals and 5 for a time reference) plus one port which provides a common start or stop point for all

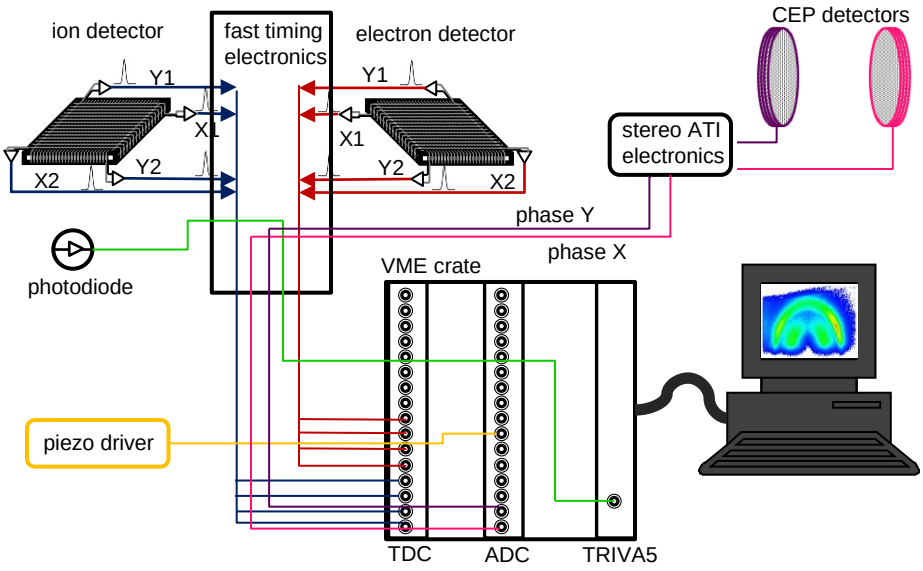

Figure 2.14: Diagram of the MPQ count mode detection scheme. Signals from the ion and electron detector, the stereo ATI phase meter, and the master trigger from a photodiode are sent through a bank of fast timing electronics, including CFDs and coincidence gates. Then, they, along with a reference signal from the split mirror's piezo driver, are read into the computer by the TDC and ADC cards in the VME crate. The Go4 software is used to monitor the data acquisition.

channels. It occupies one of the ISA slots in the data-collecting computer, and it is capable of detecting up to 16 hits per channel per laser shot with a double pulse resolution of 10 ns. The CoboldPC computer program from RoentDek [74] facilitates communication with the TDC card, and is described in Section 2.5.2.

2.4.7 AS-1 Data Collection Hardware

Data collection at the AS-1 beamline at MPQ utilizes some similar and some slightly different equipment than at UVA. A basic block diagram of the data collection scheme can be found in Figure 2.14. Trigger signals for the hardware are all derived from the laser pulses via a photodiode and a series of CFDs, delay generators, and logic boxes. Similar electron-

ics modules to those at UVA are used to discriminate against noise, coincidence gate, and create meaningful signals for the TDC from the photodiode, MPC, and DLA signals. At this point, however, the hardware and software specifics of the two data acquisition setups diverge.

Whereas at UVA we simply access the TDC card via the ISA slot on the desktop computer, the data collection at the AS-1 beamline utilizes a VME- based data acquisition hardware. (VME is simply a different form factor and bus protocol for hardware access.) There is a VME crate which houses and supplies power to a trigger and synchronizing module (TRIVA5), a TDC card and an analog-to-digital converter (ADC) card. The TDC card is a CAEN V1290N, which has 16 channels and a resolution of 25 ps [75]; it is used to read in the delay line and MCP signals from the ions and electrons detected in the main experimental chamber. The ADC card, a CAEN V785N [76], detects and converts the peak value of a pulse to a digital value. This is used to collect the laser pulses' CEP information from the stereo-ATI chamber as well as the signal being fed into the piezo driver to drive the split mirror inside the chamber.

The TRIVA5 trigger module [77] accepts external triggers and also controls the GO line, and, therefore, the starting and stopping of data taking for the whole system. Communication with the TRIVA5/VME hardware occurs through the Multi-Branch System (MBS) software [78], a C-based program accessed through a LINUX bash shell on the desktop computer, which is connected to the VME crate via ethernet cable. This software allows the user to activate channels on the TDC and ADC cards, start and stop data acquisition, and control the writing of the incoming events to hard disk on the desktop computer.

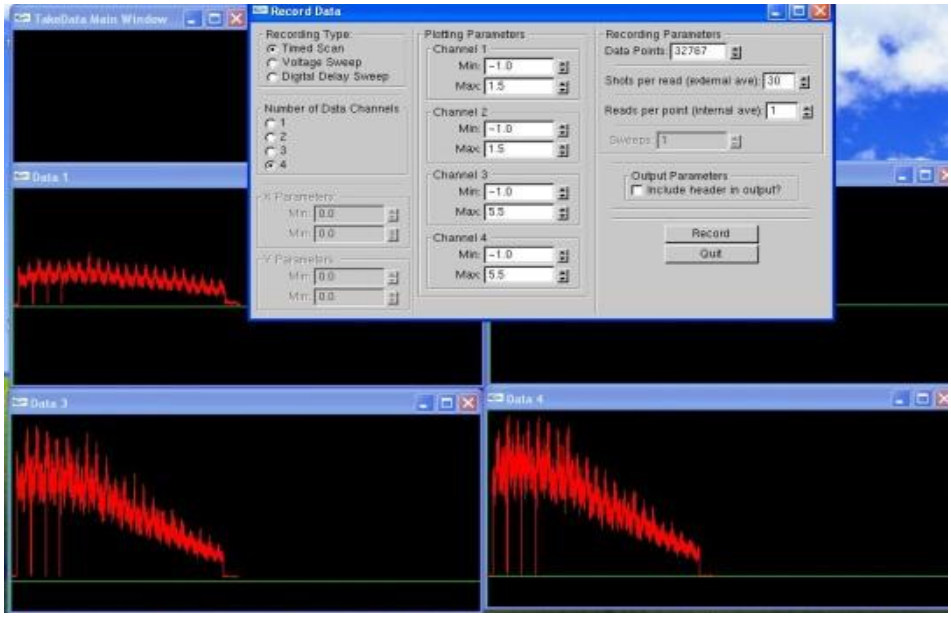

Figure 2.15: TakeData is the software used to record and visualize data taken in current mode. The "Record Data" window allows the user to specify experimental parameters. Subsequently, a window corresponding to each active channel will be activated and display the incoming signal.

2.5 Detection Software

2.5.1 TakeData

A non-commercial, C++ based program written by Charles Conover called TakeData [79] is used to record the current mode data obtained at UVA. This program communicates with the RS245 unit via GPIB cable, and allows for simultaneous recording of data from up to four channels. It can also be used to control external apparatus such as inchworm motors and DG535 units and for subsequent re-reading of the data, although this feature is seldom utilized. Within the "Record Data" window, see Figure 2.15, one can specify experimental parameters, such as recording type, number of channels, scan time and signal averaging.

After data collection, the data may be saved in .itx file format, readable by any common data analysis software.

2.5.2 CoboldPC

At UVA, CoboldPC, a commercial software program from RoentDek [74] is used to communicate with the TDC card, control data acquisition and file writing, and analyze the data. CoboldPC, which stands for Computer Based Online Offline Listmode Dataanalyzer, is a C++ based program which consists of a DAQ.dll dynamic link library to interface the main program with the hardware and a DAN.dll link library for data analysis. Data collected in count mode is collected on an event-by-event basis and is stored in list mode file format. All of the pieces of information, such as the X1, X2, Y1, Y2, and time of flight signals for each ion hit, that make up the first event are stored in layer one of the file, the second event is stored in layer two, and so on. Saving the raw data in this manner allows the user to rerun the experiment multiple times with different analyses. Decoding and analysis of these list mode files is done by user modifications to the C++ files contained in the DAN.dll library. Here, one can customize parameters such as fragment mass and charge, spectrometer voltage, etc. and write appropriate code for data filtering, momentum calculation, and any further analysis. A second file, called the command file, provides a convenient method for data visualization. It is a list of commands called by the main program that define the histograms and spectra to be viewed, as well as conditions which the data must fulfill in order to be included in the histograms. Alternatively, these commands can be entered into the prompt window within the main program. From within the main window, one can also export histograms as pictures or ASCII files for further manipulation.

2.5.3 Go4

The count mode data from MPQ is collected and written to file by the MBS software, but this program does not support visualization or analysis of the data. Online data monitoring and offline data analysis is preformed through the Go4 (GSI Object Oriented On-line-Offline) analysis framework [80], developed at the GSI Hemlholtz Centre for Heavy Ion Research. Go4 consists of an analysis framework based on the ROOT system used at CERN [81] and a Qt based graphical user interface. Within Go4, analysis of the list mode files is divided into three steps: Unpack, where simple manipulation puts the raw data in terms of time of flight and position; Calc, where 3D momentum vectors are calculated and hits are filtered and checked for coincidence; and Finish, where the user can do advanced data manipulation and plot construction. By modifying the C++ files for each of these steps, the user can tailor the analysis to specific requirements.

Table 2.1: Laboratory Equipment Inventory

	Chemistry Rm. 204 UVA	AS-1 Beamline MPQ
Laser Amplifier	Multipass Ti:Sapphire 1 kHz	Multipass Ti:Sapphire 3 kHz
Pulse Characteristics	40 fs @ 1.2 mJ per pulse	<5 fs @ 0.4 mJ per pulse
Pulse Diagnostics	Grating Spectrometer SHG FROG	USB Grating Spectrometer Single-Shot Autocorrelator Stereo-ATI Phasemeter
Vacuum Hardware	Turbopumps, Ion Gauge RGA	Turbopumps, Ion Gauges
Cooling	Liq. N_2 Cold Trap	Supersonic Jet
Gases Used	N_2, O_2, CO, CO_2	N_2, O_2, CO, NO, Ar, Ne
Spectrometer	Single-stage TOF	Two-sided TOF
Detectors	'Z Stack' MCP with Helical Delay-Line Anode	'Z Stack' MCP with Helical Delay-Line Anode
Data Collection Methods	Current Mode Count Mode	Count Mode
Software	TakeData CoboldPC	Go4
Experiments	Two Color Field Asymmetry	Phase Tagging Few-Cycle Pulse NSDI Molecular Few-Cycle Pulse Asymmetry

Chapter 3

Directional Coulomb Explosion of Molecules in Two-Color Laser Fields

3.1 Introduction

Intense asymmetric laser pulses, those with a distinct, controllable difference in the electric field in one direction versus the other, are powerful tools for controlling atomic and molecular processes. Theoretical and experimental investigations have applied directional fields to induce and control asymmetries in dynamics relevant to atomic excitation and ionization [82], above threshold ionization [4, 10, 11], high harmonic generation [12, 13, 83], molecular orientation [21, 22], and the dissociation of singly charged fragments from small [6, 14–19, 84] and large molecules [20]. Here we consider the control of combined electronic and nuclear dynamics in molecules at higher intensities where multiply-charged ion fragments are produced.

As discussed in Section 1.4, there are two standard approaches for creating asymmetric laser fields. Experiments involving the first method, which exploits the controllable difference in the directional field amplitude of few-cycle pulses, will be discussed in subsequent chapters. The experiments described in this chapter were performed using the two-color field approach, which involves the phase-coherent addition of a fundamental field at frequency ω with its second harmonic at 2ω [10]. Recall that, when linearly polarized, the two-color field has the form

$$E(t) = E_{\omega}(t)cos(\omega t) + E_{2\omega}(t)cos(2\omega t + \phi), \tag{3.1}$$

where $E_{\omega}(t)$ and $E_{2\omega}(t)$ are the fundamental and second harmonic field envelopes and ϕ is the relative phase between the two carrier waves. By changing ϕ, one alters the relative field strengths in the positive ("forward") and negative ("backward") directions (see, for example, the insets in Figures 3.2 and 3.3). A distinct advantage of the two-color approach is that, with only modest effort, the forward/backward field asymmetry can be made significantly larger than that attainable with current few-cycle fields [9].

Beyond demonstrations of quantum control, the contrast and absolute phase-dependence of directional yields can provide key insights into coupled electron-nuclear dynamics in strong laser fields. For example, pioneering experiments on dissociative ionization of HD^+ [14] showed that positively charged fragments were preferentially emitted "downfield," i.e. opposite to the direction of the maximum in the two-color field, as illustrated in Figure 3.1 (see also the discussion in Section 1.3). Soon afterward, measurements on H_2 [15] indicated that protons and electrons from dissociative ionization were preferentially ejected in the same direction in a two-color field. Both of these results were characterized as "counter-intuitive," i.e. at odds with expectations based on a "naive" classical model. Subsequent

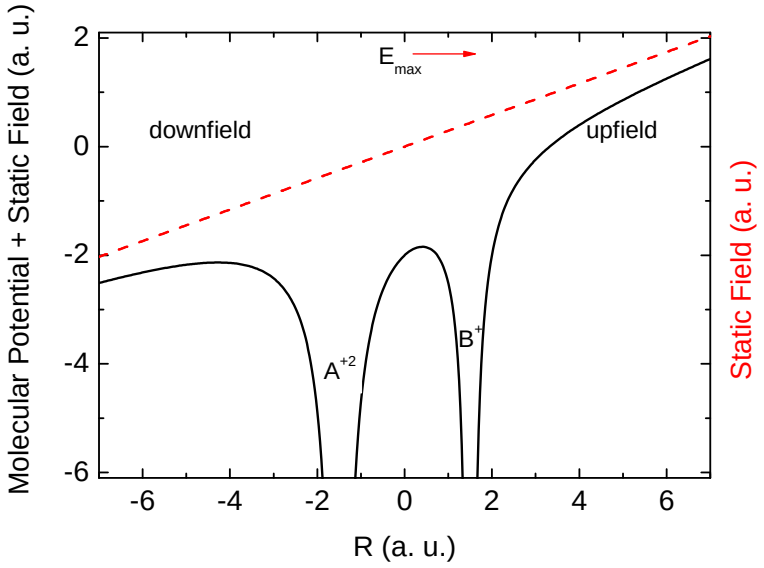

Figure 3.1: Picture of an electron inside an asymmetric molecule placed in a static field, which is a representation of the instantaneous asymmetric laser field. A change in ϕ by π will change the direction of the two-color field maximum by 180°, equivalent to reversing the direction of the static field in this representation.

theoretical work [23, 24] provided plausible resolutions to the controversy, predicting preferential ejection of electrons in the "counterintuitive" upfield direction, provided the post-ionization interaction between a departing electron and its parent ion are properly taken into account. Further, the preferred direction of proton emission from molecular hydrogen can be upfield or downfield, depending on the vibrational state distribution of the molecular ion, as this affects the principal ionization mechanism.

More recently, two-color experiments on dissociative ionization of D_2 [16] have shown that the optimal phase, ϕ_{max}, at which the D^+ yield exhibits the greatest forward/backward asymmetry, does not generally coincide with the phases $\phi = 0, \pi$ at which the field has the greatest asymmetry. Instead, ϕ_{max} depends on the energy of the dissociation products and the laser intensity [85], demonstrating the importance of the specific dissociation mechanism,

bond-softening, enhanced ionization, or electron recollision. They conclude that classical intuition based on directionality of the field is not effective for predicting the direction of ion fragment emission.

In this chapter, we discuss experiments exploring directional multi-electron dissociative ionization (MEDI) of N_2, O_2, CO, and CO_2 in a two-color field. Previous measurements on HBr [86] will also be referenced. In contrast to previous two-color dissociative ionization experiments [14–16, 19, 20, 87], we focus on multielectron ionization into non-symmetric dissociation channels $AB^{+Q} \rightarrow A^{+q} + B^{+(Q-q)}$ for which $2 \leq Q \leq 4$ and $q \geq 2$. We find that all such channels exhibit large, ϕ-dependent asymmetries in the fragment emission directions. Despite the substantial differences in molecular structure among these species, in all cases, the largest forward/backward ion asymmetries are observed at the same optimal phases, $\phi_{max} = 0, \pi$, for which the field asymmetry is also maximum. Unlike in molecular hydrogen, these optimal phases are insensitive to the net field strength and the relative intensity of the 800 nm and 400 nm field components for total intensities on the order of 10^{14} W/cm^2. If we adopt an independent phase calibration [21], then for all cases we have observed, the most positively charged ions are preferentially emitted downfield. While we avoid the use of "intuitive" or "non-intuitive" to describe the sign of this asymmetry, the uniformity of our results for different molecules and dissociation channels suggests that, in contrast to molecular hydrogen, a common mechanism associated with the difference in the peak field in the forward and backward directions is responsible.

3.2 Experimental Setup

This experiment was performed with the resources in the Chemistry lab at the University of Virginia. The experimental setup is sketched in Figure 3.2. Molecules are introduced

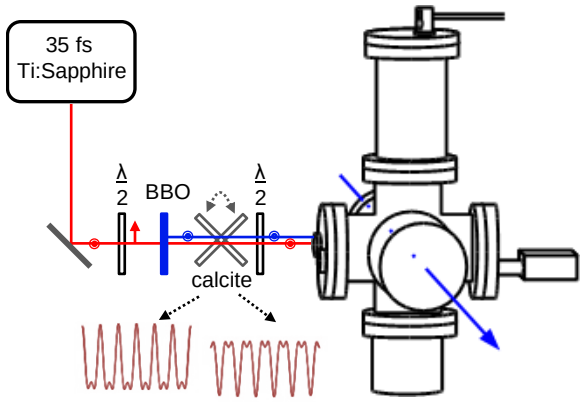

Figure 3.2: Beam path for the two-color experiment. $\lambda/2$: half-wave plate for 800 nm; BBO: β-barium borate crystal. Rotating the calcite plate adjusts temporal overlap of the two pulses and changes the two-color electric field, as shown in purple.

into the high vacuum chamber effusively through a continuous leak valve. An $f = 250$ mm spherical mirror located on the back wall of the vacuum chamber focuses the two-color beam into the molecular gas target at the center of the time of flight (TOF) spectrometer. A small electric field pushes positively charged ions formed by the laser toward the microchannel plate (MCP) detector. At low ion count rates, the full angular distributions of the ion fragments are measured using the delay line anode and the COBOLD data collection software. If full angular distributions are not necessary, we can quickly record only the ion yield vs. TOF, with ions emitted toward and away from the detector distinguished by their different flight times, via the current mode detection scheme. An example TOF spectrum of the N^{+2} ions from N_2 is illustrated in Figure 3.3. Unless otherwise noted, the polarization of the two-color field is parallel to the axis of the time of flight spectrometer.

To create the two-color field, linearly polarized, 35 fs, 800 nm laser pulses from the Ti:Sapphire laser are frequency doubled using type I phase-matching in a 250 μm thick BBO (β-barium borate) crystal. In order to compensate for dispersion induced by the

vacuum chamber window and other optics and the walk-off between the fundamental and second harmonic inside the BBO crystal, a 1.3 mm thick birefringent calcite plate is inserted into the two-color beam path with fast and slow crystal axes aligned along the 400 nm and 800 nm beam polarizations. Coarse and fine angle tuning of the calcite enables control over the relative pulse delay and relative optical phase, ϕ, respectively. An 800 nm 0-order $\lambda/2$ waveplate is then used to rotate the polarizations of the co-propagating beams to a common, horizontal axis. Previous two-color experiments [86] have used an interferometric setup, with the red and blue pulses created in the two separate arms of the interferometer. This technique allows independent control over the polarizations of the two beams, but, in general, the calcite configuration provides better phase-stability and greater forward/backward asymmetry contrast. The relative intensity, $I_{2\omega}/I_{\omega}$, is controlled by tuning the BBO crystal slightly off of the optimal phase-matching angle, although this method introduces additional channel-dependent phase shifts, as discussed in Section 3.3. The total two-color field intensity is varied over the range 0.8-5 $\times 10^{14}$ W/cm^2 by tuning a $\lambda/2$ plate before the compressor gratings to decrease the output power while retaining the beam's focal characteristics.

3.3 Results

Figure 3.3 shows a typical TOF spectrum for N^{+2} fragments from N_2, with TOF distributions for two different values of ϕ plotted in the inset. Two clear dissociation channels, $N_2(2,0)$ and $N_2(2,1)$, can be seen. The label AB(p,q) refers to the dissociation path $AB^{(p+q)+} \rightarrow A^{+p}+B^{+q}$. The bimodal TOF distribution for each channel indicates that the doubly charged fragments are produced during the dissociation of molecules that are preferentially aligned along the laser polarization, with momenta directed toward ("forward")

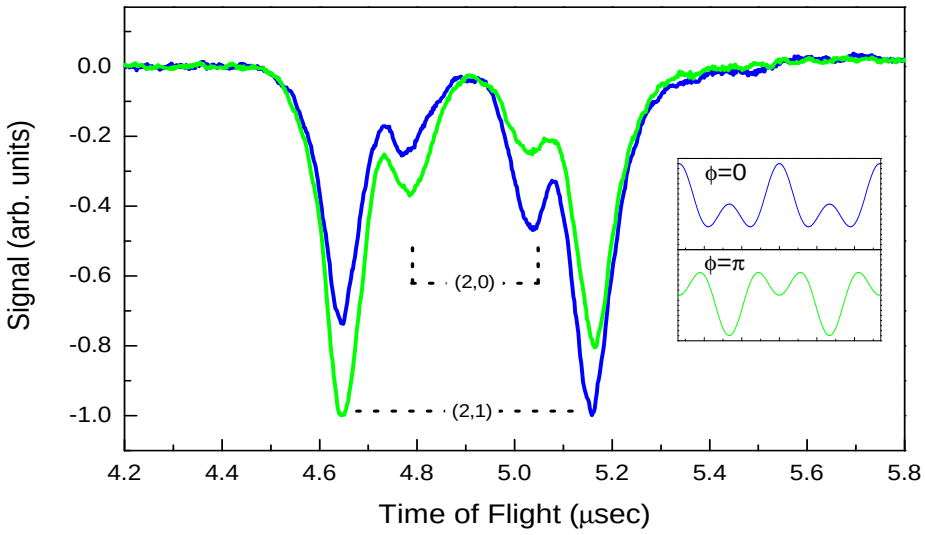

Figure 3.3: Time of flight spectrum for N^{+2} fragments from N_2 for two different two-color fields, $\phi = 0$ and $\phi = \pi$. Dashed lines denote fragment pairs from the N_2(2,0) and N_2(2,1) channels. Inset: Schematic of the two-color field with $E_\omega(t)$=$E_{2\omega}(t)$.

or away from ("backward") the detector. Both the N_2(2,0) and N_2(2,1) channels show a pronounced forward/backward signal asymmetry which reverses when ϕ is changed from 0 to π. For each dissociation channel, boxcar integrators are used to record the forward and backward yields, Y_f and Y_b, as ϕ is varied. As shown in Figures 3.4a and 3.4b, the raw yield data is used to compute a phase- and channel-dependent asymmetry parameter

$$\beta(\phi) = \frac{Y_f(\phi) - Y_b(\phi)}{Y_f(\phi) + Y_b(\phi)}. \tag{3.2}$$

Substantial asymmetries in the fragment ion directionality are observed for a wide variety of dissociation channels, including CO(0,2), CO(1,2), CO(2,2) [86], N_2(2,0), N_2(2,1), O_2(2,0), and O_2(2,1), and the C^+, C^{+2}, O^+ and O^{+2} fragments from CO_2. Figures 3.5 and 3.6 illustrate the raw data and associated asymmetry parameters for several O_2, CO, and

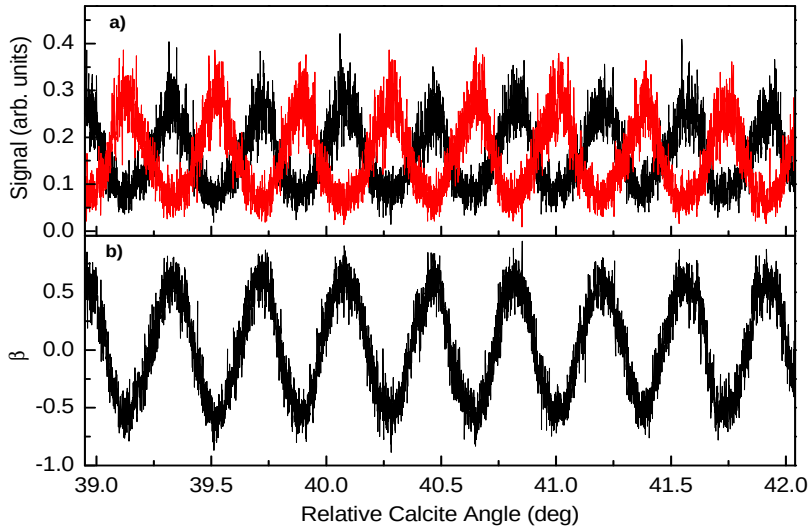

Figure 3.4: (a) Forward (black) and backward (red) N^{+2} fragment yields associated with the $N_2(2,0)$ dissociation channel for intensities I_ω=1.5×10^{14} W/cm^2 and $I_{2\omega}$=1.4×10^{13} W/cm^2 in the component beams. (b) Asymmetry parameter, β, computed from the data in (a).

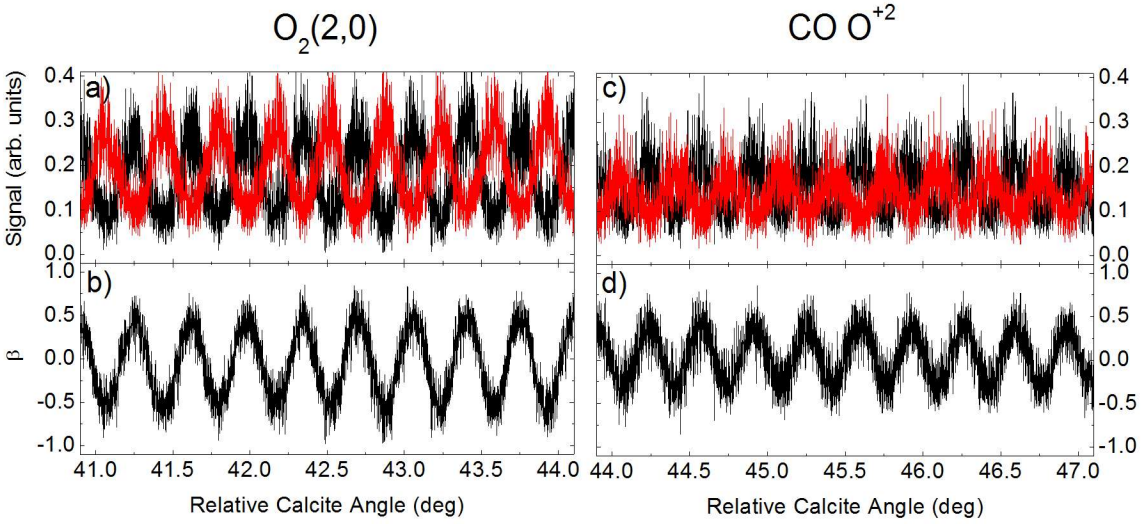

Figure 3.5: Raw data and asymmetry parameters, similar to Figure 3.4, for the O^{+2} fragments associated with the $O_2(2,0)$ channel (a,b) and the CO (1,2) and (2,2) channels (c,d; the two channels were not separated in this data).

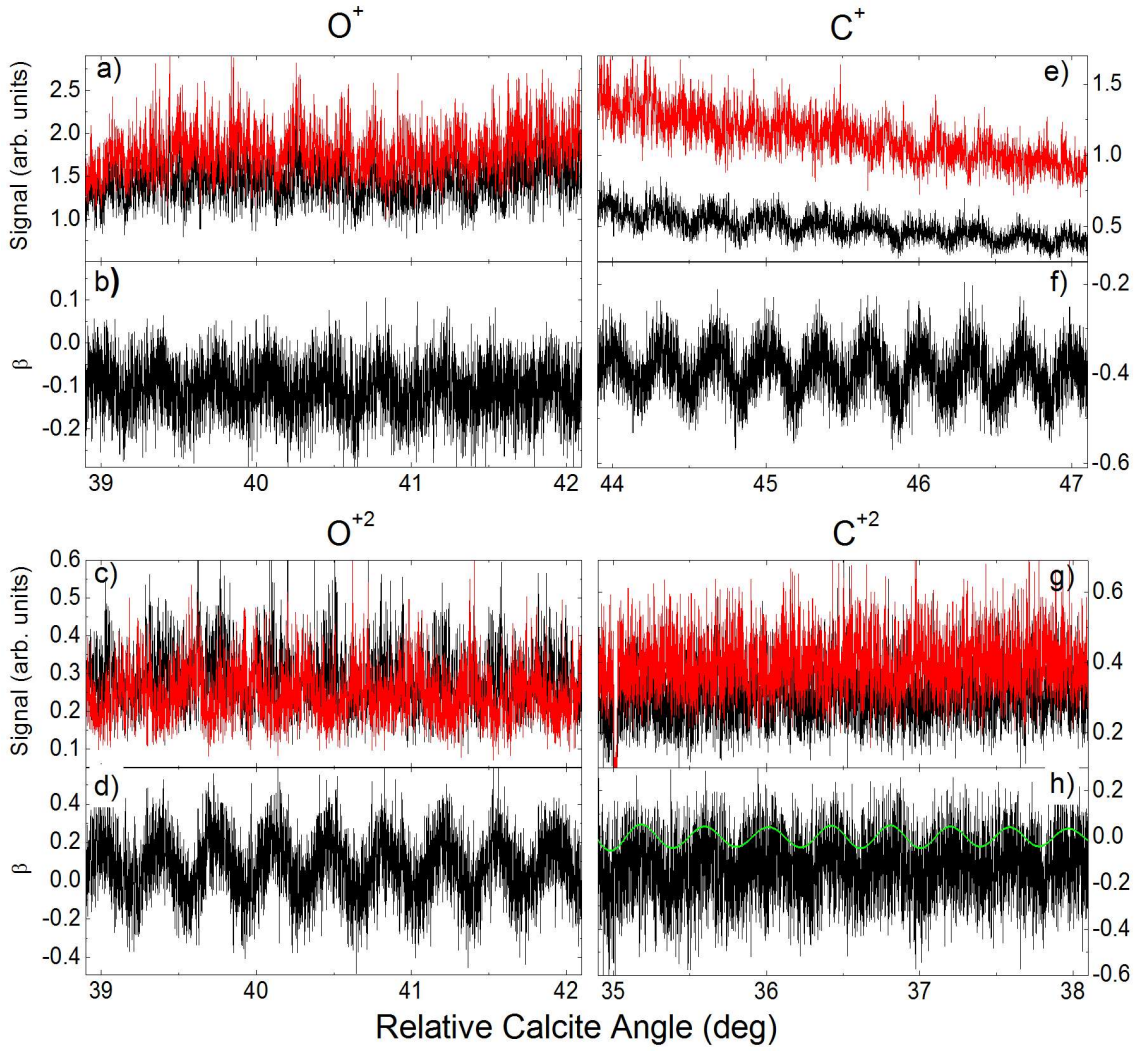

Figure 3.6: Raw data and asymmetry parameters, analogous to Figure 3.4, for the C^+, C^{+2}, O^+ and O^{+2} fragments from CO_2. The data in (h) has been Fourier filtered and plotted in green to guide the eye.

CO_2 fragments. Previous work also revealed similar results for the Br^{+3} ions from HBr [86]. In each case, the strength of the asymmetry depends on the relative intensity, $I_{2\omega}/I_{\omega}$, as well as the total intensity. Optimization of these parameters results in peak β values of ± 0.7 and ± 0.4 for the (2,0) and (2,1) channels, respectively, from N_2 and O_2. Comparable asymmetry levels are observed in the CO(1,2) and CO(2,2) channels (see Figure 3.5d), while those associated with the Br^{+3} ions from HBr and the C^+, C^{+2}, O^+, and O^{+2} fragments from CO_2 (see Figure 3.6) are factors of two to three smaller. While oscillations are not always cleanly visible in the raw data, they are present in the $\beta(\phi)$ curves.

Figure 3.7 shows the N_2^+ molecular ion yield and β for N_2(2,0) vs. ϕ. The molecular ion signal exhibits pronounced oscillations at twice the frequency observed in the forward/backward fragment yield. The periodicity is consistent with the changes in the N_2 tunneling ionization rate, due to the ϕ-dependence of the maximum field amplitude in each field-cycle. Since the ionization rate is independent of the sign of the field, tunneling ionization theory predicts the greatest molecular ion yield when the two-color field has its largest magnitude, i.e. for $\phi = 0$ and π (modulo 2π). As shown in Figure 3.7, within an experimental uncertainty of ± 5 degrees, the maxima in $|\beta|$ for N_2(2,0) occur at the same phases $\phi_{max} = 0, \pi$ as the peaks in the N_2^+ yield.

By consecutively measuring $\beta(\phi)$ for different species and channels and referencing all measurements back to N_2(2,0), we find that *for all observed dissociation channels involving multiply charged ions*, $|\beta|$ has maximum values at $\phi_{max} = 0, \pi$. This is demonstrated for the (2,0) and (2,1) channels for N_2 and O_2 in Figure 3.8. Note that in order to obtain consistent results, it is crucial that the central frequency of the 2ω beam be precisely twice that of the ω beam. If this is not the case, i.e. the BBO crystal is tuned off of the optimal phase-matching angle, an angle-dependent phase shift between maxima for different dissociation channels is

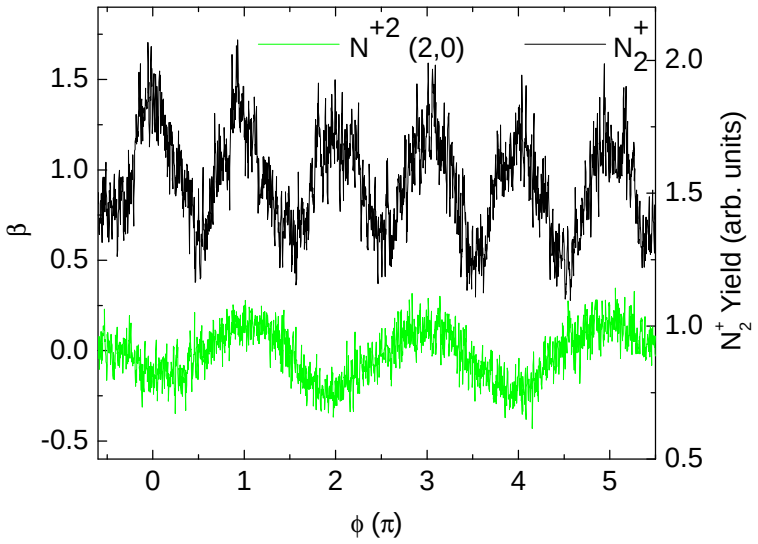

Figure 3.7: Comparison of the total N_2^+ tunneling ionization yield to the $N_2(2,0)$ asymmetry. The frequency of the molecular ion yield modulation is twice that of the fragment asymmetry, as the N_2^+ yield is dependent upon only the field magnitude, not the sign. Within experimental uncertainty, the two signals are in phase with one another.

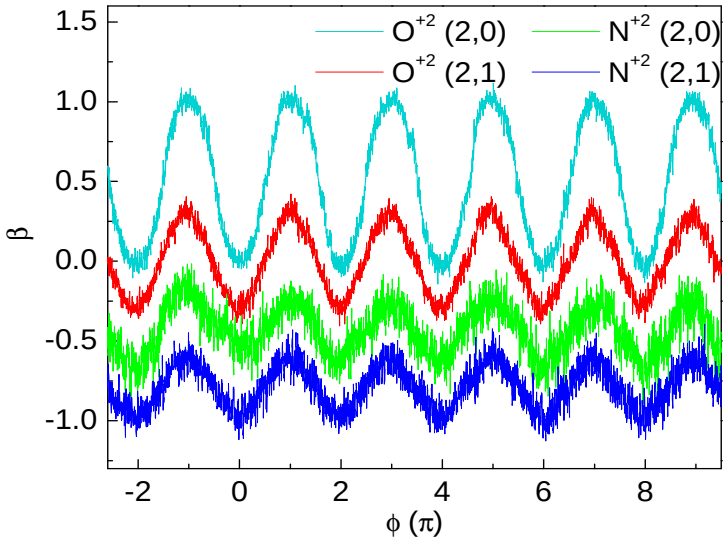

Figure 3.8: Asymmetry parameter vs. ϕ for the doubly-charged fragments from N_2(2,0), N_2(2,1), O_2(2,0), and O_2(2,1), obtained under identical laser conditions that are near optimal for maximizing the O_2(2,0) asymmetry. The β values have been vertically offset for clarity, but the amplitudes have been maintained.

introduced. Figure 3.9a illustrates this variation for the N_2(2,0) and N_2(2,1) channels, and Figure 3.9b shows the 400 nm pulse energy as a function of the BBO angle. As the BBO angle is tuned off of the optimal phase matching angle, the center frequency of the 400 nm light is shifted (i.e. ω_2=$2\omega_1 \pm \delta\omega$), and the spectrum is narrowed, as shown in Figure 3.10a for the BBO angles marked by arrows in Figure 3.9b. Figures 3.10b and 3.10c illustrate the two-color electric fields for the same BBO angles and experimental conditions as in Figure 3.9. Differences in amplitude result from different 800 nm and 400 nm intensities at the three BBO angles, and, while the field here is in arbitrary units, the $E_{2\omega}/E_{\omega}$ ratios have been maintained. Near t=0, the largest visible difference is in the small electric field modulations in the negative direction, but, looking farther away from the center of the pulse, the phase shift between the ω_2=$2\omega_1$ and the ω_2=$2\omega_1 \pm \delta\omega$ fields becomes apparent.

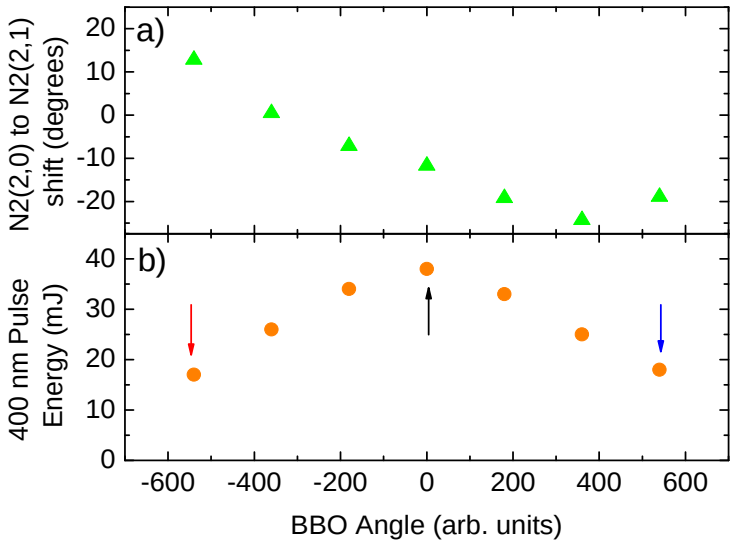

Figure 3.9: (a) Relative shift between maxima in the $N_2(2,0)$ and $N_2(2,1)$ channels and (b) 400 nm pulse energy as a function of BBO angle. "BBO angle" is related to the incidence angle, hence the phase matching, of the BBO crystal.

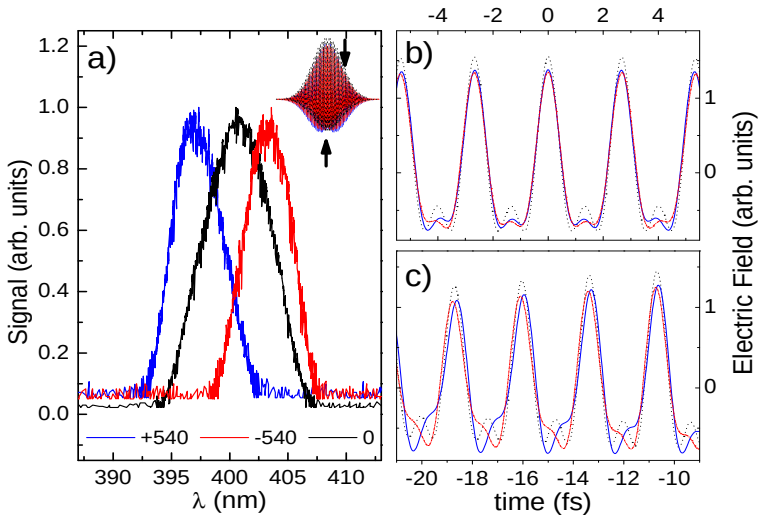

Figure 3.10: (a) Spectra of the frequency-doubled light for the three BBO crystal angles marked in Figure 3.9b. The two-color electric fields for the different phase-matching conditions zoomed in near (b) t=0, and (c) the full-width half-maximum (FWHM) of the pulse, as marked by arrows in the inset of part (a). Line color corresponding to BBO angle has been maintained throughout the two figures.

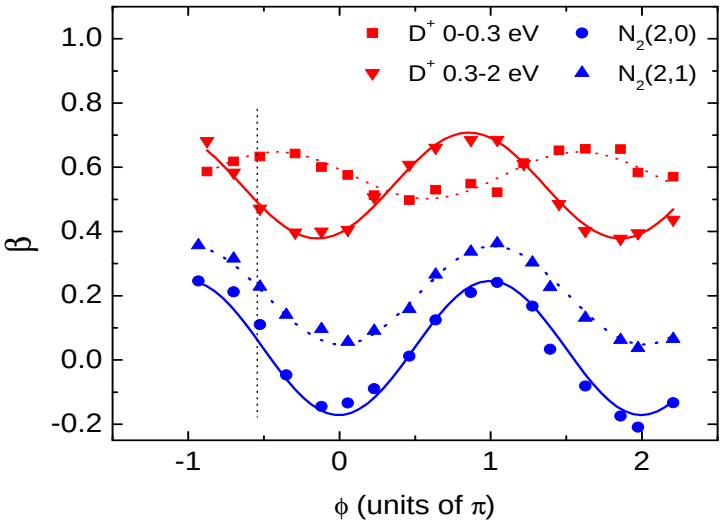

Figure 3.11: $N_2(2,0)$, $N_2(2,1)$, and two different D^+ dissociation channels (integrated over the specified energy ranges). The points represent the data taken in count mode, and the curved lines are fits to the data. The vertical dotted black line indicates the ϕ=0 assignment from [16], i.e. ϕ_{max} for the D^+ 0-0.3 eV channel lags ϕ=0 by $\sim \pi/6$.

In an attempt to eliminate the 0 or π ambiguity in ϕ_{max}, following Ray *et al.* [16], we measured the energy dependence of $\beta(\phi)$ for two-color dissociative ionization of D_2. In accordance with their results, we observed a pronounced variation in ϕ_{max} as a function of proton energy. However, as seen in Figure 3.11, our phase-assignment, based on the $N_2(2,0)$ standard, is inconsistent with their calibration [16] based on asymmetric high-energy electron yields from Xe. The difference in the two phase measurements may be the result of the intensity dependence of the different processes responsible for asymmetric dissociation in D_2^+ [85] and the likelihood that laser conditions in the two experiments were not identical.

As an alternative calibration, we compare our asymmetry results for the CO(2,2) channel [86] with those previously reported [21]. In this case, their absolute phase calibration, again

based on backscattered electrons from Xe, is consistent with our assignment from the $N_2(2,0)$ reference. If we adopt their calibration, as shown in Figure 3.8 and 3.11, *for all channels observed in our experiments*, fragments with the highest ionization potential (i.e. those that are the most difficult to produce via tunneling ionization) are preferentially emitted downfield.

3.4 Discussion

The ubiquity of the asymmetric emission suggests that it originates from a non-molecule-specific mechanism which depends primarily on the strength and asymmetry of the field rather than on the precise couplings between field-dressed molecular levels. We have, therefore, performed several auxiliary measurements in an attempt to identify it. First, we measured the full momentum distributions of the doubly-charged fragments from N_2, O_2, and CO. Results for O_2 are typical, and are shown in Figure 3.12; N_2 and CO data are shown in Figure 3.13. The ion angular distributions are highly anisotropic, with maxima oriented along the laser polarization axis. The distributions have no significant ϕ-dependence beyond the forward/backward asymmetry; even considering only fragments with large momenta in the directions transverse to the laser polarization axis results in an asymmetry amplitude equal to that of the entire distribution (see Figure 3.14).

By adding an intense, circularly polarized, time-delayed 800 nm probe pulse, Pinkham [86] previously found from Coulomb explosion measurements that the two-color beam creates a modest degree of transient molecular alignment [88]. However, he observed no evidence for transient orientation of the heteronuclear species, CO and HBr, either immediately following the two-color pulse or at rotational revivals [21]. Presumably, this was due to the broad rotational distribution of the (near) room temperature samples [88].

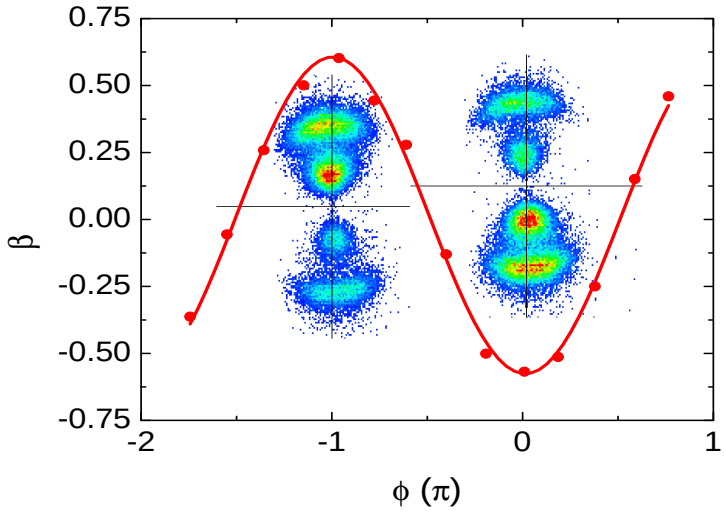

Figure 3.12: Measured asymmetry (red dots) vs ϕ for the O^{+2} fragment yield from the $O_2(2,0)$ channel obtained by integrating over the positive and negative y-momentum distributions. The solid red curve is a fit to the data. The left(right) insets show the p_y vs p_x momentum distributions of the O^{+2} ions from the $O_2(2,0)$ and $O_2(2,1)$ channels at $\phi = 0(\phi = \pi)$. The laser is polarized along the (vertical) y-axis.

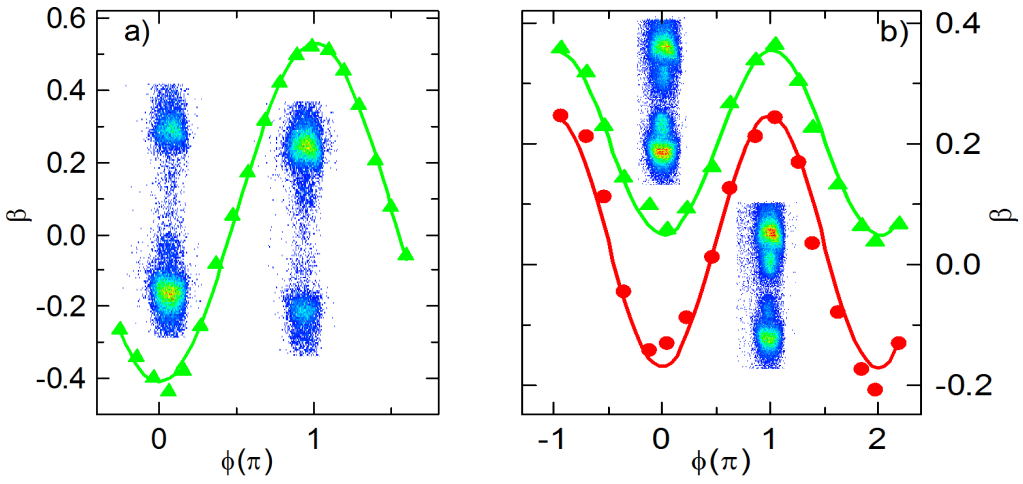

Figure 3.13: Count mode data for (a) the O^{+2} fragments from CO, and (b) the N^{+2} fragments from the $N_2(2,0)$ (red circles) and $N_2(2,1)$ (green triangles) channels. See Figure 3.12 for further explanation.

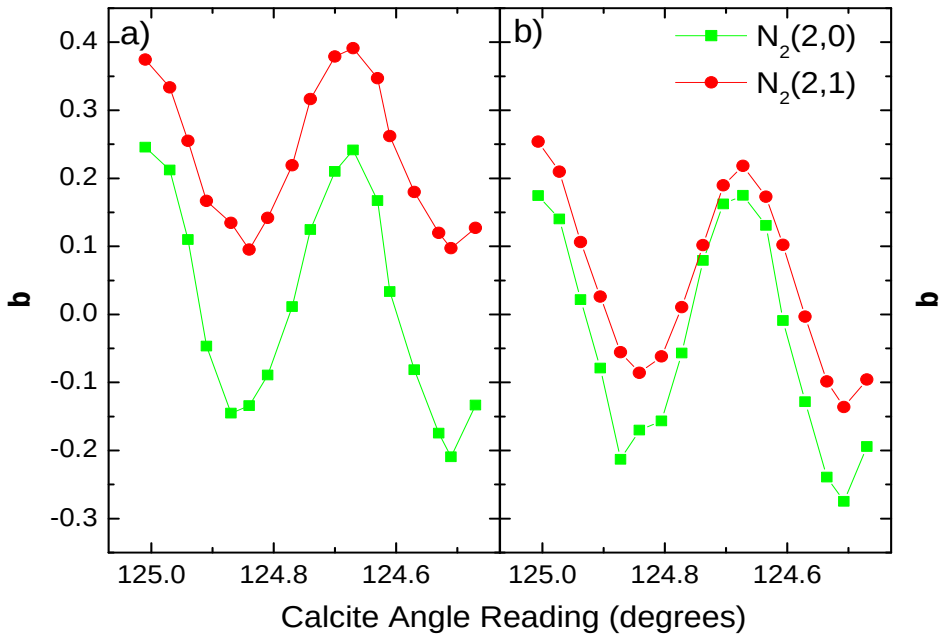

Figure 3.14: Asymmetry in the $N_2(2,0)$ and $N_2(2,1)$ channels as observed in count mode. By applying momentum filters to the data, we calculate β for (a) all hits; and (b) only those hits with $p_{trans} > 40$ atomic units (a.u.) and > 55 a.u. for the (2,0) and (2,1) channels, respectively. While the absolute values of β are shifted (due to a slight offset from p_{trans}=0 in the analysis), the amplitude of the asymmetry is preserved even in the very wings of the distribution.

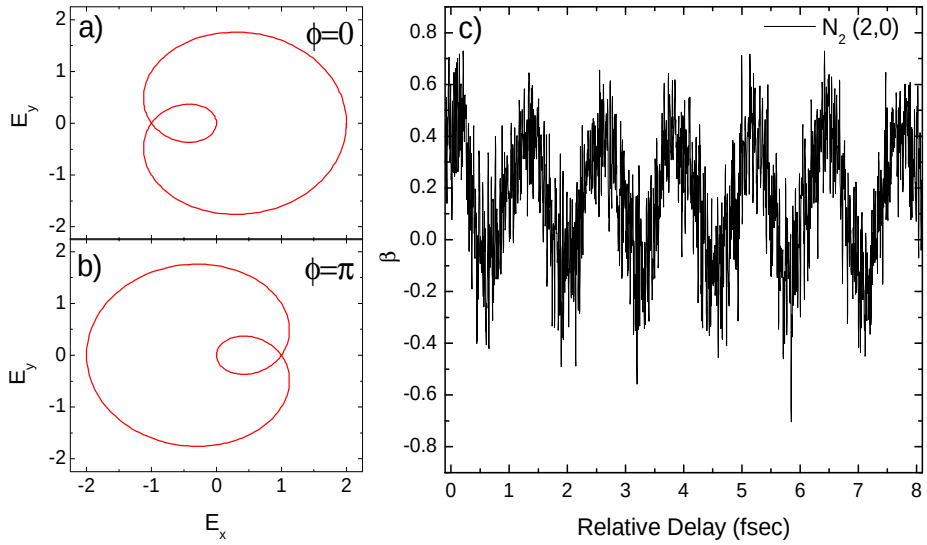

Figure 3.15: Representations of the circularly-polarized two-color electric field in the plane perpendicular to the laser propagation direction for (a)ϕ=0 and (b)ϕ=π. $E_\omega(t)$=$E_{2\omega}(t)$. (c) The asymmetry in the N_2(2,0) channel for near circularly polarized two-color field.

To determine if the observed asymmetry is the result of electron recollision [6, 9], $\lambda/4$-waveplates are employed to nearly circularly polarize the ω and 2ω beams. With this polarization, during each full-cycle, the two-color field vector traces out an epicycloid rather than a circle, with a pronounced ϕ-dependent field asymmetry in the polarization plane, as is illustrated in Figure 3.15. Electron recollisions should be suppressed in such a field, yet we observe asymmetries comparable to those measured with linear polarization.

Enhanced ionization (EI) of dissociating molecular ions at a critical internuclear separation, R_c, (or beyond R_c for non-Σ molecular orbitals [89]) is an established mechanism for producing multiply-charged ion fragments [38–40]. It involves tunnel ionization of electrons, localized on the upfield side of a molecule, through the "inner" potential barrier between ions. This mechanism is consistent with several features of the asymmetric dissociation we observe. First, EI is predicted to occur for a wide range of molecules. Second, it is most

effective for molecules aligned along the laser polarization axis, in accordance with the narrow fragment angular distributions we observe. Third, the exponential field-dependence of the tunneling ionization rate should lead to highly asymmetric emission in a two-color field, with the field asymmetry determining the direction of ion fragments with the highest ionization potential. Because the ionization rate is greater on the upfield side of the molecule, the ions that are most difficult to produce should be preferentially emitted from that side, i.e. in the direction of the field maximum. Indeed, calculations of dissociative ionization in two-color and few-cycle pulses in simpler systems show strong asymmetric emission, in the direction expected from the EI mechanism [90, 91]. However, the sign of the asymmetry we observe is precisely opposite to this if we adopt the phase calibration based on asymmetric electron rescattering [16, 21].

The physical source of this discrepancy is intriguing and important. One possibility is that MEDI in small molecules at these intensities is, in fact, not dominated by EI (or electron recollisions) [92] and charge-localization in the separating molecule favors the observed configuration for a different reason. Another is that the phase-calibration based on the directional asymmetry of high-energy electrons from Xe in a two-color field has the wrong sign [21]. In either case, the resolution of this issue may have significant implications for past and future studies of strong-field atomic and molecular dynamics.

3.5 Conclusion

In summary, we have observed strong, directional emission of multiply-charged ion fragments from dissociative ionization of a variety of molecules in two-color laser fields. All species exhibit the greatest forward/backward asymmetry when the field is maximally asymmetric. Based on an independent phase calibration, the sign of the asymmetry is opposite

to that expected from the standard EI model. The robustness of the asymmetries in N_2, O_2, and CO makes MEDI of any of these common species a convenient *in situ*, single-shot, phase-standard for experiments involving intense two-color fields.

3.6 Post Script

Since the writing of this Chapter, several private communications have revealed that the independent phase calibration has been repeated and a π discrepancy now appears to have been found [93, 94]. With this new assignment, the sign of the asymmetries in the directional fragment emission from N_2, O_2, and CO is in agreement with that expected from the standard enhanced ionization model.

Chapter 4

Interfacing Carrier-Envelope Phase Tagging and Cold Target Recoil Ion Momentum Spectroscopy

4.1 Introduction

As discussed in Section 1.4.1, asymmetric fields are a natural feature of few-cycle laser pulses. Since a free-running laser has a random pulse-to-pulse CE phase shift, studying the effects of these asymmetric laser pulses has, to date, required carrier-envelope (CE) phase stabilization. With this technique, the per-pulse CE phase shift, $\Delta\phi$, of the oscillator is locked, and subsequent pulse picking, amplification, additional phase locking, and pulse compression leads to few-cycle pulses with a known CE phase, ϕ [1]. The carrier-envelope phase has been shown to be important in many processes, including attosecond pulse generation [2], controlled electron emission from atoms [3–5], and electron localization in the dissociation of H_2 [6–8] and CO [9]. For the remainder of this work, the phrases

"phase-locked" and "phase-stabilized" will be used interchangeably.

The necessary steps for the generation CE phase-locked amplified few-cycle pulses are quite demanding, requiring multiple feedback loops to stabilize not only the oscillator CE phase, but also laser amplifier parameters such as temperature and power, all of which have a profound impact on $\Delta\phi$ of the amplified pulses [1, 95]. Often times, achievable lock times are only minutes or a few hours, which precludes their use for high-statistic experiments. Experiments performed using phase-locked pulses did, however, allow the demonstration of CE phase-measurement by above-threshold ionization in noble gas atoms [5]. This has now been developed into a single-shot phase measurement technique [70]. This so-called "phase meter" can be used in conjunction with a second, event-mode data collection method to "tag" each event with the laser pulse's CE phase for the extraction of the phase-dependence of atomic and molecular phenomena.

In this chapter, we discuss the first proof-of-principle experiments involving the interfacing of the phase-tagging technique with Cold Target Recoil Ion Momentum Spectroscopy (COLTRIMS) [96]. These experiments were performed in collaboration with the group of Dr. Matthias Kling at the AS-1 beamline at the Max Planck Institute for Quantum Optics in Garching, Germany. The momentum of the Ar^{+2} ions created by nonsequential double ionization (NSDI) of argon has previously been shown to be phase-dependent [3], and the phase dependence of the NSDI yield has recently been investigated with quantitative rescattering theory [97], so we use this as our target system. With the single-shot phase-tagging technique, the asymmetry in the directional emission of the Ar^{+2} ions is measured to be ± 0.5, and the phase-dependent Ar^{+2} yield is found to be in good agreement with theoretical calculations [97]. We are also able to extend data collection times up to several days and achieve a phase uncertainty of < 210 mrad.

4.2 Principles of the Stereo-ATI Phase Meter

As its name implies, stereo-ATI is based upon the phenomenon known as above threshold ionization (ATI) [29], whereby an electron absorbs many more photons than are necessary for ionization. Further discussion of this process is presented in Section 1.2.2. This process has a highly non-linear dependence on the laser electric field, which, recalling Section 1.4.1, depends upon ϕ for few-cycle pulses ($E(t) = E_0(t)\cos(\omega t + \phi)$), making it an ideal process for the study of phase effects.

In 2001, Paulus *et. al.* published the results of the first experimental demonstration of few-cycle pulse phase effects on a physical system [4]. Using two opposed detectors, they found an anti-correlation in the total yield of photoelectrons from ATI of krypton emitted to the left and right for each laser shot. Two years later, they expanded upon this idea to measure the CE phase for phase-stabilized laser pulses [5]. Focusing on the highest-energy ATI electrons (those in the "plateau region") from xenon, which have a much stronger CE phase-dependence than lower-energy electrons, and comparing the left vs. right electron yields to classical simulation results allowed them to infer the CE phase with an estimated error of $\pi/10$ with no $\pm\pi$ ambiguity.

Further development of this technique lead to the creation of a truly single-shot phase detector only two years ago [70]. It was known that the directional asymmetry of high energy photoelectrons in the plateau had a near sinusoidal ϕ dependence [5], i.e. $\beta = \cos(\phi + \phi_0)$, and further work revealed an energy-dependent phase shift in β within these high energy electrons [98]. By subdividing the plateau region, one could exploit the phase shift between the asymmetry parameters for two different regions [98]. Plotting β_1 vs. β_2, where the subscripts 1 and 2 indicate the two energy regions, in a parametric asymmetry plot (PAP, also referred to as a "phase potato") became an easy way to visualize the CE phase of

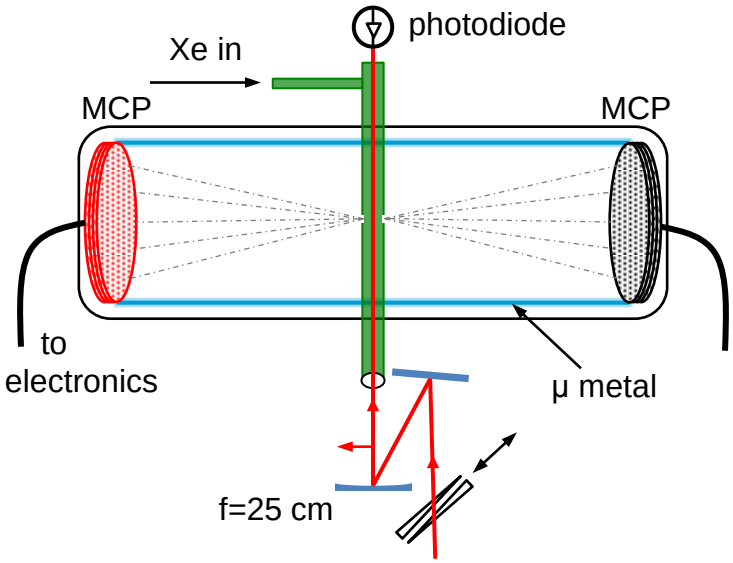

Figure 4.1: Overhead view of the stereo-ATI phase meter. MCP: microchannel plate stack. See the text for details.

each laser pulse. Note that each pulse generates a single point on the PAP. The CE phase for every pulse is uniquely determined from the PAP, with the standard deviation in the measurement precision as low as $\pi/300$ [70], an unprecedented level of precision. Chen *et. al.* introduced a technique based upon quantitative rescattering theory to extract the pulse duration, intensity, and CE phase directly from this experimental data [99], and further work has offered more insights into optimizing conditions for data collection and analysis [100].

The details of the stereo-ATI single-shot phase meter used in our experiments are shown schematically in Figure 4.1. Two (ideally) identical MCP detectors are diametrically opposed to one another about a central interaction region inside a μ metal-shielded vacuum chamber. Xenon gas fills the inner (green) tube, which is colinear with the laser propagation direction, to a pressure of 6.5 $\times 10^{-3}$ mbar. This high pressure ensures the detection of many

electrons per laser shot, a necessity for the single-shot operation of the phase meter. Differential pumping maintains pressure in the remainder of the chamber at 1-5 $\times 10^{-5}$ mbar, a safe operating pressure for the MCPs. A small fraction, approximately 30 μJ per pulse, of each few-cycle laser pulse produced by the AS-1 beamline is linearly polarized along the spectrometer axis and focused into the interaction region with an f = 25 cm mirror. A pair of moveable wedges exterior to the chamber allow for optimization of the pulse chirp. Two small holes on either side of the gas confinement tube allow electrons emitted within 2° of the polarization axis to propagate towards the two detectors. A small repeller voltage of $\sim$-25 V prevents the low-energy electrons from hitting the detectors, thus allowing only the high-energy, plateau-region electrons to be detected.

Using specially designed integrator circuitry [100, 101], one sets gates about the two desired energy regions by viewing the electron time-of-flight spectra on an oscilloscope, and the electron currents within these gates for both detectors are integrated and rapidly converted to four distinct voltages. From these voltages, the circuitry calculates the energy region-dependent asymmetry parameters, β_1 and β_2, in $\sim$ 20 μs, and these signals can be viewed on an oscilloscope or sent directly to the ADC card in the VME crate for data collection (see Section 2.4.7). Figure 4.2 illustrates the electron time-of-flight spectra collected at the black and red detectors for two different values of ϕ. The yellow and blue shaded areas indicate the high- and low-energy regions used for the asymmetry calculations and phase determination. An example PAP is included in Figure 4.2(c). The size and shape of this PAP depends upon laser intensity and pulse duration, the TOF regions selected, and inequalities between the two detectors. However, accurate retrieval of the absolute phase has been shown to be independent of the TOF regions selected [99], and the shape can be compensated for, as described below.

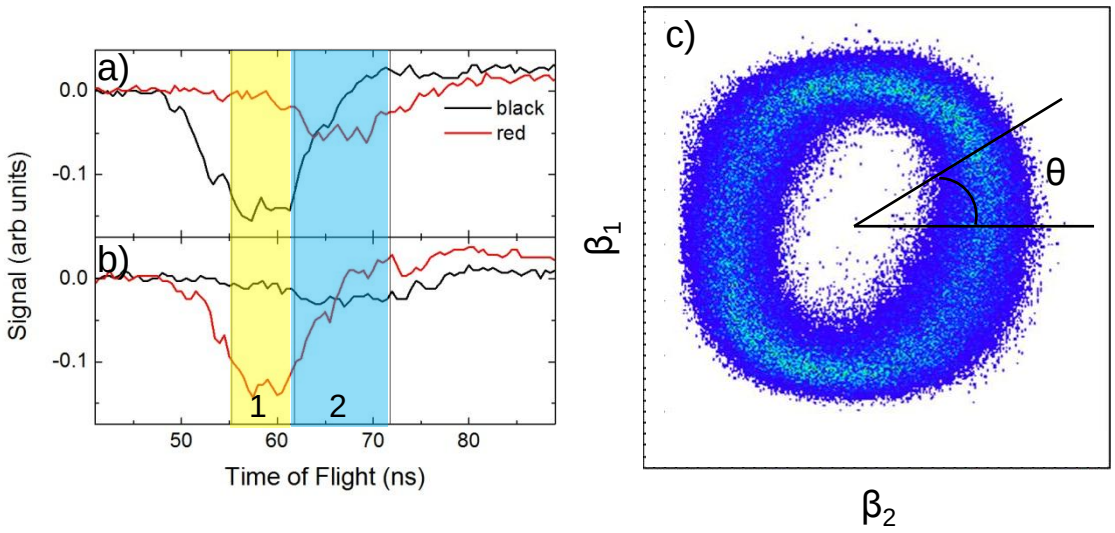

Figure 4.2: (a) and (b) Time-of-flight spectra for electrons incident on the left (red) and right (black) phase meter detectors for two different carrier-envelope phases. (c) The parametric asymmetry plot ("phase potato") generated by plotting the β parameter for the high energy region (1, yellow shading in (a) and (b)) vs. that for the low-energy region (2, blue). The polar angle, θ is related to the CE phase.

In this method, the polar angle, θ, of the PAP is related to the actual CE phase, ϕ, but it is still necessary to find the exact relationship. If the laser is free-running (i.e. non-CE phase-stabilized) with a random CE phase variation, then the CE phase distribution is uniform over the full 2π range. Thus, for a sufficiently large number of laser shots, every equally-sized ϕ region must contain the same number of counts, and

$$d\phi = \frac{\rho(\theta)}{\langle\rho\rangle} d\theta = \lambda(\theta) d\theta \longrightarrow \phi(\theta) = \phi_0 + \int_0^{\theta} \lambda(\theta') d\theta' \tag{4.1}$$

where $\rho(\theta)$ is the density of laser shots as a function of θ, $\langle\rho\rangle$ is the average density, and $\lambda(\theta) \equiv \rho(\theta)/\langle\rho\rangle$. Additionally, if the two detectors are identical and the energy regions are perfectly selected such that the phase dependence of their asymmetry parameters are 90° out of phase, i.e.

$$\beta_1 = \frac{Y_{L1} - Y_{R1}}{Y_{L1} + Y_{R1}} \approx \sin(\phi + \phi_0) \tag{4.2}$$

$$\beta_2 = \frac{Y_{L2} - Y_{R2}}{Y_{L2} + Y_{R2}} \approx \cos(\phi + \phi_0), \tag{4.3}$$

then the phase potato radius and change in radius will be independent of θ. This means that

$$\phi(\theta) = \theta + \phi_0 \tag{4.4}$$

and the phase potato will be a uniform circle. By careful optimization of experimental conditions, this can be nearly achieved, but ϕ can be retrieved for even very elongated potatoes [100]. The assumption of random CE phase variations can be verified by inserting an incremental amount of glass into the beam path and observing no change in the phase

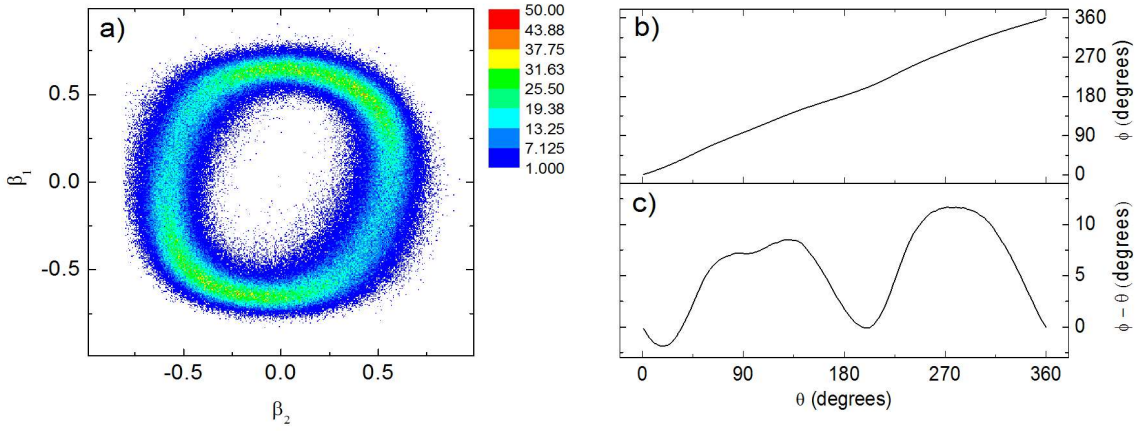

Figure 4.3: (a) An unbiased parametric asymmetry plot. From this data, integration via Equation 4.1 results in (b) $\phi(\theta)$ vs. θ. This is also plotted as $\phi(\theta) - \theta$ vs. θ in (c) to illustrate the nonlinearities.

potato. Alternatively, we can use a modification of our phase tagging technique, described in Section 4.5, to verify the assumption.

To retrieve ϕ, it is necessary to collect a phase potato reference scan, in which the phase of every single laser shot is collected. As the full COLTRIMS/stereo-ATI setup records data only when there is an ionization event inside the COLTRIMS chamber, which may be ϕ-dependent, we remove the COLTRIMS apparatus from the data collection hardware and record an unbiased, every-single-laser shot reference phase potato. We then use the unbiased reference scan to perform the integration in Equation 4.1 to get the proper θ-to-ϕ conversion (up to the constant, ϕ_0), and apply that conversion to the raw data. The necessary conversion is easily visualized by plotting ϕ vs. θ (see Figure 4.3). The closer this is to a straight line at 45°, the more optimally the experimental parameters have been set. For some measurements, it may be desirable to have increased resolution along a certain CE phase range. In this case, intentional distortion of the phase potato from round can

create regions of higher or lower ϕ resolution [70].

4.3 Experimental Setup

The experiments described in this chapter were performed at the AS-1 beamline at the Max Planck Institute for Quanutm Optics in Garching, Germany. The optical setup is sketched in Figure 4.4. Approximately 17% of the amplified, compressed laser light (central wavelength 750 nm, pulse duration < 5 fs) is directed towards the stereo-ATI phase meter, details of which are given in Section 4.2, while the remainder of it propagates towards the COLTRIMS experimental chamber. Pairs of moveable glass wedges are used to optimize the pulse duration in each chamber, and the laser intensity in each arm is controlled by apertures in the beam path. Because of the different beam paths, the CE phase inside the COLTRIMS chamber is not the same as that in the stereo-ATI chamber, i.e. $\phi_{COLTRIMS} \neq \phi_{Stereo-ATI}$. However, since the beam paths are not changing, the difference between the two phases, $\Delta\phi = \phi_{stereo-ATI} - \phi_{COLTRIMS}$, is constant, so phase measurement in a separate chamber is adequate to determine $\phi_{COLTRIMS}$.

Argon enters the interaction region of the COLTRIMS chamber via a supersonic jet. An f = 25 cm mirror focuses the light just before the gas jet in order to minimize the Gouy phase shift associated with the focus [102]. A $\sim$ 1.25 V/cm electric field guides the ions towards a time- and position-sensitive detector composed of a stack of microchannel plates (MCP) backed by a delay line anode (DLA). Signals from the MCP and DLA are amplified, discriminated, and collected with a TDC card. The energy-specific asymmetry parameters from the phase meter electronics are collected with an ADC card. A photodiode located after the stereo-ATI chamber provides the master trigger for the data collection electronics, ensuring that information from each experiment is simultaneously recorded for each event.

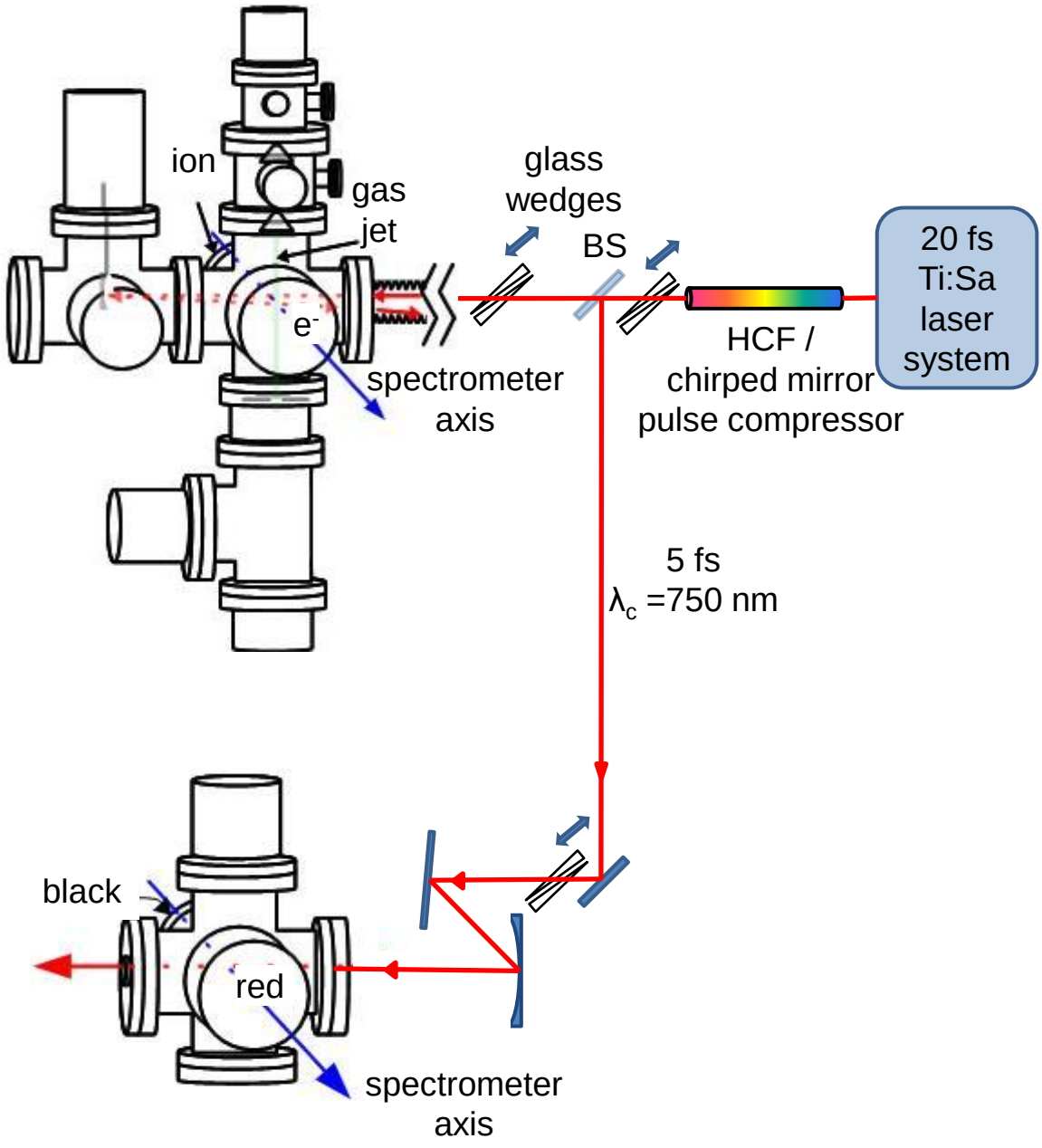

Figure 4.4: Beam path for the MPQ phase tagging setup. After the hollow core fiber (HCF) / chirped mirror compressor, 17% of the light is sent into the stereo-ATI phase meter, while the remainder is sent into the experimental chamber. Glass wedges allow for optimization of the pulse's chirp. Ti:Sa: Ti:Sapphire; BS: Beam splitter; ion, e^-, red and black: detectors.

Online monitoring of the data acquisition and subsequent offline analysis is performed with the Go4 software package.

To collect the unbiased phase potato for the the $\theta \rightarrow \phi$ conversion, we simply remove the TDC card from data collection, and record the phase meter data for every single laser shot for 5-10 minutes. This is done prior to and following each data run and in the event of a change in the laser parameters. Generally speaking, the major ϕ-dependent features are visible regardless of which unbiased data collection is used for the conversion. Additionally, as long as the COLTRIMS data includes a large number of counts from H_2^+, H_2O^+, or another channel whose yield is easily saturated at all values of ϕ for the given laser conditions, the phase potato from the data run itself provides a similar phase conversion (although using these PAPs for the conversion is generally avoided). The difference between using an unbiased reference phase potato and one collected simultaneously with COLTRIMS data is illustrated in Figure 4.5.

4.4 Results

Figure 4.6a shows an example time-of-flight spectrum for the Ar^{+2} ions, as recorded with the Go4 data analysis software. The laser polarization lies along the spectrometer axis, and ions will have initial momentum either towards or away from the detector. Unlike the molecular dissociations described in Chapter 3, the atomic ionizations studied here do not create highly-energetic ion fragments, so there are not distinct "forward" and "backward" peaks in the time-of-flight spectrum. (Typically, NSDI does create a "double-hump" structure in the longitudinal momentum distribution, which may be visible in the TOF if the spectrometer resolution is high enough. The absence of this structure in our Ar data is discussed below.) Some versions of the analysis code also allow preliminary on-line monitoring of CE phase

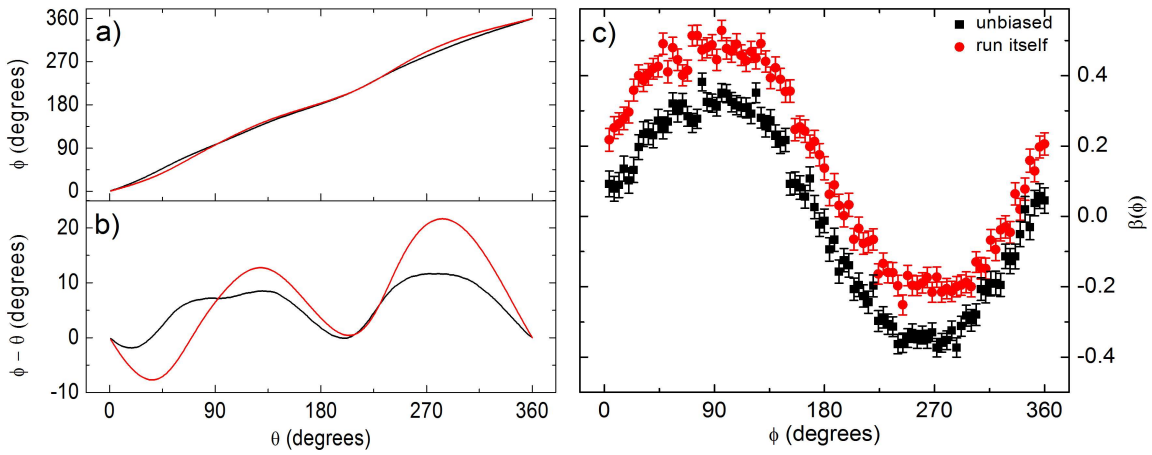

Figure 4.5: Comparison of two $\phi(\theta)$ retrievals for the same Ar^{+2} data set. (a) and (b) are similar to Figure 4.3b and c; (c) the resulting asymmetry parameters for the Ar^{+2} ions (see also Section 4.4 and Figure 4.7). The black curves were obtained by using an unbiased phase potato for the conversion; the red curves were obtained using the phase potato collected simultaneously with the Ar^{+2} data in the COLTRIMS chamber. The red data in (c) has been vertically offset for clarity.

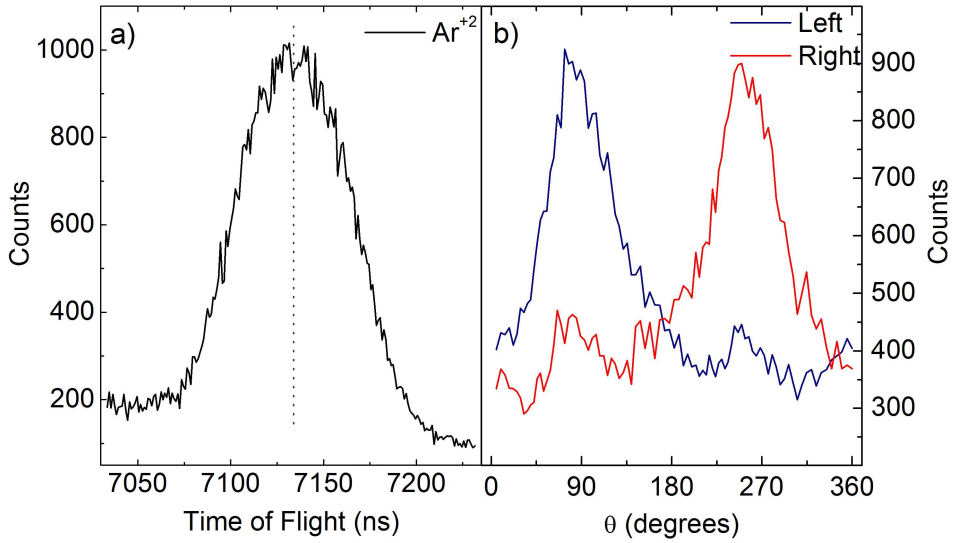

Figure 4.6: (a) Time-of-flight spectrum for the Ar^{+2} ions. (b) Time-of-flight yields to the left and right of the vertical line in (a) as a function of the measured phase, θ.

effects by dividing the Ar^{+2} TOF peak into a left (forward, towards the detector) and a right (backward, away from the detector) half and then monitoring the ion yields in the two halves as a function of the measured CE phase-related angle, θ. This is illustrated in Figure 4.6b. Strong anti-correlated modulations in the number of ions in the left and right gates are visible, with nearly 3 times as many ions traveling in one direction versus the other at optimal phases.

Subsequent off-line analysis allows the conversion of the measured θ values to ϕ and the calculation of the asymmetry parameter, $\beta(\phi)$, associated with the time-of-flight yield modulations. As in the two-color field experiments, we define

$$\beta(\phi) = \frac{Y_f(\phi) - Y_b(\phi)}{Y_f(\phi) + Y_b(\phi)}. \tag{4.5}$$

Figure 4.7 combines the TOF spectrum (a) with the extracted CE phase, ϕ, in a contour plot (b). The peak modulations present in the line plot in Figure 4.6 are now cleanly visible as islands in the TOF-vs.-ϕ space. Additionally, the asymmetry parameter is plotted in Figure 4.7c; peak β values of ± 0.4 are easily attainable with even this rudimentary filtering method.

The entire COLTRIMS technique is predicated on the retrieval of the momentum of the charged particles created in an ionization or dissociation event, and Figure 4.8 illustrates the retrieved momentum of the Ar^{+2} ions. Due to their low kinetic energy, the ions are well-localized in the dimensions along and transverse to the laser polarization. Because of the velocity of the ions in the jet, the distribution is slightly wider in the $\hat{y}$ (jet) direction. The momentum distribution along the laser polarization is of most interest, and this 1-dimensional spectrum is shown in Figure 4.9.

From the longitudinal momentum distributions, we can make *in situ* determinations of

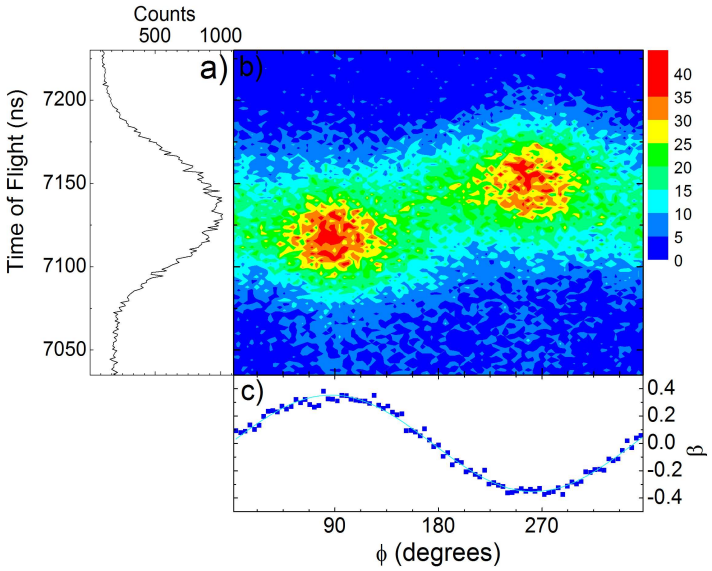

Figure 4.7: (a) Ar^{+2} time-of-flight spectrum. (b) The same TOF vs. carrier-envelope phase, ϕ, and (c) the resulting asymmetry parameter. The solid line is a sinusoidal fit to the data.

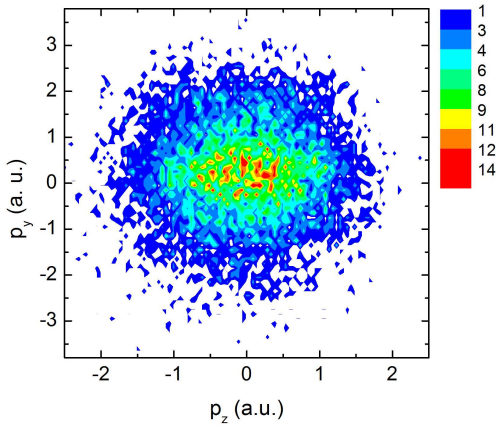

Figure 4.8: The transverse vs. longitudinal momentum of the Ar^{+2} ions. $\hat{y}$ is the direction of the gas jet.

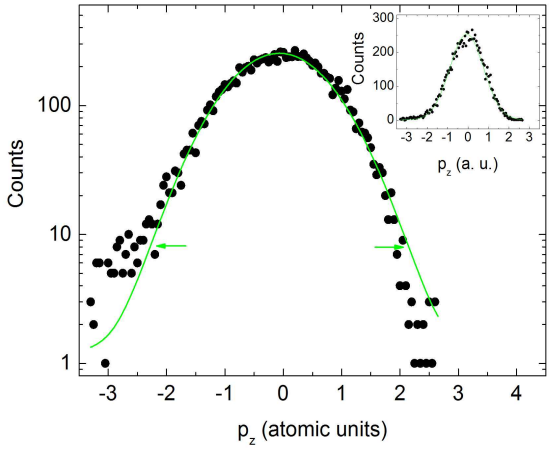

Figure 4.9: Ar^{+2} fragment momentum along the spectrometer axis. Black circles: data; green line: Gaussian fit. The horizontal arrows correspond to approximate values of $p_{\parallel}^{max}$. The inset is the same data represented on a wider momentum span with a linear vertical axis.

the laser intensity, I. As per [103, 104] (see also Appendix B), the maximum drift momentum that an ion can obtain from a linearly polarized laser field is

$$p_{\parallel}^{max} = 2n\sqrt{U_p} \tag{4.6}$$

where n is the charge state of the ion and $p_{\parallel} = p_z$ in this work. The ponderomotive energy, or the cycle-averaged quiver energy of a free electron in the laser field, U_p, is related to the laser intensity by

$$U_p = \frac{I}{4\omega^2}, \tag{4.7}$$

and by rearranging and substituting for U_p, we obtain

$$I = \frac{(\omega p_{\parallel}^{max})^2}{n^2}. \tag{4.8}$$

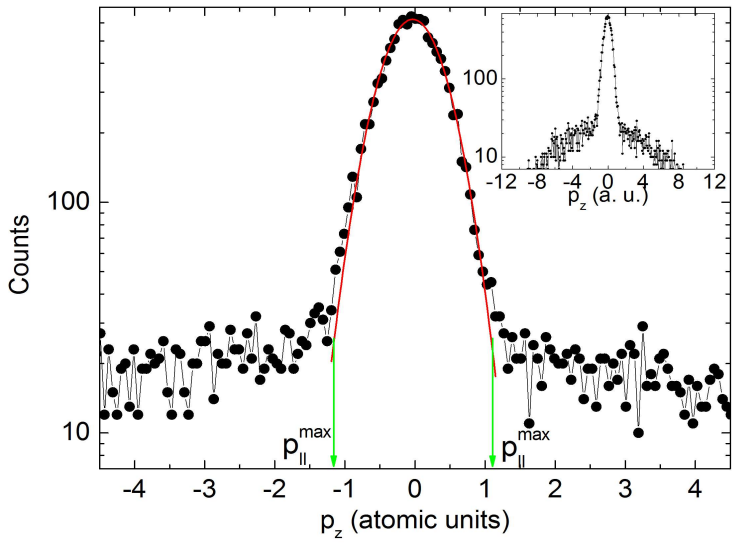

Figure 4.10: H_2O^+ fragment momentum along the spectrometer axis. Black circles: data; red curve: Gaussian fit. From the deviation of the peak from the pedestal, the $p_{\|}^{max}$ can be extracted, as indicated by the green arrows. The inset illustrates the same data but with a wider momentum span.

To determine $p_{\|}^{max}$, we fit the experimental momentum data with a Gaussian and look for the momentum values at which the fit begins to pull away from the data. This is illustrated in Figure 4.10 for the H_2O^+ ions collected simultaneously with the Ar^{+2} data in Figure 4.9. In principle, any ion species can be used for the intensity calculation; we use H_2O^+ because it has a clean change of slope where the large peak from the jet meets the broad pedestal due to the background gas. Also, unlike the Ar^+ flux, it does not saturate the detector. For the H_20^+, $p_{\|}^{max}$ = 1.11 a. u. and I=1.6 $\times 10^{14}$ W/cm^2. Precisely determining $p_{\|}^{max}$ is prone to some error, but an intensity range of I = 1.3-1.8 $\times 10^{14}$ W/cm^2 is obtained for a $p_{\|}^{max}$ = 0.995-1.17 a. u. Similar analysis for the Ar^{+2} ions yields I=1.6 $\times 10^{14}$ W/cm^2; however, Figure 4.9 illustrates that the shoulder is not as prevalent as for the H_2O^+, which makes this a less optimal peak to use for the intensity calculation. The lack of a broad pedestal

most likely due to the Ar^{+2} originating entirely from the cold jet and also to tighter gating conditions in the Ar^{+2} analysis.

4.5 Discussion

As seen in Figure 4.9, the momentum parallel to the spectrometer axis, p_z, does not exhibit the classic double-hump structure observed in most NSDI experiments [103, 104]. However, if we divide the data into ten consecutive ϕ regions, as in Figure 4.11a-j, we can clearly see the momentum peak shifting smoothly between positive and negative momentum. It is believed that the reason for the single peak, as opposed to the double-hump structure is the reduced intensity (1.6×10^{14} W/cm^2) used in this experiment as compared to 3.5×10^{14} W/cm^2 in [3].

Recently, the total Ar^{+2} yield was predicted to be CE phase-dependent in work applying quantitative rescattering theory to NSDI [105]. From Figure 4.11 we see that, in addition to the shifting momentum, the total yield is exhibiting ϕ-dependent modulations. Figure 4.12 plots the total Ar^{+2} from the same data set as in Figure 4.11 as a function of phase, and two maxima and minima are observed. Overlaying the theoretical Ar^{+2} vs. ϕ curves indicates good agreement for the intensity that we have calculated. This analysis can also be used to assign the absolute phase of the asymmetry. Recall that $\phi(\theta) = \theta + \phi_0$, and thus far, we have assumed ϕ_0=0. The experimental CE phase offset has been chosen such that the minima in the experimental data corresponds to that in the theoretical curves, i.e. $\phi_0 = 110°$. By considering the ion momenta, we can resolve the $\pm\pi$ ambiguity that is inherent in the periodicity of the Ar^{+2} yield modulations. For ionization in a laser field $\vec{E}(t) = E_0(t)cos(\omega t + \phi)\hat{z}$ with $\phi = 0$, the electron will initially travel against the electric field maximum, then be returned to the ion core and the two electrons involved in

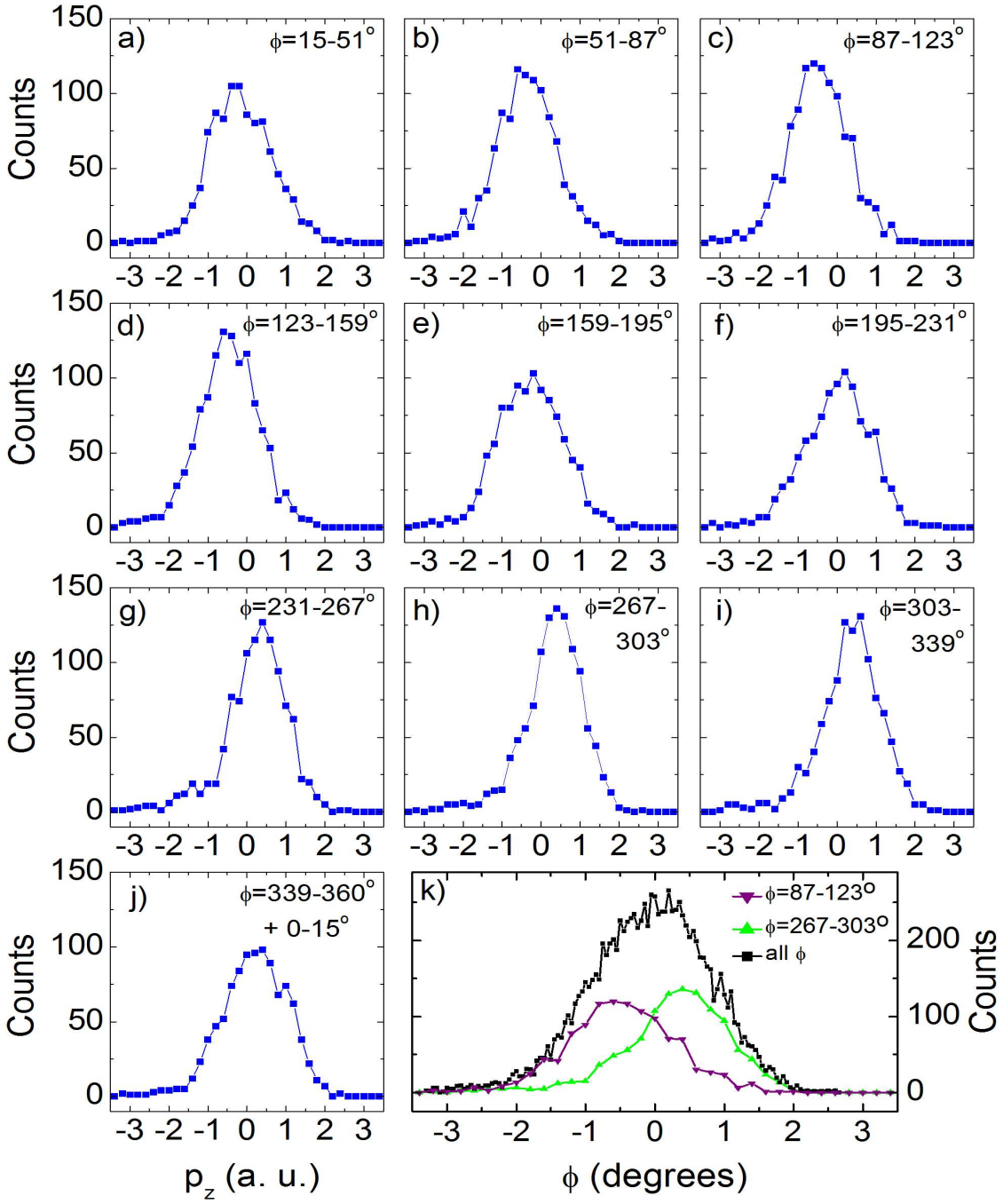

Figure 4.11: (a)-(j) Longitudinal momentum of the Ar^{+2} ions in consecutive ϕ regions. (k) Longitudinal momentum for two ϕ regions (green and purple triangles) as it compares to the momentum distribution integrated over ϕ (black squares).

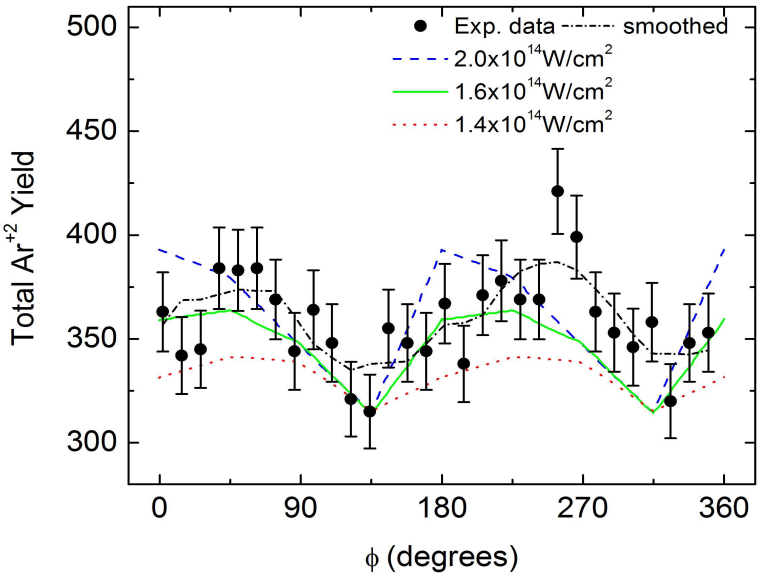

Figure 4.12: Black dots represent the experimental total yield of the Ar^{+2} ions as a function of CE phase; the data set is the same as in Figure 4.11. This data, after smoothing, is plotted as the black dot-dashed line. The theoretical intensity-dependent yields are taken from [105]. The CE phase offset, ϕ_0, has been chosen so that the minima in the experimental data and theoretical curves match. The vertical axis reflects the raw data yield, and the vertical of the theoretical curves have been scaled to match the minimum of the experimental data.

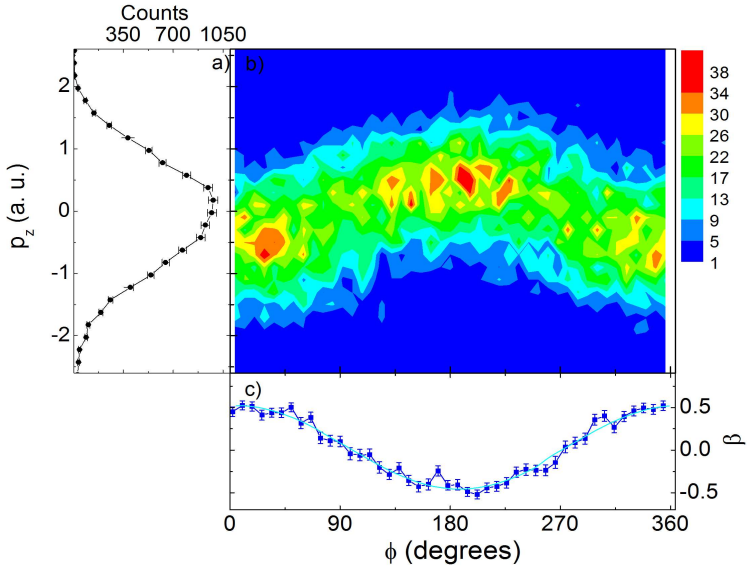

Figure 4.13: (a) The longitudinal momentum spectrum of the Ar^{+2} ions. (b) Longitudinal momentum vs. CE phase, and (c) the resulting asymmetry parameter.

the (e,2e) process will obtain final momentum in the positive direction, that is, in the same direction as the electric-field maximum at the time of ionization (see [103] and Appendix B). Conservation of momentum requires that the ion obtain recoil momentum in the opposite direction, so we assign $\phi = 0$ for maximum longitudinal momentum in the negative direction. This absolute phase assignment is illustrated in Figure 4.13. Panel (b) is a contour plot in p_z vs. ϕ space. This data set shows less distinct islands, but the asymmetry parameter (c) has larger peak β values of ± 0.5, than those observed in Figure 4.7. Note that Figures 4.7 and 4.13 represent two different data sets; the consistency in the degree of asymmetry is typical. The loss of the island structure may be due to intensity differences between the two runs.

Until now, no measurements of the ion yield purely as a function of CE phase have been made. This is partly due to limits on the duration of data acquisitions at each CE phase

due to lock stability, but more so because previous measurements have used addition of glass to the beam path to change the phase [3, 6, 8, 9]. Along with changing the CE phase, the addition of glass to the beam path also changes the pulse duration and peak intensity by imparting chirp to the pulse. Our method eliminates the need for a varying amount of glass, thus keeping the pulse intensity and duration the same for each pulse, effectively decoupling the effects of the CE phase. In addition, we also have the laser stability to make sufficiently long measurements for good statistics.

The error in the single-shot phase determination, $\Delta\phi(\theta)$, is influenced mainly by statistical error in the electron counting and intensity fluctuations, and it may, in general, be difficult to determine from the PAP data. However, for a nearly round PAP, we can approximate $\Delta\phi \simeq \Delta\theta \simeq \Delta r/r$ [100]. From this, we calculate $\Delta\phi < 210$ mrad for the data in Figure 4.13. This value is similar to the rms phase variation in experiments using a stereo-ATI as a feedback mechanism for phase-locking [106]; however, our simplified setup obviates the need for complex locking techniques and affords much longer data collection times. Previous experiments employing phase locking have had signal-to-noise ratios limited by the duration of the locks [3, 8]. While these particular proof-of-principle experiments were terminated after 3-5 hours, data acquisition times have been extended to several days with improvement of the stabilization unit that couples the amplified laser light in the hollow core fiber. Additionally, our CE phase measurement is made after pulse compression in the hollow core fiber and propagation through air, thereby accounting for all accumulated phase fluctuations, whereas previous CE phase determination has been performed prior to pulse compression [1, 107].

Chen *et. al.* [99] stated in a subsequent analysis of the first phase meter experiment [70] that the consecutive pulses from a free-running laser amplifier exhibit random CE phase

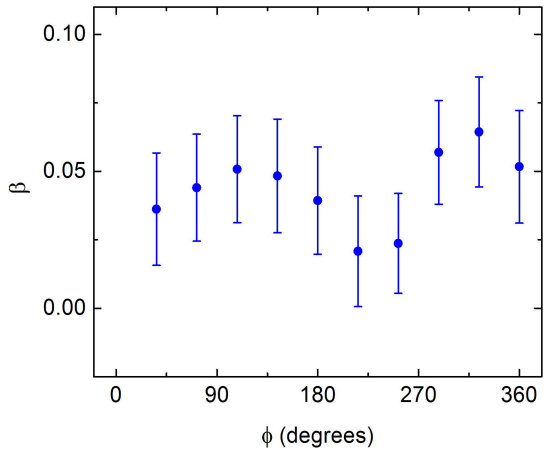

Figure 4.14: The asymmetry parameter for Ar^{+2} data analogous to Figure 4.7c but with the phase information from pulse n binned with the COLTRIMS information from pulse $n+1$. The lack of any statistically significant asymmetry confirms the random pulse-to-pulse CE phase shift for a free-running laser.

shift. Our experiment offers direct proof of this concept: By delaying the signals from the stereo-ATI with respect to those from the COLTRIMS chamber and binning the phase information from pulse n with the dissociation even information from pulse $n+1$, no phase dependence in the directionality of the Ar^{+2} ions was observed, as illustrated in Figure 4.14. If there was a non-random pulse-to-pulse phase relationship, it would be expected to manifest itself in this configuration; a lack of phase dependence in the (pulse n, pulse $n+1$) scheme confirms the random pulse-to-pulse phase variations from a free-running laser amplifier.

There are two main mechanisms thought to be responsible for nonsequential double ionization. In the first, after tunnel ionization and propagation in the laser field, the ionized electron returns to the ion core and immediately induces the ionization of a second electron. The two electrons then depart from the ion in the same direction. This method is known as recollision-induced direct ionization, or RIDI [103, 108]. In the second mechanism, the

returning electron excites a second electron, which is tunnel ionized by a subsequent laser electric field cycle. Electrons involved in this recollision induced excitation plus tunneling (RIET), also known as recollision-induced excitation with subsequent ionization (RESI), do not have a clear momentum correlation, as it depends upon the sign of the electric field that induces the second tunnel ionization event. The effects of laser wavelength, intensity, and pulse duration on these two mechanisms have been studied previously [3, 103, 104, 109–112]. Because of the correlated electron momentum, the longitudinal momentum of ions produced via RIDI is predicted to be bimodal, peaked at two non-zero values, and the distribution should be ϕ-dependent [111]. On the other hand, the independence of the electron motion in RIET leads to an ion momentum distribution peaked about zero [103]. When integrated over all CE phases, our Ar^{+2} momentum data exhibits a single peak centered around zero. However, the data shows strong ϕ dependence, with peak β values of $\pm$ 0.5. Thus, despite the lack of a bimodal longitudinal momentum structure, we believe that RIDI is the dominant mechanism for NSDI under our experimental conditions.

4.6 Conclusion

We have demonstrated, for the first time, the interface of the novel single-shot stereo-ATI phase meter with Cold Target Recoil Ion Momentum Spectroscopy. Our proof-of-principle measurement of carrier-envelope phase effects in nonsequential double ionization of argon illustrated continuous data collection for more than 5 hours, forward/backward peak asymmetry parameters of $\beta \pm 0.5$, and phase error of 210 mrad. This work has since been expanded upon to include NSDI in Ar, Ne, N_2, O_2, and CO with coincident ion and electron detection.

Chapter 5

Investigating Molecular Dynamics with Few-Cycle Pulses

5.1 Introduction

Understanding the coupled electronic and nuclear dynamics during dissociative ionization is a goal of much of the research involving molecules in strong laser fields. From our previous studies [113] and the work of others [14–20], we know that dissociative ionization is sensitive to the relative phase of a two-color laser field. The standard model for multielectron dissociative ionization (MEDI) is enhanced ionization (EI) [38, 39], in which, after one or two electrons are removed by tunnel ionization, the molecular bond begins to weaken and the nuclei to separate. When their internuclear distance has reached some critical value, R_c, it becomes very easy to remove additional electrons if the laser field is still present, leading to Coulomb explosion of the atomic ions. The rapid removal of electrons at R_c is facilitated by tunneling ionization through the potential well barrier between the separating charges. Enhanced ionization is discussed further in Section 1.3.1. This phenomenon is predicted

to occur for molecules of different highest occupied molecular orbital (HOMO) structures [89], and the exponential field dependence of the tunneling ionization rate should lead to highly directional-dependent emission in an asymmetric field. This model has successfully explained the observation of kinetic energy releases being lower than expected for Coulomb explosion at the equilibrium bond distance [39], and the high directionality of the ion fragments following Coulomb explosion of unaligned molecules. In addition, the required delay between the initial and subsequent ionization steps in EI has been observed in pump-probe experiments exploring MEDI of I_2 [40, 114]. All of these factors support the notion that EI may be responsible for the directional emission of fragments observed in the two-color field described in Chapter 3. Importantly, however, the directionality appears to be opposite to that expected from the most naive model.

The time scale for a small doubly-charged diatomic molecular ion, such as N_2^{+2}, to undergo ionization and expansion from $R_e \approx 2.1$ a.u. to $R_c \approx 8$ a.u. via a nearly Coulombic $N^+ + N^+$ channel is roughly 25 fs [39]. This is shorter than the duration of the two-color laser field used in our experiments. Thus, the initial tunnel ionization, molecular separation, and final ionization can all take place while the laser pulse is present. Accordingly, we are unable to resolve the specific dynamics involved. To determine if EI is occurring and which step in the process may be responsible for the directional emission of fragments observed in an asymmetric field, we can utilize two, ultrashort ($\sim$ 5 fs), time-delayed pulses, in a pump-probe experiment. Since the peak electric field in a $<$ 5 fs 750 nm laser pulse can be significantly larger in one direction relative to the other, such pulses enable the investigation of the origin of any field induced asymmetry, be it in the first or second ionization step or at some time in between.

In this chapter, we describe ultrashort pump-probe experiments on N_2 and O_2 performed

in collaboration with the group of Dr. Matthias Kling at the Max Planck Institute for Quantum Optics in Garching, Germany. Using the combination of Cold Target Recoil Ion Momentum Spectroscopy (COLTRIMS) and the stereo-ATI phase tagging technique, as described in Chapter 4, we have explored MEDI in N_2 and O_2 using two time-delayed < 5 fs pulses. Specifically, one < 5 fs pulse interacts with the neutral molecules and the influence of a second < 5 fs probe pulse on the yields in various dissociative ionization channels is recorded as a function of the pump-probe delay. We observe the $O_2(2,0)$, $O_2(2,1)$, $N_2(1,0)$, $N_2(1,1)$, $N_2(2,0)$, $N_2(2,1)$, and $N_2(2,2)$ dissociation channels from O_2 and N_2. (As in previous chapters, we use the notation "AB(p,q)" to refer to the AB $\rightarrow A^{+p}$+B^{+q} channel, whereas A^{+p} refers to the ions of charge p, non-specific to a particular dissociation channel.) We also observe time-dependent molecular dynamics in the $N_2(1,1)$, $N_2(2,0)$, and $N_2(2,1)$ channels. Regardless of species, dissociation channel, or pump-probe delay, and in spite of the strong field asymmetry in the few-cycle pulses, no directional fragment emission is observed.

5.2 Experimental Setup

The experiments described in this chapter were performed at the AS-1 beam line at the Max Planck Institute for Quantum Optics. The experimental setup, a combination of COLTRIMS and a stereo-ATI phase meter, has been described in detail in Chapter 4, and is illustrated in Figure 4.4. Briefly, nitrogen or oxygen gas enters the interaction region of the COLTRIMS chamber via a supersonic jet; spectrometer fields of 24-37 V/cm guide the ions towards the time-and-position sensitive detector. The laser pulses, which are < 5 fs in duration and have a central wavelength of 750 nm, are polarized along the spectrometer axis, and the intensity in the interaction region is controlled by an iris in the beam path. In

order to minimize the effects of the Gouy phase shift in the laser field as it moves through a focus, the laser beam is focused just before the gas jet. Carrier-envelope (CE) phase data is collected simultaneously with the stereo-ATI phase meter, as described in Section 4.2. To allow for two pulse pump-probe studies, the focusing mirror inside the COLTRIMS vacuum chamber has been cut into an outer annular and an inner circular region, and the inner mirror is mounted on a piezo stage to allow relative motion between the two mirrors. A function generator provides a triangle wave to drive the inner mirror forwards and backwards, constantly sweeping the pump-probe delay. A replica of the driving signal is fed into the ADC card to allow correlation of the pump-probe delay with the molecular dissociation and CE phase data. On-line monitoring and off-line analysis of the data are performed with the Go4 software suite.

5.3 Results

Figures 5.1 and 5.2 illustrate the time-of-flight spectra of the nitrogen and oxygen fragments, as collected with Go4. With the laser intensities used in these experiments ($\sim 10^{14}$ W/cm^2), ionization states up to N_2^{+4} and O_2^{+3} with neutral, singly- and doubly-charged ion fragments are produced. Polarization of the laser pulses along the spectrometer axis results in the characteristic forward and backward peaks for each species. The nitrogen fragments show clear dissociation channels, whereas the O^{+2} fragments have only small shoulders on the main peaks.

With the Go4 software, the time- and position- information is used to calculate the momentum of the ions at the time of dissociation. Here we define $p_{long} = p_z =$ momentum parallel to the spectrometer/laser polarization axis and

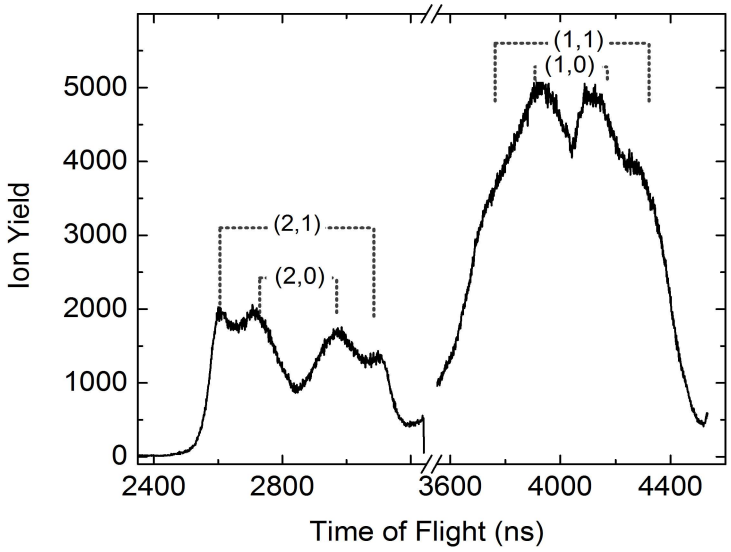

Figure 5.1: Time-of-flight spectrum of the N^+ and N^{+2} fragments from N_2.

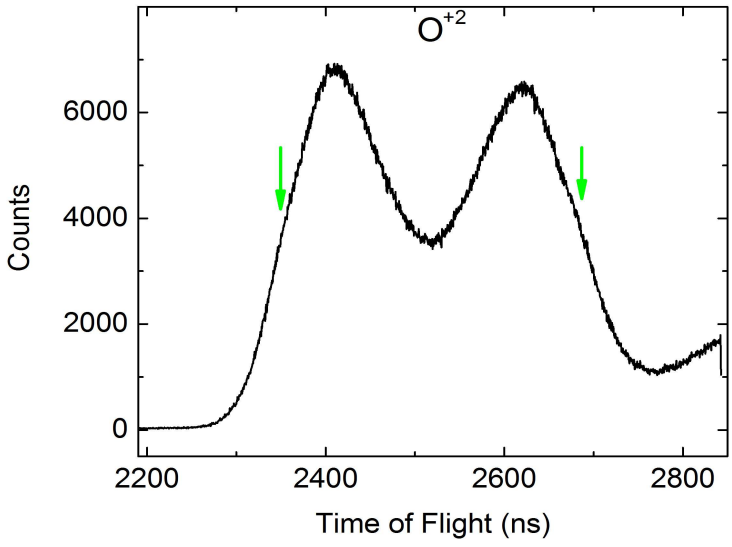

Figure 5.2: Time-of-flight spectrum for the O^{+2} fragments from O_2. The green arrows illustrate shoulders on the main peaks.

$$p_{trans} = \sqrt{p_x^2 + p_y^2} \tag{5.1}$$

is the momentum in the plane transverse to the polarization axis. By plotting the transverse vs. longitudinal momentum, as shown in Figures 5.3a and c for the N^+ and N^{+2} ions and Figure 5.4 for the O^+ ions, up to three dissociation channels for each ion species are visible.

In order to identify the dissociation channels, we can make use of coincidence filtering. The software records multiple ion hits per event, and can check for correlations between these hits. If, for example, the first hit and the second hit have equal and opposite momenta, they pass the coincidence filtering condition and are considered a pair having originated from the same molecular dissociation event. Using this method, we are able to identify the outer ring in Figure 5.3a as two distinct N_2(1,1) channels, illustrated in Figure 5.3b. Likewise, the predominant semi-circle in Figure 5.3c is the N_2(2,1) channel (Figure 5.3d), and a faint N_2(2,2) channel is also present (Figure 5.3e). Note that the filtering method returns some false coincidences, so the other channels may be visible in the filtered data in small amounts. Reducing the ion count rate would decrease the occurrence of false coincidences. The coincidence method can be used only if both ions from the dissociation event are collected. Since neutral fragments are not collected, the AB(1,0) and AB(2,0) channels cannot be identified in this manner. We do know that the lowest-momentum channels are not N_2(1,1) or N_2(2,1), and process of elimination allows them to be identified as N_2(1,0) and N_2(2,0) given that it is unlikely for weakly bound negative ions to survive the high laser intensities.

Balancing experimental conditions to obtain high charge states at a reasonable count rate without saturating the detector with low-charged fragments is a difficult task. This was not achieved in the case of the O_2 experiment; the O^+ fragments saturated the detector

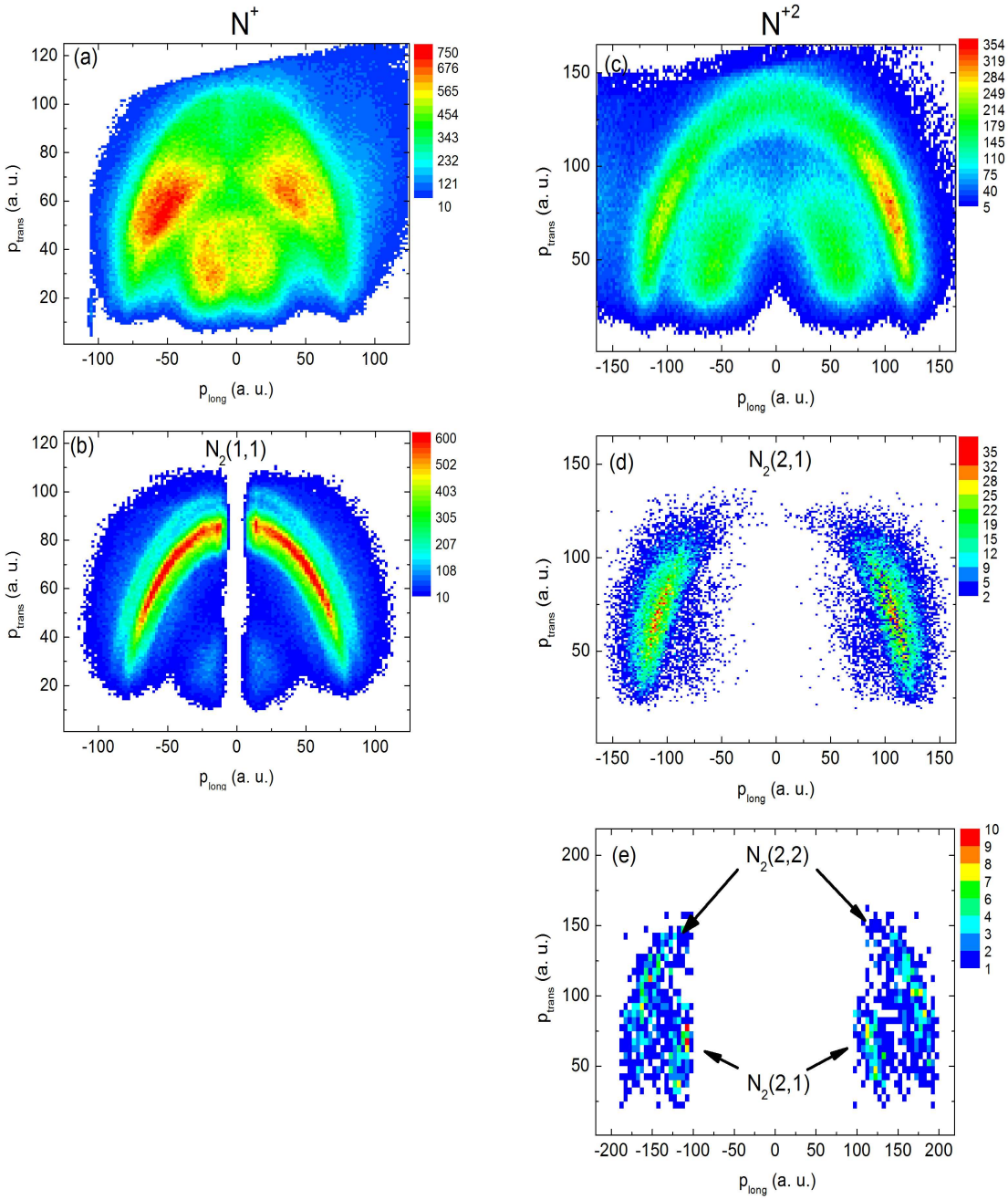

Figure 5.3: Transverse vs. longitudinal momentum for the N^+ and N^{+2} fragments. Panels (a) and (c) represent unfiltered data, and panels (b), (d), and (e) have been coincidence filtered for the specified channels.

and no meaningful coincidence-filtered data was obtained. However, based upon comparison with the N^{+2} fragments from the few-cycle pulse and O^{+2} fragments from the two-color experiments, we assign the lowest-momentum channel in Figure 5.4 to be the $O_2(2,0)$ channel and both of the higher-momentum curves to be $O_2(2,1)$ channels.

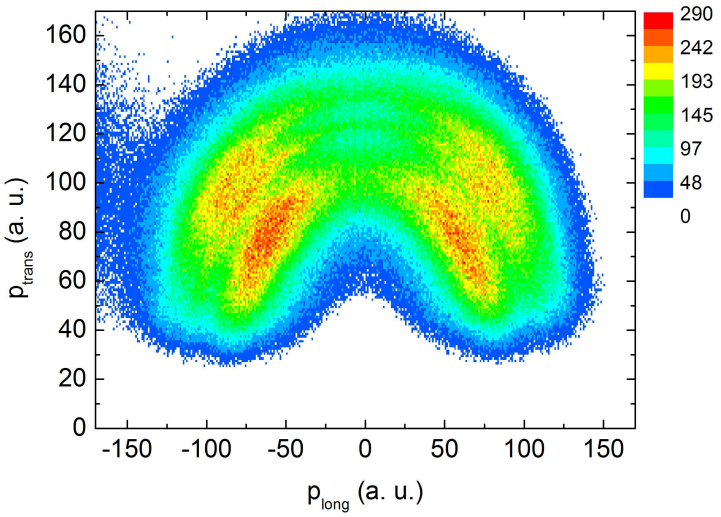

Figure 5.4: Transverse vs. longitudinal momentum for the O^{+2} fragments. No coincidence filtering has been performed.

Figure 5.5a-c shows the total momentum

$$p_{tot} = \sqrt{p_{trans}^2 + p_{long}^2} = \sqrt{p_x^2 + p_y^2 + p_z^2} \tag{5.2}$$

of the N^{+2} fragments as a function of pump-probe delay for three different laser intensities. In each case, the $N_2(2,0)$ and $N_2(2,1)$ channels are visible, but with different relative intensities. The yield in all channels increases significantly when the pump and probe pulses are temporally overlapped, i.e. $t = 0$. Also visible is a delay-dependent "swoop" between the $N_2(2,0)$ and $N_2(2,1)$ channels, the presence of which is strongest for the medium intensity

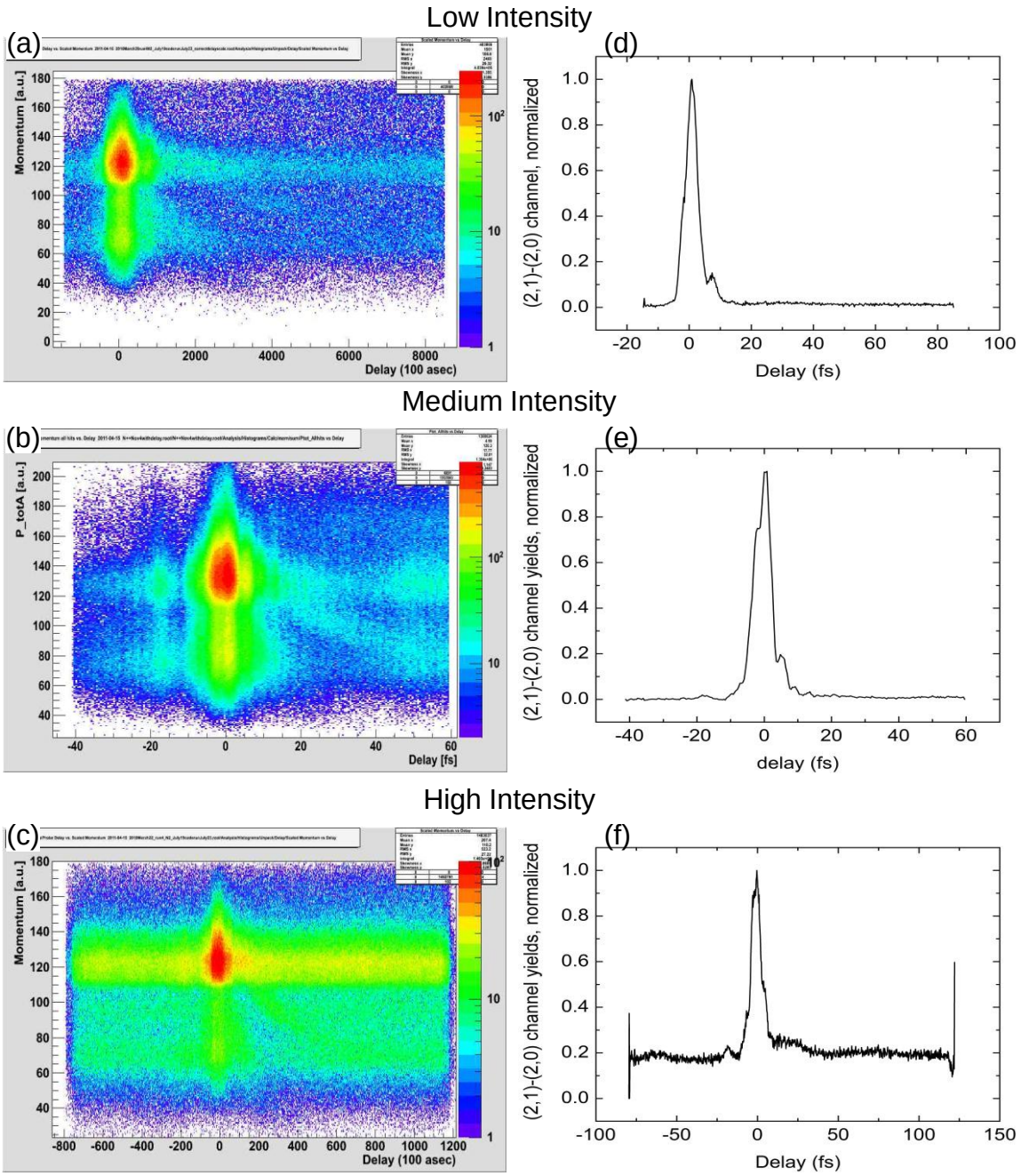

Figure 5.5: (a)-(c) Momentum vs. pump-probe delay for the N^{+2} fragments for three laser intensities. Note that the color intensity scales are on log scales. (d)-(f) The normalized difference between the $N_2(2,1)$ and $N_2(2,0)$ channel yields as a function of delay for the data in (a)-(c), respectively.

data, for which the $N_2(2,0)$ and $N_2(2,1)$ channels have approximately the same population. The delay dependence of the "swoop" indicates that ions detected in this channel are produced when molecules, dissociatively ionized by the first pulse, undergo subsequent ionization in the second pulse. The energy and delay-dependent intensity of this channel provides information about changes in the ionization rate as the molecular ion expands. Panels (d)-(f) in Figure 5.5 show the difference in the yield in the $N_2(2,1)$ and $N_2(2,0)$ channels for the data in panels (a)-(c), respectively. There may be some indication in panel (f) of the relative depletion of the $N_2(2,0)$ channel at delays between 15 and 40 fs.

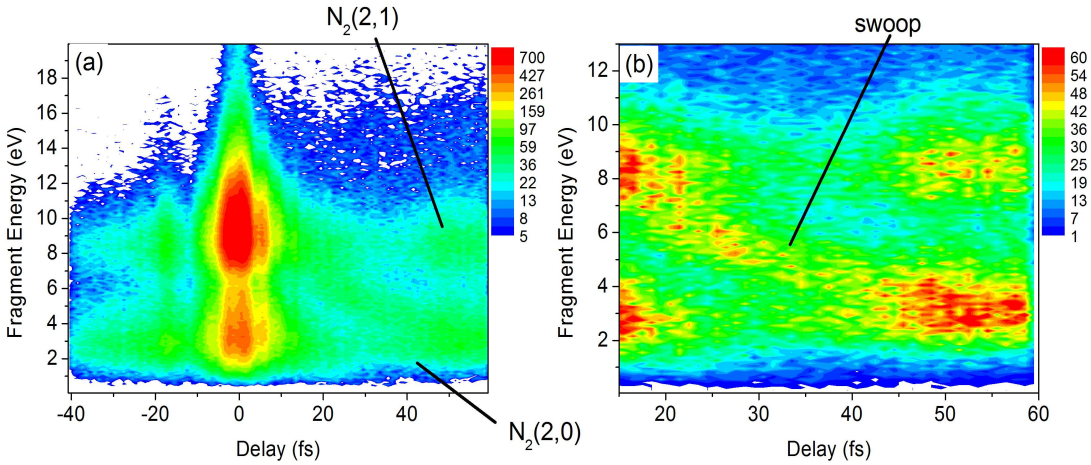

Figure 5.6: (a) N^{+2} fragment energy vs. pump-probe delay. (b) The same as (a) but with expanded scales to illustrate the swoop.

Analogous to Figure 5.5b, the delay-dependent fragment energy from the medium intensity experiment is reproduced in Figure 5.6, with scaling to highlight the swoop. This same data is represented in Figure 5.7, where we have plotted the transverse vs. longitudinal momentum for three delay windows: before, during, and after the swoop. The non-coincidence filtered data in panels (a)-(c) illustrates the emergence of an intermediate channel during the swoop, which disappears at long delays. By coincidence filtering, we confirm that the

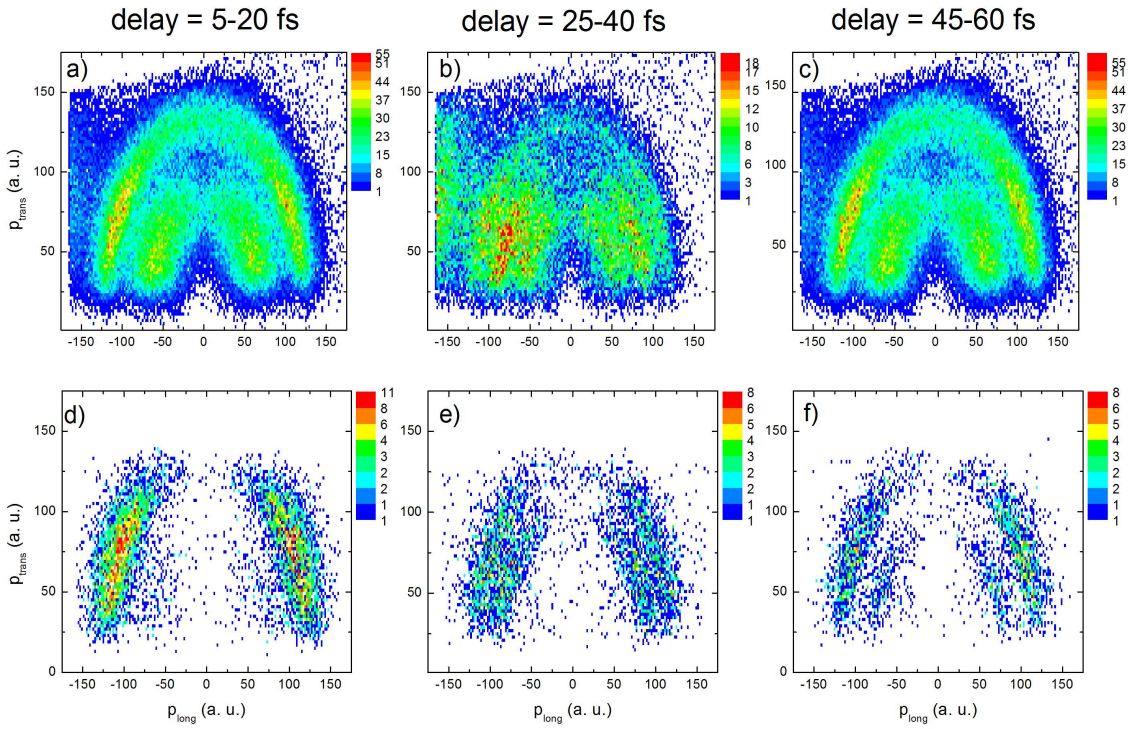

Figure 5.7: Transverse vs. longitudinal momentum of the N^{+2} fragments for three pump-probe delay regions. The data in panels (a)-(c) is unfiltered, whereas the data in panels (d)-(f) is coincidence filtered for the $N_2(2,1)$ channel.

swoop is due to a $N_2(2,1)$ channel, which has an asymptotic energy equal to that of the $N_2(2,0)$ channel at long delays (see Figure 5.7d-f). This assignment is reinforced by plotting the kinetic energy for the coincidence-filtered $N_2(2,1)$ channel as a function of delay. Figure 5.8 shows that the swoop contribution to the $N_2(2,1)$ signal is only significant for delays 10 fs $< t <$ 50 fs. Note that the channel kinetic energy release (KER) plotted in Figure 5.8 is the sum of the energy of the two ions created during the dissociation event, and is, therefore, equal to twice the energy of the individual ion fragments.

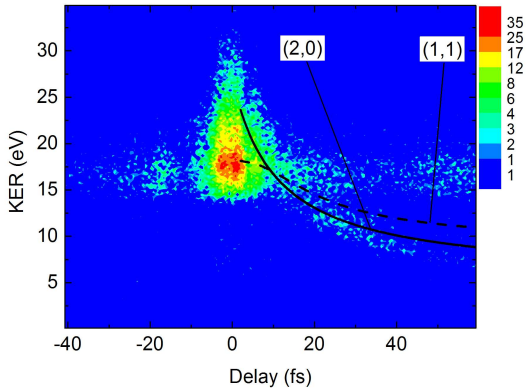

Figure 5.8: Similar to Figure 5.6(a) but plotted as channel kinetic energy release for the $N_2(2,1)$ coincidence-filtered data. The figure includes two model estimates, assuming the swoop originates from additional ionization of the $N_2(2,0)$ (solid line) and $N_2(1,1)$ (dashed line) channels. See Section 5.4 for further explanation of the models.

A similar phenomenon is observed in the N^+ fragments. While there is no apparent swoop in the unfiltered data (shown in Figure 5.9a), the $N_2(1,1)$ coincidence-filtered data shows a clear delay-dependent swoop between the main $N_2(1,1)$ and $N_2(1,0)$ channels. The appearance of this new channel is also visible (see Figure 5.10) in the p_{trans} vs. p_{long} plots for delay regions less than and greater than 45 fs.

In the case of the O^{+2} fragments, the momentum vs. delay plot, illustrated in Figure

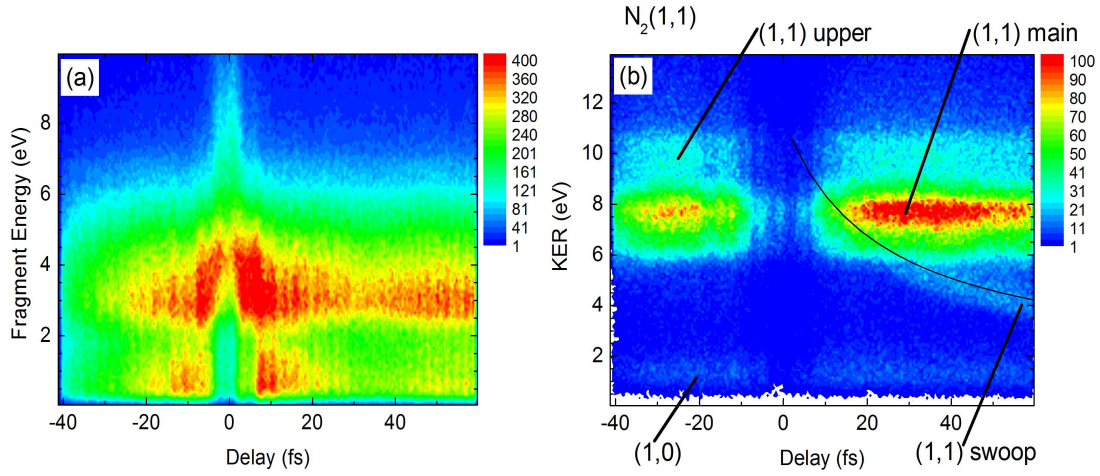

Figure 5.9: (a) N^+ fragment energy vs. pump-probe delay. (b) Channel kinetic energy release vs. delay for the $N_2(1,1)$ coincidence-filtered data. A theoretical KER vs. delay curve is overlaid in (b), for which initial dissociation along the $N_2(1,0)$ is assumed. See Section 5.4 for details on the model.

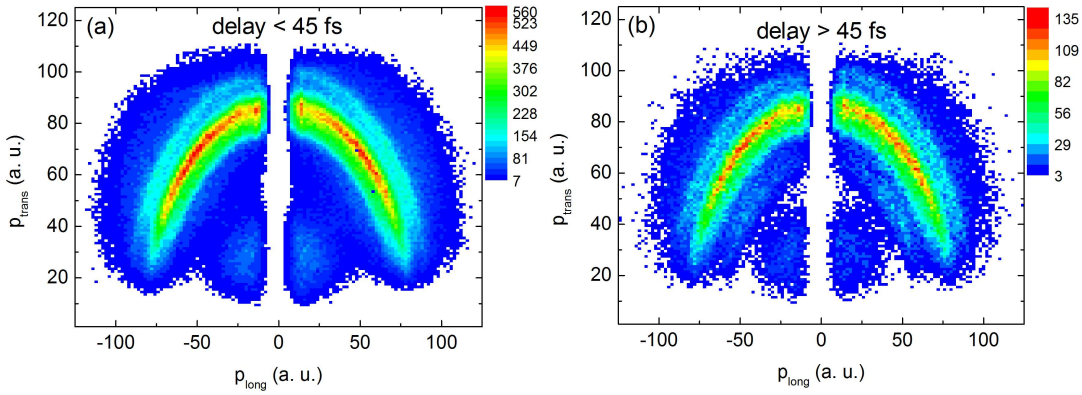

Figure 5.10: Transverse vs. longitudinal momentum of $N_2(1,1)$ coincidence-filtered data for two pump-probe delay regions.

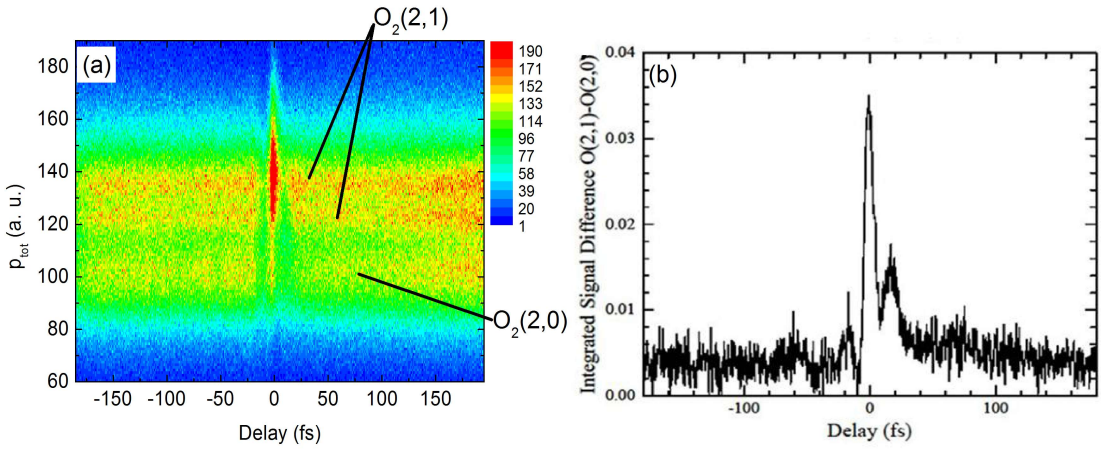

Figure 5.11: (a) Total momentum vs. pump-probe delay for the O^{+2} fragments produced in the dissociation of O_2. (b) The difference in the $O_2(2,1)$ and $O_2(2,0)$ channels as a function of delay.

5.11a, clearly shows that all three dissociation channels have constant momentum, regardless of delay. Plotting the difference in the $O_2(2,1)$ and $O_2(2,0)$ channels in Figure 5.11b reveals a large peak near 20 fs delay, which may indicate some population transfer. However, plotting p_{trans} vs. p_{long} (see Figure 5.12) shows that the momentum distributions remain the same, for all delay regions, which is consistent with the absence of a visible swoop in Figure 5.11a.

5.4 Discussion

From the Go4 analysis, we can extract the kinetic energy release (KER) associated with each dissociation channel by adding the energies of the two collected fragments. For the channels where only one fragment is collected, from momentum conservation the KER is twice the energy of the collected fragment. Table 5.1 compares the KERs from many N_2 and O_2 channels obtained using four different laser conditions: 40 fs 800 nm pulses, 40 fs

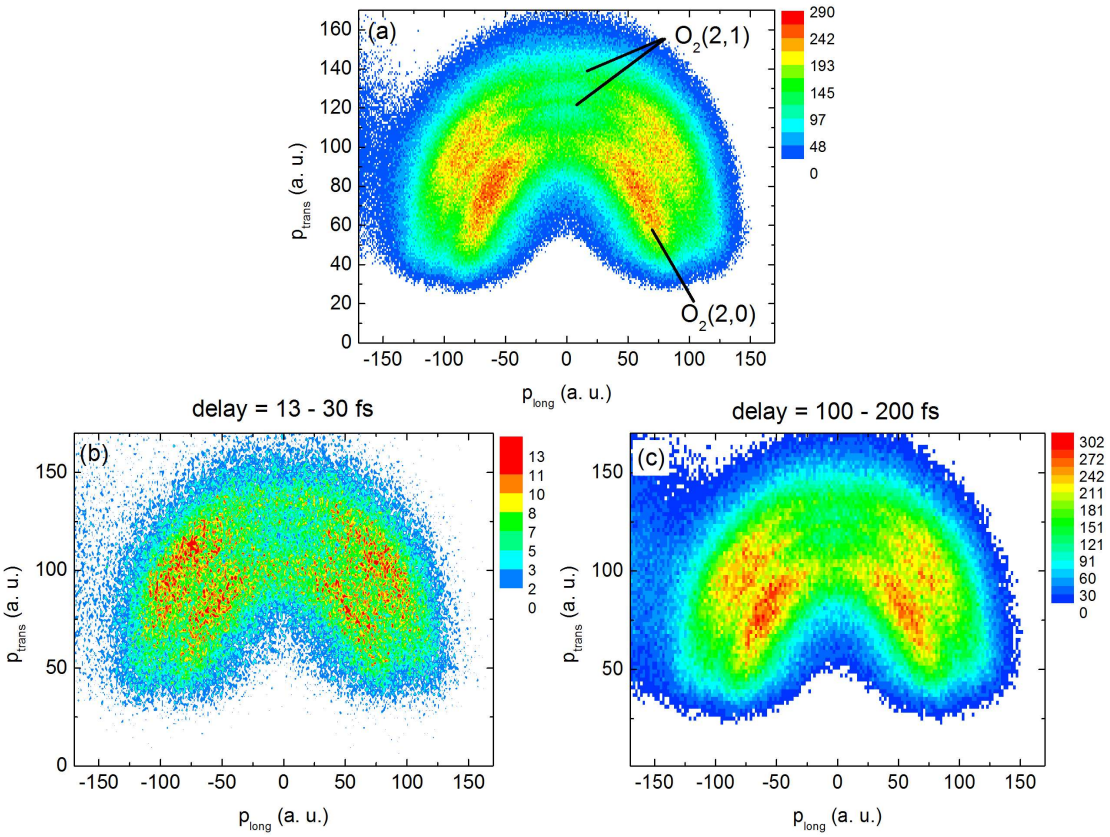

Figure 5.12: Transverse vs. longitudinal momentum of the O^{+2} fragments from the dissociation of O_2 for (a) all pump-probe delays, (b) delay = 13 - 30 fs, and (c) delay = 100 - 200 fs.

800 nm + 400 nm pulses, 5 fs 750 nm pulses, and 8 fs 800 nm pulses. The MPQ KER values were determined at long pump-probe delay, where the experiment is interpreted as a single 5 fs pulse interaction with the molecules. The results from a recent 8 fs single-color pump-probe experiment are also included. Listed values for that experiment were estimated from the asymptotic values of the KER vs. pump-probe delay plots [115] (see also [116]). An extended table, including the KERs for the long-pulse CO channels, is located in Appendix C. Our 5 fs single-color values are in good agreement with the results from the 8 fs pulse experiment, as indicated by the shaded regions of Table 5.1.

Generally speaking, the short pulse experiments result in larger KERs than the longer single- and two-color pulse experiments, particularly for the dissociation channels involving doubly- and higher-charged fragments. This is consistent with our expectation and previous measurements which show [117] that shorter laser pulses produce fragments with larger kinetic energies. Consider a dissociating molecule. Creation of each dissociation channel requires a particular laser intensity, which is governed by the rise time of the laser pulse. Shorter laser pulses result in higher intensities earlier in the pulse, allowing the nuclei less time to separate before the required laser intensity is available. Thus, a particular dissociation channel is created at smaller internuclear distance, leading to higher Coulomb explosion energies for short pulses than for longer pulses. Our observed KERs are slightly lower than those from 10 fs pulse experiments on N_2 [117], but this is believed to be due to the higher intensity ($5 \times 10^{14} - 7 \times 10^{15}$ W/cm^2) of the 10 fs pulses leading to Coulomb explosion approaching the equilibrium separation, $R_e = 2.074$ a.u. Assuming the observed kinetic energy is due to Coulomb explosion (a crude approximation for fragments with total charge $p + q < 3$), the internuclear separation, R, at the time of explosion can be estimated from

Table 5.1: Kinetic energy release (KER, eV) for the dissociation channels of N_2 and O_2. All single color data employed a near-IR Ti:Sapph laser, and the two-color experiment employed 400 nm + 800 nm pulses (see Chapter 3). The 8 fs data was estimated from KER vs. delay plots in [115].

Channel	40 fs Single Color UVA	Two Color UVA	5 fs Single Color MPQ	8 fs Single Color [115]
$N_2(1,0)$	1.32	0.8	1.5	2
$N_2(1,1)$	6.6	7		7.5-11
$N_2(1,1)$ main			7.6	
$N_2(1,1)$ upper			10.2	
$N_2(2,0)$	2	3.2	5.56	
$N_2(2,1)$	11	12		17-20
$N_2(2,1)$ main			16.6	
$N_2(2,1)$ upper			21.6	
$N_2(2,2)$	14.8			40-42
$N_2(2,2)$ lower			32.6	
$N_2(2,2)$ upper			39.6	
$N_2(3,1)$	17.8			
$N_2(3,2)$	25.8			
$O_2(1,0)$	1.2			2.7
$O_2(1,1)$	6.8			6-12
$O_2(2,0)$	1.9	2.1	8.9	
$O_2(2,1)$	10.6	9.3		13; 17-24
$O_2(2,1)$ lower			13.3	
$O_2(2,1)$ upper			16.4	
$O_2(3,1)$	17.3			20-35

Table 5.2: Internuclear separations (in atomic units, a.u.) at time of Coulomb explosion assuming Equation 5.3 for the KER values in Table 5.1.

Channel	40 fs Single Color UVA	Two Color UVA	5 fs Single Color MPQ
N_2(1,1)	4.1	3.9	
N_2(1,1) main			3.6
N_2(1,1) upper			2.7
N_2(2,1)	4.9	4.5	
N_2(2,1) main			3.3
N_2(2,1) upper			2.5
N_2(2,2)	7.4		
N_2(2,2) lower			3.3
N_2(2,2) upper			2.7
N_2(3,1)	4.6		
N_2(3,2)	6.3		
O_2(1,1)	4.0		
O_2(2,1)	5.1	5.8	
O_2(2,1) lower			4.1
O_2(2,1) upper			3.3
O_2(3,1)	4.7		

$$KER = \frac{pq}{R} \tag{5.3}$$

where p and q are the charges of the two fragments. For the 5 fs experiments, we find that Coulomb explosion is occurring at R = 2.5 - 3.5 a.u. for N_2. Table 5.2 lists the internuclear separations at the time of Coulomb explosion for the channels in Table 5.1. The internuclear separations indicate that our 5 fs pulse experiments exhibit slight molecular stretching, but not as much as in the longer pulse experiments. The higher KERs observed provide evidence that explosion due to expansion to R_c and enhanced ionization do not occur in a single 5 fs pulse.

The simultaneous depletion of the $N_2(2,0)$ yield and appearance of the $N_2(2,1)$ swoop, as viewed in Figure 5.6, suggests population transfer induced by the probe laser pulse from the $N_2(2,0)$ channel to the $N_2(2,1)$ channel, similar to that observed in the dissociation of molecular iodine [40]. If the probe pulse ionizes $N_2(2,0)$ to $N_2(2,1)$ at small R, the ion fragments experience a large additional Coulomb repulsion. The decrease in fragment energy as a function of delay is due to decreased Coulomb explosion energy as the molecule is dissociated at larger internuclear separations. At very long time delays, the ions are so far apart that Coulomb repulsion is minimal and the kinetic energy is primarily due to dissociation along the initial potential energy curve, thus the asymptotic KER is the same as that for the $N_2(2,0)$ channel. We now investigate several characteristics of this population transfer to test this hypothesis.

Looking at Figures 5.5b, c and 5.9b, one will notice that the so-called "swoops" occur only for positive pump-probe delays. This phenomenon is believed to be related to the relative intensities of the two pulses: It is necessary that the stronger pump pulse come first to drive population onto a specific $N_2(2,0)$ dissociation curve, from which the second

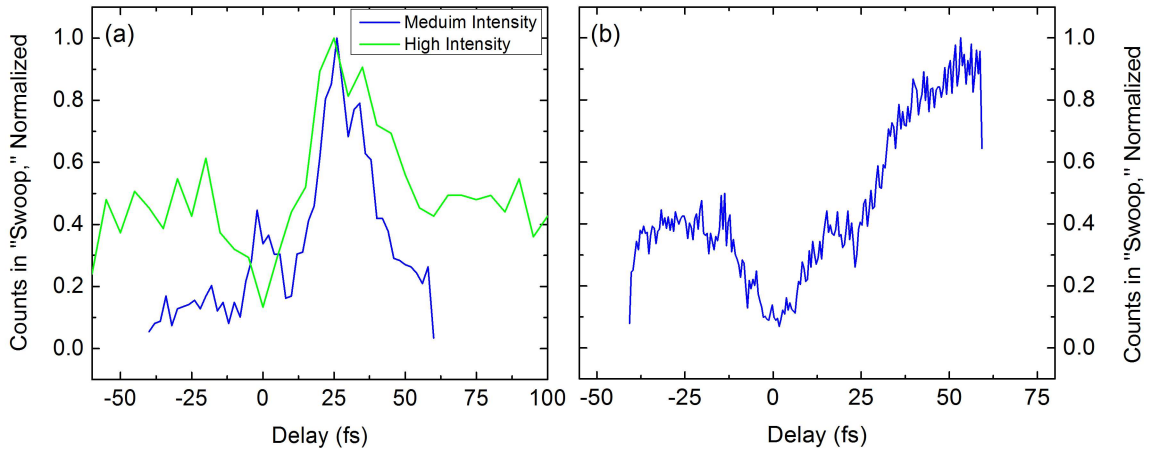

Figure 5.13: (a) Comparision of the $N_2(2,1)$ "swoop" timing for the medium and high intensity data in Figure 5.5 after coincidence filtering. (b) Similar to (a) but for the $N_2(1,1)$ swoop in Figure 5.9b.

weaker probe pulse can initiate dissociation via the $N_2(2,1)$ channel. If the weaker pulse interacts with the N_2 molecule first, it is not strong enough to populate the $N_2(2,0)$ channel, so, despite the second stronger pulse, the swoop is not visible.

To determine if the timing of the swoop is intensity dependent, we use coincidence filtering to extract the events in this channel and plot their yield as a function of pump-probe delay. Comparison of these yields for the medium and high-intensity experiments, as seen in Figure 5.13a, demonstrates that the maximum yield in the channel occurs at the same time regardless of laser intensity. A similar maximum occurring at ≈ 20 fs is observed in the normalized signal difference in between $O_2(2,0)$ and $O_2(2,1)$ (see Figure 5.12b). Interestingly, the enhanced ionization model suggests that a maximum in the ionization rate occurs when the dissociating molecule reaches a critical internuclear separation [38, 118, 119], which, for the N_2^{+2} molecular ion, occurs at ≈ 25 fs, according to Figure 5.13a.

While the simultaneous depletion of the $N_2(2,0)$ and production of the $N_2(2,1)$ swoop

channel with a weak probe pulse suggests that the swoop originates from an initial $N_2(2,0)$ dissociation, it could, in principle, come from the $N_2(1,1)$ channel. If, as suggested for I_2 [40], $N_2(1,1)$ is a precursor for $N_2(2,0)$ which forms via charge transfer at large to intermediate R, then the apparent depletion of the $N_2(2,0)$ could simply be a reflection of the depletion of $N_2(1,1)$. Also, the agreement between the measured and predicted delay, ≈ 25 fs, at which maximum transfer to $N_2(2,1)$ occurs suggest $N_2(1,1)$ is the parent of $N_2(2,1)$ as that prediction assumes R_c is reached via Coulomb expansion of $N_2(1,1)$. To identify the dynamical origin of the $N_2(2,1)$ "swoop," we develop two simple models for the $N_2(2,1)$ KER as a function of delay, assuming initial expansion in the $N_2(1,1)$ and $N_2(2,0)$ channels, respectively. For origination in the $N_2(1,1)$ channel, we assume a two-step Coulomb explosion sequence [39]. First, two electrons are ionized at the equilibrium internuclear distance, R_e, and the N_2^{+2} molecular ion explodes Coulombically as $N^+ + N^+$. The probe pulse arrives at a variable time, initiating an additional Coulomb explosion of $N^{+2} + N^+$ at internuclear separation R. The entire kinetic energy release is the sum of these two contributions

$$KER = q_1 q_2 \left(\frac{1}{R} - \frac{1}{R_e} \right) + \frac{pq}{R} \tag{5.4}$$

where $q_1 = q_2 = 1$ are the charges of the initial ions, and $p = 2$ and $q = 1$ are the charges of the observed ions. To convert this dissociation distance into time, we can integrate the equation of motion [39, 120]

$$t = \sqrt{\frac{\mu}{2}} \int_{R_e}^{R} \frac{dr}{\sqrt{E - U(r)}} \tag{5.5}$$

where $U(r) = \frac{q_1 q_2}{r}$ for dissociation along the initial Coulombic potential, $E = \frac{q_1 q_2}{R_e}$ is the energy at R_e, and μ is the reduced mass of the molecule. After integration and the

introduction of the variable $x = \sqrt{\frac{R}{R-R_e}}$, this yields [1]

$$t = \sqrt{\frac{\mu}{2}} \frac{R_3^{3/2}}{q_1 q_2} \left[\frac{x}{x^2-1} + \frac{1}{2} \ln\left(\frac{x+1}{x-1}\right) \right]. \tag{5.6}$$

Assuming the N_2^{+2} molecule begins dissociating from $R_e = 3$ a.u. at a delay of 2 fs (consistent with the internuclear separation results in Table 5.2), the resulting kinetic energy release as a function of pump-probe delay is overlaid as the dashed line in Figure 5.8.

Because the $N_2(2,0)$ channel is not Coulombic, we must use a different method for estimating KER as a function of delay. We assume instead that the $N_2(2,0)$ channel is excited on a very steep potential curve, and accelerates rapidly such that the dissociation occurs along a flat potential curve. This is not completely unreasonable considering the dominant interaction potential between the two fragments is due to the polarizability of the neutral atom which decreases as $1/R^4$. We assume that the final KER for the $N_2(2,1)$ channel is the sum of the energy from the $N_2(2,0)$ dissociation (from Table 5.1, KER$[N_2(2,0)]$ = KER$'$ = 5.5 eV) and Coulomb explosion into $N_2(2,1)$ at a variable internuclear separation

$$\begin{aligned} KER &= KER[N_2(2,0)] + \frac{pq}{R} \\ &= KER' + \frac{pq}{R} \\ &= 5.5\text{eV} + \frac{pq}{R} \end{aligned} \tag{5.7}$$

where, again, $p = 2$ and $q = 1$. We also use the asymptotic $N_2(2,0)$ energy as a measure of the velocity of the dissociation,

[1] The solution to this integral in [39], Eqn. 15, is incorrect. It should read "t=... + 0.5ln()...".

$$KER' = \frac{1}{2}\mu v^2, \tag{5.8}$$

to find R as a function of delay

$$t = \frac{\Delta R}{v} = \frac{R - R_e}{\sqrt{\frac{2KER'}{\mu}}} + t_0. \tag{5.9}$$

Assuming R_e=3 a.u. and t_0 = 2 fs, the KER vs. pump-probe delay curve is plotted as a solid line in Figure 5.8.

From comparison of these two model curves with the experimentally observed kinetic energy release, it is apparent that the $N_2(1,1)$ model curve is not the proper representation. The $N_2(2,0)$ model curve, however, is in reasonable agreement with the experimental data given the crudeness of the model. This suggests that the $N_2(2,1)$ channel originates from the $N_2(2,0)$ channel. Moreover, the dissimilarity of the $N_2(2,0)$ and $N_2(1,1)$ curves indicates that the former channel is created independently from the $N_2(1,1)$ channel. Interestingly, for a molecular wavepacket launched in the primitive $N_2(2,0)$ curve, the maximum in $N_2(2,1)$ yield at t $\approx$ 25 fs occurs at R $\approx$ 8.3 a.u, which is in fair agreement with the predicted value [39] of R_c=7.6 a.u. for N_2. A similar crude analysis for the delay-dependent $I_2(2,1)$ channel observed in previous pump-probe experiments [40] indicates that initial expansion along the $I_2(2,0)$ curve would result in an internuclear separation of 11.4 a.u. when the maximum channel yield is observed, which is, again, slightly larger but in fair agreement with the predicted value of R_c = 10 a.u. Thus, the I_2 experiment may also have been observing initial electron localization to the $I_2(2,0)$ state followed by ionization of the neutral atom.

Presumably, the $N_2(1,1)$ swoop originates from the $N_2(1,0)$ channel, as it is the only channel of the next lowest degree of ionization. To test this, we estimate a KER vs. delay

curve for the $N_2(1,1)$ channel in the same way as for the $N_2(2,1)$ channel originating from $N_2(2,0)$. We assume initial propagation on flat the $N_2(1,0)$ curve, with initial KER = 1.5 eV, from R_e=3 a.u. started at a delay of 2 fs. The final $N_2(1,1)$ KER is given by Equation 5.7 with $p = q = 1$ and $\mathrm{KER}' = 1.5$ eV. This curve fits remarkably well to the experimental data in Figure 5.9b, and suggests that the $N_2(1,1)$ channel originated as $N_2(1,0)$. The swoop channel yield as a function of delay, plotted in Figure 5.13b does not show a discrete maximum, suggesting that $N_2(1,1)$ is formed from ionization of the neutral fragment in $N_2(1,0)$ following charge localization at $\approx$ 20 fs.

Previous two-color [14–20, 113] and few-cycle pulse [6, 9] experiments have illustrated the directional emission of fragments during molecular dissociations in asymmetric fields. Based upon this knowledge, we analyze the current few-cycle pulse data looking for such directional emission. First, we select a specific dissociation channel and pump-probe delay region. From these data, we calculate the energy-, delay-, and phase-dependent asymmetry parameter, $\beta(E, delay, \phi)$

$$\beta(E, delay, \phi) = \frac{Y_f(E, delay, \phi) - Y_b(E, delay, \phi)}{Y_f(E, delay, \phi) + Y_b(E, delay, \phi)} \tag{5.10}$$

as in previous chapters. We find that, for all dissociation channels and all delay regions, no statistically significant asymmetry is observed for N_2 or O_2. Figure 5.14 illustrates the lack of asymmetry for the $N_2(2,1)$ swoop for pump-probe delay 25 - 60 fs.

Our two-color experiments exhibit a high degree of asymmetry for all dissociation channels studied, and it may be expected that the few-cycle pump-probe work would return similar results *if* the pulse asymmetry was critical at one or two well-defined times, e.g. initial ionization and ionization at R_c. One possibility of the lack of asymmetry in the few-cycle pulse data could be that many of the on-axis fragments are being lost due to

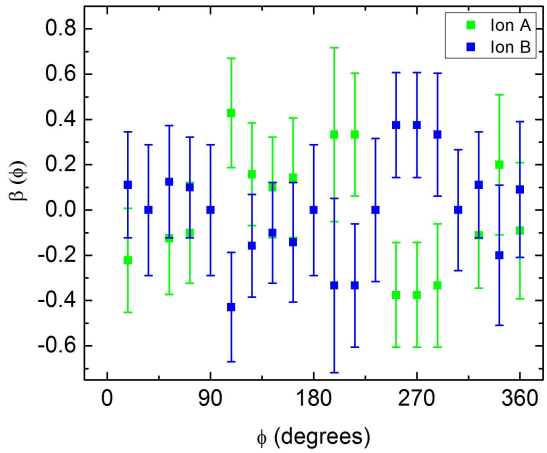

Figure 5.14: The asymmetry parameter for the $N_2(2,1)$ swoop for pump-probe delay 25-60 fs.

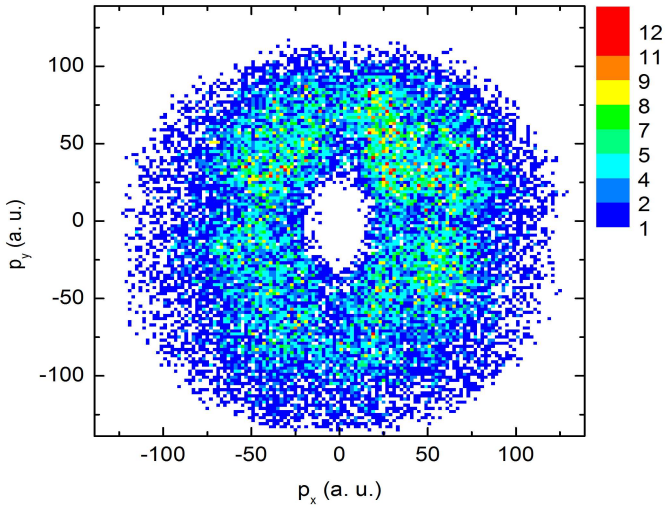

Figure 5.15: The apparent momentum of N^{+2} ions in the plane of the detector. the non-isotropic distribution indicates a significant "dead" region at the center of the MCP detector. It is known that these dead regions can be formed by large ion flux incident on the detector for extended periods of time.

a rather large dead region on the microchannel plates in the MPQ detector. This dead region is illustrated in Figure 5.15, which plots the N^{+2} fragments' momenta in the plane of the detector. This distribution should be isotropic in the plane perpendicular to the laser polarization. This may contribute to the observation that the angular distributions of the fragments produced with the ultrashort pulses have much larger off-axis yields than those from the longer pulse, two-color field experiments. (Another possibility is that the fragments are formed via different processes in the two experiments, as the different KERs also suggest.) For example, compare Figures 5.16a and 5.3c for the N^{+2} fragments created in the two-color and few-cycle pulse experiments. To give a quantitative comparison of the angular distributions, we define the polar angle γ

$$\gamma = \frac{p_{trans}}{p_{long}} \tag{5.11}$$

and extract the 1-dimensional angular distributions, as demonstrated in Figure 5.16 for the $N_2(2,0)$ and $N_2(2,1)$ channels from the two-color field experiments. Rather than explicitly show these angular distributions for every dissociation channel, we calculate the peak and width of each distribution, and display them in Figure 5.17. The few-cycle pulse experiments from MPQ always result in angular distributions peaked farther away from the laser polarization axis, although the widths of these distributions are about the same as those from the UVA single- and two-color experiments.

In order to determine if the majority of the two-color asymmetry is due to the on-axis fragments, we filter the UVA two-color data so only those events with large momenta in the transverse directions are included, i.e. we cut a hole in the middle of the detector to match that in the MPQ data. The amplitude of the asymmetry parameter calculated including only the off-axis fragments is found to be equal to that from the entire distribution, and is

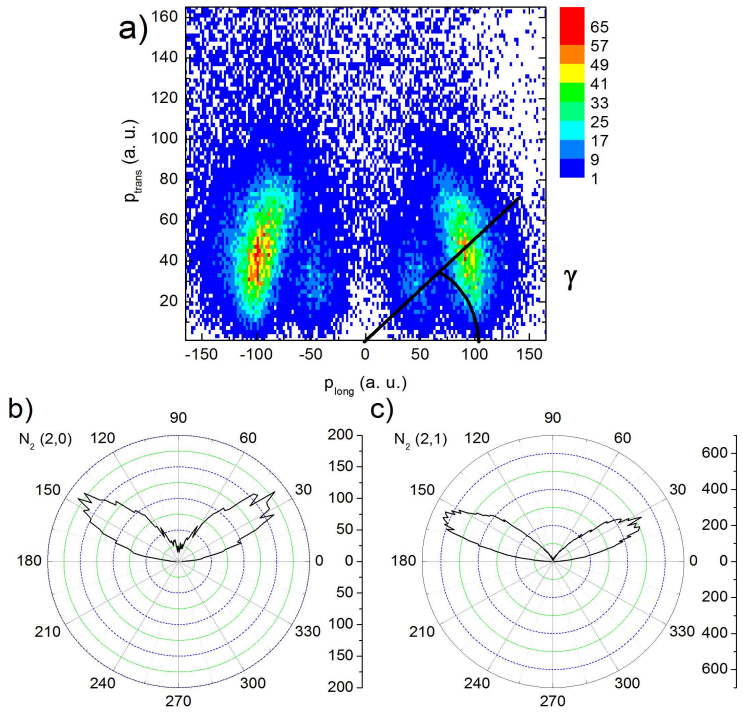

Figure 5.16: (a) Definition of the angle γ illustrated for the N^{+2} fragments from the two-color field data. The angular distributions for N^{+2} fragments from the (b) $N_2(2,0)$ and (c) $N_2(2,1)$ channels from the two-color experiments at UVA. The laser polarization is along the horizontal p_{long} axis.

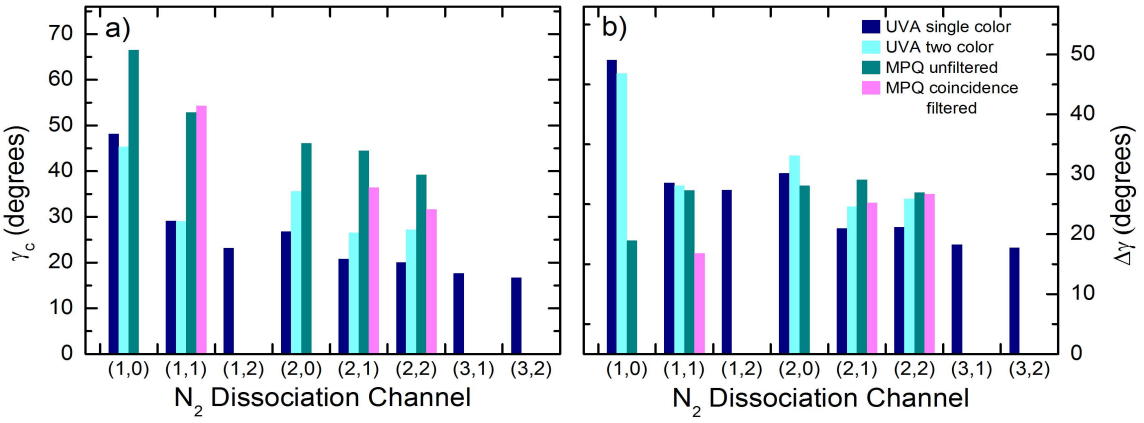

Figure 5.17: Comparison of the (a) centers, γ_c, and (b) widths, $\Delta\gamma$, of the angular distributions of the ion fragments for several N_2 dissociation channels. The UVA single color data was taken using 40 fs 800 nm laser pulses, and the UVA two-color data was taken using the 400 nm + 800 nm pulses described in Chapter 3. The MPQ data employed 5 fs 750 nm pulses, and it was coincidence filtered when possible.

shown in Figure 3.14. Therefore, it is believed that the loss of the on-axis fragments is not obscuring any potential asymmetry in the few-cycle pulse experiment.

Assuming that detector is not obscuring any asymmetry that may be present, the lack of observed asymmetry suggests that, unlike in the two-color experiment, the few-cycle pulses do not induce asymmetric dissociation in the present channels. Rather, it indicates that the light needs to be present throughout the dissociation process. This suggests that the asymmetric dissociation observed in the two-color experiment is the result of an ongoing coupling of states as the molecule is expanding. One specific stage in the process, such as the first ionization step, charge localization in an asymmetric channel, or enhanced ionization at R_c, does not seem to determine the electron localization.

5.5 Conclusion

In summary, we have measured the kinetic energy releases of several N_2 and O_2 dissociation channels induced by few-cycle laser pulses. These values illustrate Coulomb explosion close to the equilibrium internuclear distance. Distinct changes in KER as a function of delay indicates ionization of $N_2(2,0)$ to $N_2(2,1)$ via ionization of the neutral following charge localization in $N_2(2,0)$. Why this ionization apparently shuts off at longer times is not understood at this time, but may be the result of charge exchange between $N_2(2,0)$ and $N_2(1,1)$ channels via tunneling at large R. The lack of directional emission of fragments in the few-cycle field indicates that the asymmetry observed in the two-color field experiments is the result of the long laser pulse continuously coupling states during the dissociation event.

Chapter 6

Summary and Conclusions

Using laser fields to probe or control the combined electronic and nuclear dynamics in intense-field processes such as atomic and molecular ionization, nonsequential double ionization, high harmonic and attosecond pulse generation, and molecular dissociations has been the subject of much research over the past two decades. The use of asymmetric laser fields extends these areas of research to exploration and potential exploitation of the inherent asymmetries present in these processes. In this dissertation, we describe three experiments which employ asymmetric laser fields to induce and explore the dynamics of multielectron dissociative ionization (MEDI) of N_2, O_2, CO and CO_2 and nonsequential double ionization of Ar.

Chapter 3 details experiments in which we use a two-color laser field to explore the directional fragment emission from dissociative ionization of N_2, O_2, CO and CO_2. By changing the relative phase between the red and blue components of the two-color field, we observe large, robust asymmetries in the directionality of fragment emission for all species studied. All dissociation channels observed exhibit the largest asymmetry when the two-color field is also maximally asymmetric. If we adopt an independent phase calibration

[16, 21], we find that the fragments with the highest ionization potential are preferentially emitted in the direction opposite to the field maximum, which is precisely opposite to predictions based on the standard model of enhanced ionization (EI) [90, 91]. Recent private communications [93, 94] indicate that a phase discrepancy of π in this independent phase calibration may have been found, indicating that the phase of our observed asymmetry may be in agreement with the EI model.

The molecular dissociations studied in Chapter 3 take place on a timescale of $\sim$ 25 fs. Thus, our 40 fs laser pulses do not allow the resolution of the nuclear dynamics occurring during the MEDI event. In Chapter 5, we discuss a pump-probe experiment using two time-delayed sub-5 fs pulses to time-resolve the dissociation dynamics of N_2 and O_2. These pump-probe experiments suggest that the delay-dependent $N_2(2,1)$ channel is created through charge localization into the asymmetric $N_2(2,0)$ state after interaction with the strong pump pulse followed by ionization of the neutral atom by the weak probe pulse. A similar mechanism of electron localization to the $N_2(1,0)$ channel and subsequent ionization of the neutral fragment is observed in the delay-dependent production of the $N_2(1,1)$ channel.

To date, experiments exploring the effects of the carrier-envelope phase of few-cycle pulses on atomic and molecular processes have required extensive efforts to stabilize the carrier-envelope (CE) phase. In Chapter 4, we describe the first experiments to use a novel method of measuring the CE phase of each laser pulse and recording it simultaneously with information from a second laser-induced event. The first demonstration of this combination of stereo-ATI phase measurement and cold target recoil ion momentum spectroscopy (COLTRIMS), referred to as "phase tagging," studies the CE phase dependence of nonsequential double ionization of argon. The results not only illustrate a robust phase

dependence, but the method increases the possible data acquisition time to several days, greatly improving statistics while requiring only a fraction of the effort necessary for phase stabilization.

Using this phase tagging technique, we use the few-cycle pulse pump-probe geometry to investigate whether the laser phase at one stage in the dissociation process, such as tunnel ionization at R_e or R_c, determines the phase of the observed fragment directionality in the two-color field experiments. This is described in Chapter 5. Regardless of ionization channel or pump-probe delay, and despite the inherent asymmetry in the few-cycle pulse, we observe no directional fragment emission from N_2 or O_2. This indicates that one stage in the enhanced ionization process does not determine the electron localization, and suggests that a continual coupling of states via an ever-present laser field as the molecule expands is necessary for directional fragment emission.

Considering the lack of asymmetric dissociation induced by few-cycle (< 5 fs) pulses but its robustness when induced by longer, two-color (~ 40 fs) pulses, one logical question to ask is, "How long do the pulses need to be?" It may be instructive to study the same diatomic molecules with a ~ 10 fs two-color field, which retains its asymmetric quality due to the two frequencies present but may not obscure all of the ensuing dynamics. Experimentally, the creation of such laser pulses is non-trivial. It will require, after pulse compression in a hollow-core fiber/chirped mirror setup, frequency doubling in a very thin non-linear crystal located inside the vacuum chamber to avoid temporal walk-off between components due to the vacuum chamber window. Preliminary attempts to create such pulses have been made, but the conversion efficiency of the 10 μm crystal was prohibitively low, such that there was not enough blue light to create a two-color pulse with the necessary field asymmetry. An alternative suggestion to further the study of asymmetric molecular dynamics would

be to use a 10 fs pulse in conjunction with a $\sim$ 100 fs two-color field, which will require synchronization of multiple lasers, but should be possible.

Preliminary analysis of more few-cycle pulse experiments indicates the presence of asymmetric dissociation in some dissociation channels from the heteronuclear diatomics CO and NO. Further analysis may shed light on the origins of electron localization and preferential emission of fragments produced by multielectron dissociative ionization in asymmetric laser fields.

Since the first proof-of-principle experiments described in Chapter 4, the phase tagging technique has been expanded to also collect electrons created in the nonsequential double ionization processes. This full reaction microscope technique has been applied to NSDI in argon, neon, N_2, O_2, and CO. Combined analysis of the electrons and ions will help to resolve the on-going discussion of the mechanisms behind NSDI [3, 103, 109–111].

Appendix A

Frequency Comb Theory and the Creation of Carrier-Envelope Phase-Locked Oscillator Pulses

A.1 Introduction

First steps have been made to upgrade the amplified 30 fs laser system in the Chemistry lab to be able to produce phase locked few-cycle laser pulses. At the time of this writing, it is possible to produce phase locked laser pulses from the oscillator via the FC 8004 Optical Frequency Synthesizer from MenloSystems, GmbH [46], and this process is outlined here.

A.2 Theory of Frequency Combs and CE Phase-Locking

Consider the ideal case of a pulse circulating inside a laser cavity of length L with carrier frequency ω_c. In the time domain, this results in the output from the laser being a sequence of nearly identical pulses separated by the cavity round-trip time, $T = 2L/v_g$, where v_g is the

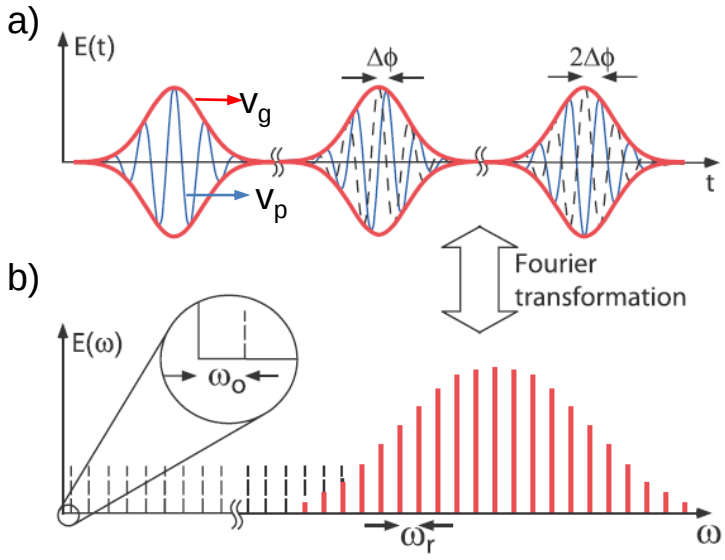

Figure A.1: Representation of a mode-locked laser pulse in the (a) time- and (b) frequency domains. Figure taken from [121].

mean group velocity of the pulse inside the cavity. However, due to dispersive elements in the cavity, the carrier wave does not propagate with the same velocity as the pulse envelope, i.e. $v_g \neq v_p$, where v_p is the phase velocity. This inequality leads to a carrier-envelope (CE) phase shift, $\Delta\phi$, per round trip in the cavity, as illustrated in Figure A.1a.

If we now consider the same situation in the frequency domain (see Figure A.1b), we see that the pulse spectrum is a comb of laser modes, equally spaced by frequency ω_r ($\omega_r = 2\pi$ f_r, where f_r is the pulse repetion frequency) and centered at ω_c. The continuous CE phase shift manifests itself in an offset, $\omega_0 = \Delta\phi T$, of the first comb mode from 0. This means that the comb modes are not quite exact harmonics of the repetition frequency. Instead, $\omega_n = n\omega_r + \omega_0$, where n is the (very large, n $\approx 10^6$) mode number.

The comb spacing, ω_r, is straight forward to measure with a fast photodiode, but determination of ω_0 requires an interferometric measurement. In the Chemistry lab, the

frequency comb has a bandwidth greater than an optical octave, so the two interfering beams are both derived from different regions of the same spectrum, and a "self-referencing" method is used.

Consider measuring the combination of two beams of light with electric fields $E_1(t) = E_1 e^{i\omega_1 t}$ and $E_2(t) = E_2 e^{i(\omega_2 t + \phi_0)}$ on a photodetector. Due to its heterodyne detection characteristics, the photodetector's response would be proportional to the total intensity of the light,

$$I \propto E_1^2 + E_2^2 + 2E_1 E_2 \cos\left((\omega_2 - \omega_1)t + \phi_0\right) \tag{A.1}$$

where E_1 and E_2 are the magnitudes of the two electric fields, ω_1 and ω_2 are their angular frequencies, and ϕ_0 is the variable phase shift between them. This heterodyne detection method, in which two signals are non-linearly mixed to create a signal at the difference frequency, maintains the amplitude, phase, and frequency modulation information present in the initial signals. For example, if the optical phase of the second beam shifts by and amount $\delta\phi$, the optical phase in the difference beam shifts by exactly the same amount. Clearly, the phase difference between the two laser beams,

$$\phi_2(t) - \phi_1(t) = (\omega_2 - \omega_1)t + \phi_0, \tag{A.2}$$

is the quantity of interest here.

If we were to directly compare light from the long- and short- wavelength regions of the frequency comb, for example one beam being the second harmonic of the other ($\omega_2 = 2\omega_1$), Equation A.1 would become

$$I \propto E_1^2 + E_2^2 + 2E_1 E_2 \cos\left((\omega_1)t + \phi_0\right). \tag{A.3}$$

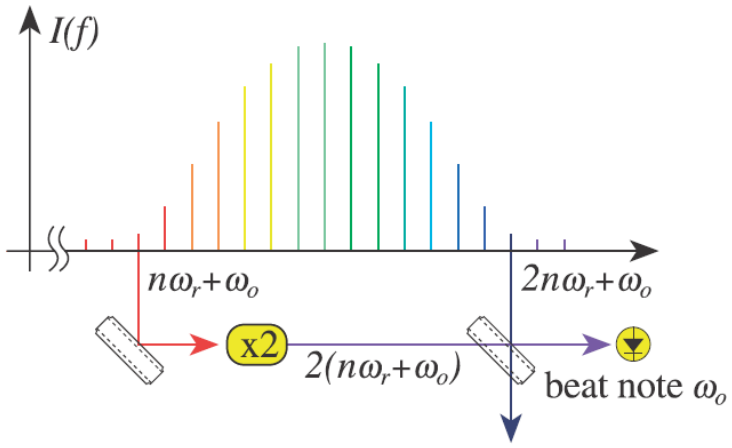

Figure A.2: In one arm of an interferometer, light from the long wavelength side of the spectrum is frequency doubled in a non-linear crystal and then combined with the modes from the short wavelength side. Heterodyne mixing of individual mode pairs creates a beat signal, which is used for the measurement of ω_0. Figure taken from [121].

In this case, the beats in the combined field occur at optical frequencies, whose detection is far beyond the capabilities of electronic circuits. However, if the frequencies of the two beams are much closer to one another, for example, by frequency-doubling the long-wavelength side of the spectrum so $2 \times \omega_1 \approx \omega_2$, as illustrated in Figure A.2, the oscillations now occur at much lower radio frequencies, which are easier to process.

To illustrate how this interferometric technique creates useable signals, we return to frequency space. Consider a comb mode of number n on the long wavelength (i.e. red) side of the spectrum

$$\omega_n = n\omega_r + \omega_0 \tag{A.4}$$

and a comb mode on the short wavelength (i.e. blue) side of the spectrum with mode

number $2n$

$$\omega_{2n} = 2n\omega_r + \omega_0 \tag{A.5}$$

If the red mode is frequency doubled and then mixed with the blue mode via heterodye detection, per Figure A.2,

$$2\omega_n - \omega_{2n} = 2(n\omega_r + \omega_0) - (2n\omega_r + \omega_0) = \omega_0 \tag{A.6}$$

Alternatively, if we redefine $\omega_1 \equiv \omega_{2n}$ and $\omega_2 \equiv 2\omega_n$ and substitute Equation A.6 into Equation A.2

$$\phi_2(t) - \phi_1(t) = (\omega_2 - \omega_1)t + \phi_0 = (2\omega_n - \omega_{2n})t + \phi_0 = \omega_0 t + \phi_0 \tag{A.7}$$

it becomes obvious that the phase difference between the two beams can be used to determine ω_0.

In reality, many comb modes are present in the direct and frequency doubled green beams, and beat signals between many pairs of modes are created. The resulting signal, as detected by the photodiode, is a series of peaks, spaced $\pm\omega_0$ away from $\omega = 0$ and integer multiples of ω_r. Mixing between modes n and $2n + x$, where $x = 0, 1, 2, ...$, creates the peak spacing at ω_r, whereas the $-\omega_0$ shift results from mixing the two modes with the sign opposite above, i.e. $\omega_{2n} - 2\omega_n$. Selection of one specific beatnote for analysis is done by radio-frequency filters in the locking electronics.

The very important result is that stabilizing ω_0 will stabilize the round-trip carrier-envelope phase shift, $\Delta\phi$. The optical and electronic components used to stabilize ω_0 are described below. At this time in the Chemistry lab, stabilization of ω_r is available, but is

not required for stabilization of ω_0.

A.3 Nonlinear f-to-2f Interferometer

As mentioned in Section 2.2.3, 30% of the light from the Femtosource oscillator is split off from the main beam and is used for phase-locking. Obtaining carrier-envelope phase-locked pulses requires using an optical "beatnote" signal as an input to a system of electronics that monitors the CE phase and generates the signal for feedback into the optical system. A nonlinear f-to-2f interferometer generates this optical signal, and is illustrated in Figure A.3. A photonic crystal fiber is used to broaden the spectrum of the light from the oscillator to more than an optical octave, and the components near 532 nm and 1064 nm are picked off and sent into the f-to-2f interferometer. The green component is separated from the IR component by a dichroic beam splitter, thus creating the two legs of the interferometer. After the IR component is frequency doubled in a 5 mm $KNbO_3$ crystal, the two green beams are recombined and dispersed by a grating, and the frequency offset ("beatnote") between the two green beams is detected by an avalanche photodiode. Half waveplates in both legs of the interferometer allow for the adjustment of the polarization directions of the two beams, and a pair of BK 7 prisms in the 532 nm arm serves as a delay line in order that the pulses from the two arms are temporally overlapped. The light between 600 nm and 900 nm that is not passed into the nonlinear interferometer is incident on a photodiode, via which it provides a reference signal for the local oscillator (see Section A.4.1).

A.3.1 Photonic Crystal Fiber

Developments in photonic crystals, materials that incorporate a periodic modulation of the refractive index on the physical scale of an optical wavelength, have led to a family of air-

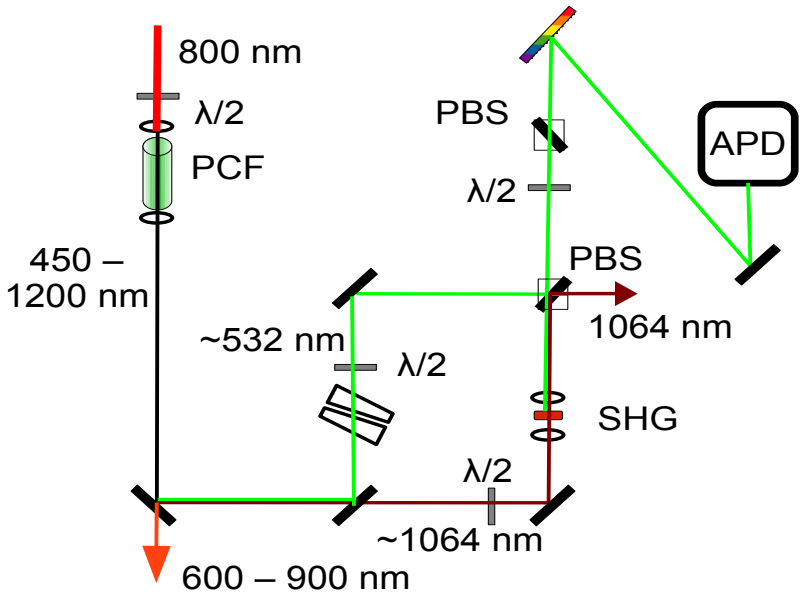

Figure A.3: Schematic of the nonlinear interferometer employed for beatnote detection. PCF: photonic crystal fiber; $\lambda/2$: half waveplate; SHG: second-harmonic crystal; PBS: polarizing beamsplitter; APD: avalanche photodiode.

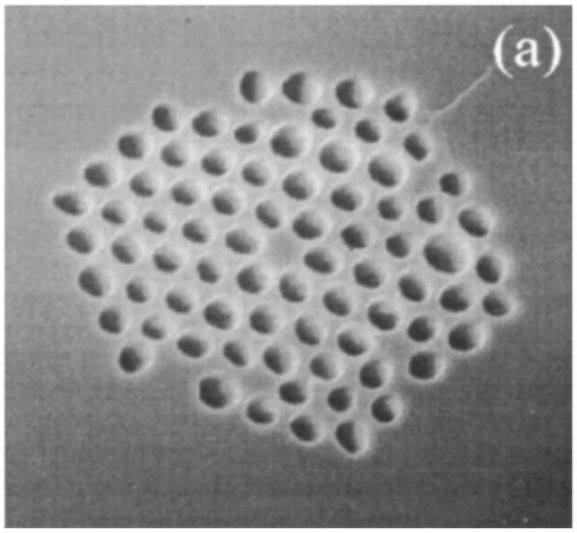

Figure A.4: Electron micrograph image of an air-silica microstructure fiber [124].

silica microstructure fibers [122–125]. These fibers, illustrated in Figure A.4, are composed of a solid silica core approximately 2 μm in diameter surrounded by air holes in a hexagonal arrangement running the length of the fiber. Light is guided down the center core by the difference in index of refraction between the solid silica core and the air hole cladding. Unlike conventional waveguides, photonic crystal fibers can support anomalous waveguide and net dispersion while remaining single-mode, a property that can be exploited to broaden the spectrum of a 100 fs pulse centered at 800 nm to more than an optical octave [124].

A.4 Locking Electronics

By comparing the optical beatnote frequency to a reference frequency, a signal can be fed back into the optical system to control the offset frequency and the CE phase of the laser

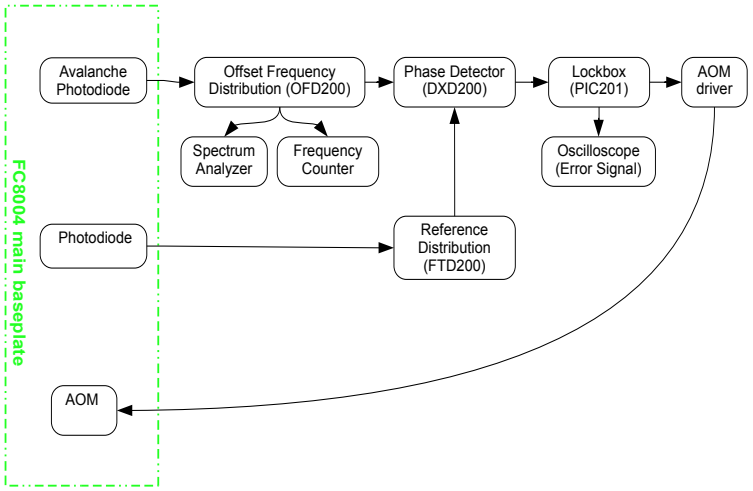

Figure A.5: Schematic of the carrier-envelope phase offset locking electronics.

pulses. This is commonly done by phase locked loops, which allow the transfer of frequency information from one oscillator to another without loss of accuracy.

As discussed above, the beat signal between two lasers,

$$I \propto E_1^2 + E_2^2 + 2E_1E_2 \cos\left((\omega_2 - \omega_1)t + \phi_0\right) \tag{A.8}$$

is detected on a photodiode. Generally speaking, inside the phase detector, the difference between this signal and that from a local oscillator is formed, and the resulting signal is fed back into one of the lasers, closing the loop. The suite of electronics from MenloSystems, GmbH [46] that provides this locking signal is outlined in Figure A.5 and discussed in detail below.

A.4.1 Reference Distribution (FTD200)

In order for the laser oscillator to be phase locked, a reference frequency, i.e. the local oscillator in the phase locked loop, is needed. This signal is derived from the light itself, rather than an external source, because the short-term stability of the laser cavity should be higher than that from an external source. A photodiode detects the mode locked pulse train between 600 nm and 900 nm exiting the PCF, and this 200 MHz signal is fed into the FTD200 Divider unit, which can derive output signals at 1/2, 1/4, 1/8, or 1/16 of the input frequency. By employing the 1/8 output, we obtain the reference frequency at 25 MHz, which is provided to the phase detection unit.

Note: The FC 8004 Optical Frequency Synthesizer manual in the lab [46] does not discuss the FTD200 unit. When the system was delivered, a different Reference Distribution unit, the RFD10, was used. In August 2008, we received several new electronics modules, including the FTD200, a new PIC201 lockbox, and a new DXD200 phase detector. The new electronics were tested, the best options were kept, and the poorer units were returned to MenloSystems. We still have the RFD10 Reference Distribution unit, and it can be used in place of the FTD200. However, the RFD10 unit requires a 10 MHz reference, which can either be supplied by an SRS DG535 or by the mode-locked oscillator pulses themselves (via photodiode and a home-built divide-by 20 circuit). From this 10 MHz signal, the RFD10 derives and delivers 20 MHz reference signals to the other electronics units. With this setup, the offset frequency will be locked to 20 MHz, rather than 25 MHz with the FTD200.

A.4.2 Offset Frequency Distribution (OFD200)

The beatnote signal detected by the avalanche photodiode on the main baseplate is fed directly into an Offset Frequency Distribution (OFD200) box. Here, the signal is passed

through a 150 MHz low-pass filter (to select only beatnotes between modes n and $2n$) followed by a 20 MHz band-pass filter (to select only the $\omega_n - \omega_{2n}$ beatnote). Outputs to a frequency counter and spectrum analyzer are also generated. The spectrum analyzer allows us to monitor the beatnote at 25 MHz and to perform integrated phase jitter analysis, as discussed in Section A.5. A third signal at 25 MHz is fed into the phase detection unit.

A.4.3 Phase Detector (DXD200)

The phase detection unit is the heart of the phase locked loop scheme. Inside this unit is a counter, in which the local oscillator (the 25 MHz signal from the FTD200) counts up and the beat signal counts down. With a range from 0 to 64, the counter is able to monitor a + 32 π phase difference between the two oscillators. A digital to analog converter then regenerates a signal relative to this phase difference, which is supplied to the lockbox.

A.4.4 Lockbox (PIC201)

Formally a proportional integral circuit, the PIC201 lockbox allows the locking mechanism to be turned on or off. Several knobs adjust the coarse-, fine-, and high frequency (HF) amplification of the input signal, and the DC offset knob allows for addition or subtraction of an adjustable offset prior to signal integration. If locking is initiated, the input signal is integrated and then fed through to the acousto-optic modulator driver. When the lock is not engaged, the output signal is determined by a second, adjustable "Offset out" setting, which also determines the starting point if the lock is lost. A red LED indicates the locking status. The error signal is output from the unit and is monitored on an oscilloscope. Typically, the best locks have been attained with coarse gain = 9 and very low HF gain.

A.4.5 Acousto-optic Modulator and Driver

A model ME-405K light modulator signal processor from IntraAction Corp. [126] receives the locking signal from the lockbox and then provides the RF drive power to the acousto-optic modulator (AOM, model AFM-405A1 from IntraAction Corp. [127]) sitting on the main baseplate of the FC 8004. Applying this radio frequency to the AOM modulates the amplitude of Verdi pump laser light via the acousto-optic effect [128]. Variations in pump power manifest themselves in changes in the optical path length inside the Ti:Sapphire crystal due to its optical Kerr effect [54], thus stabilizing the carrier envelope phase. The "level" knob adjusts the CW power level at the output; setting this to 0 generally gives the most stable locks.

A.5 Locking Results

Figure A.6 shows spectrum analyzer (SA) traces of the beatnote for several different frequency spans. From these SA traces we can tell quite a bit about the quality of the lock and the noise present in the system. First of all, on the 20 MHz span (Figure A.6a), the beatnote must be at least 30 dB above the baseline for the locking electronics to function; 40 dB is preferable, and the best contrast achievable is $\sim$50 dB. On the 300 kHz span (Figure A.6e), one will notice sidepeaks at $\pm$100 kHz. The source of these sidepeaks was found to be the Verdi pump laser itself, and their exact frequency depends upon the individual laser used. Harmonics of these sidebands are also visible on the 1 MHz span. Generally speaking, in addition to the maximum peak-to-baseline contrast on the wide span, a well-separated central peak on top of a narrow pedestal when viewed with a 300-500 kHz span (black curve in Figure A.7) gives the greatest lock stability and lowest noise (discussed quantitatively below). The widening of the base, or neck, of the central peak, as illustrated

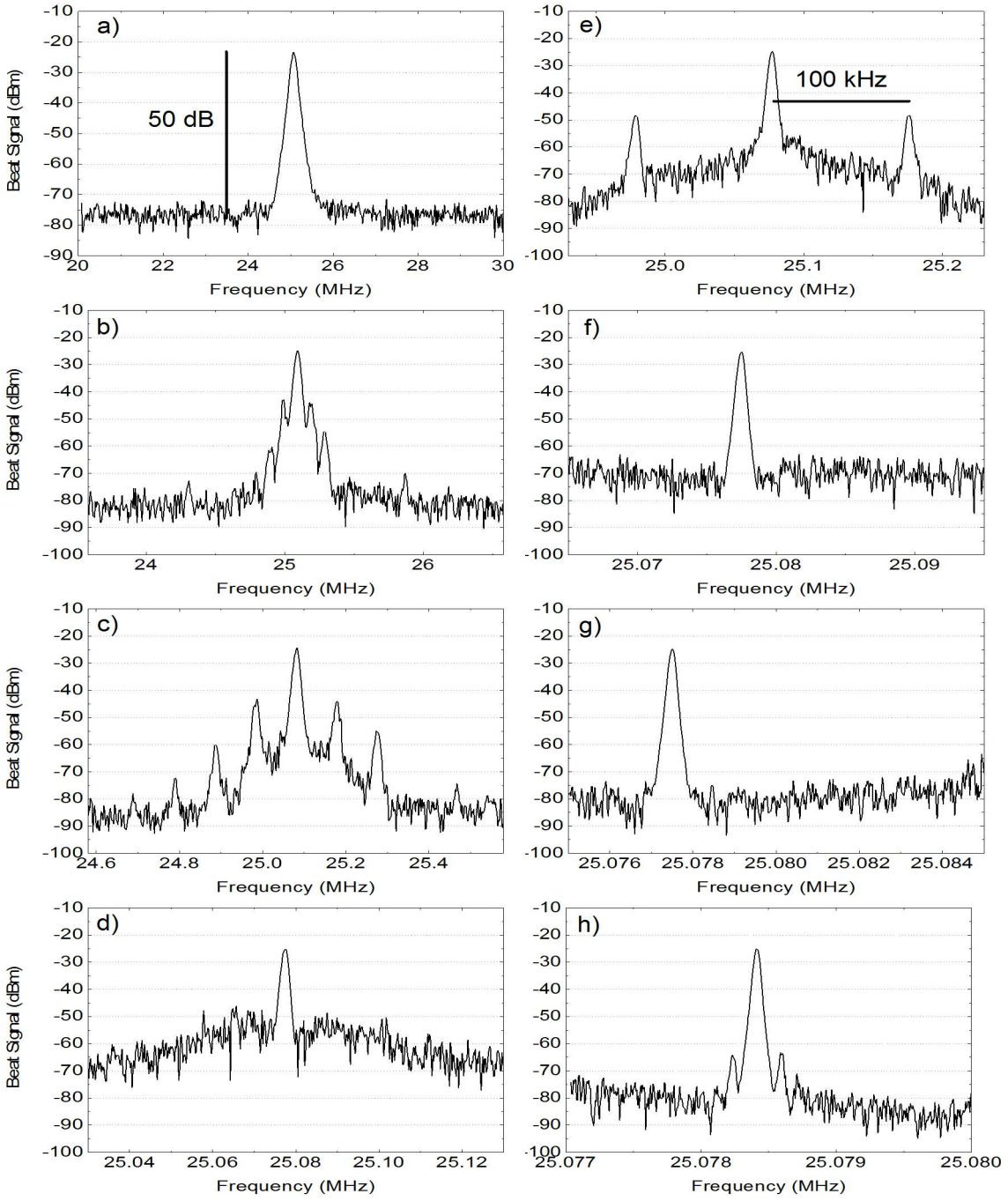

Figure A.6: Spectrum analyzer traces (reconstructed from the oscilloscope files) of the beatnote for a typical lock. Frequency spans (a) 10 MHz; (b) 3 MHz; (c) 1 MHz; (d) 100 kHz; (e) 300 kHz; (f) 30 kHz; (g) 10 kHz; (h) 3 kHz.

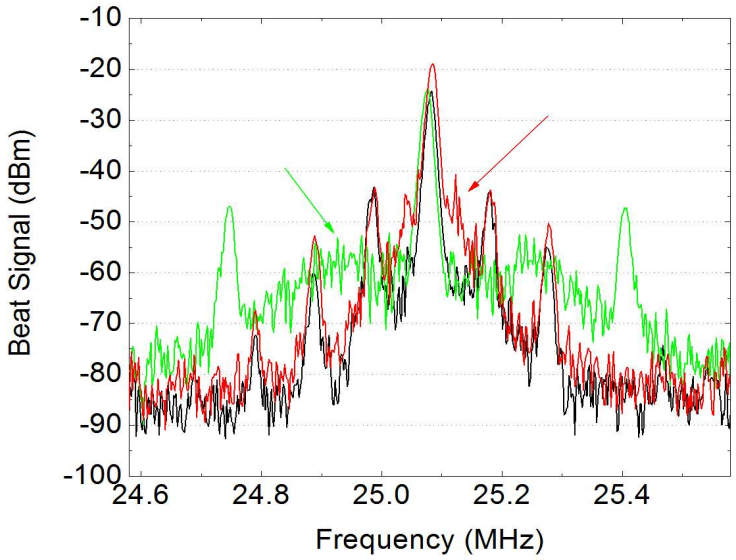

Figure A.7: Spectrum analyzer traces (reconstructed from the oscilloscope files) of the beatnote for three locks. Note the widening of the neck on the red curve and the shrugging of the shoulders on the green curve. The black traces represents the most desirable signal shape.

in the red curve, indicates poorer locking conditions. This can sometimes be improved by adjusting the fine and HF gain pots on the lockbox. Also, the beatnote will often appear to "breathe" or shrug its shoulders, as in the green curve; the reason for this behavior has not been determined, nor has it been effectively compensated.

As a quantitative method of determining the amount of phase noise present in a lock, we use the PhaseNoise analysis program [129] provided to us by MenloSystems. The SA in the lab, a Hewlett Packard 8568B Spectrum Analyzer [130], has no direct method of saving data for analysis, but it is capable of outputting its traces to a pen plotter or oscilloscope. For our purposes, we send these outputs to a Tektronix TDS 3034 digital oscilloscope [131], with which we can save the SA traces to floppy disk. We obtain eight traces of the beatnote, with varying spans, as shown in Figure A.6, which are then used for integration in the

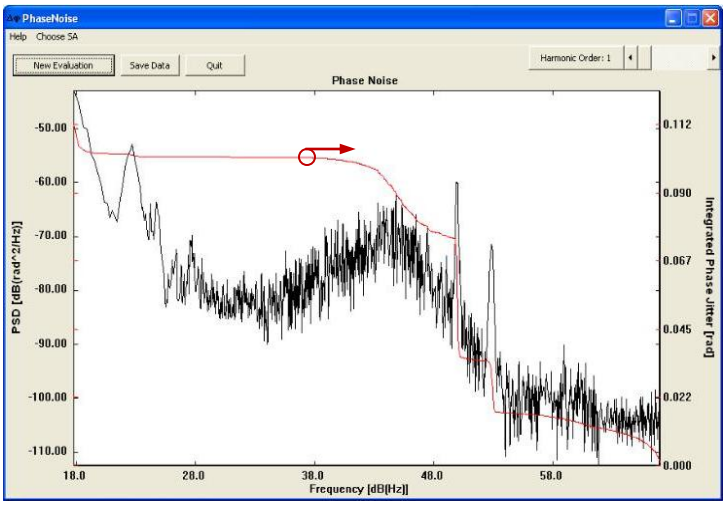

Figure A.8: Screen shot of the PhaseNoise software from MenloSystems. Black curve: power spectral density (PSD); red curve: integrated phase jitter (IPJ).

PhaseNoise program, seen in Figure A.8. Included in the analysis is the power spectral density (PSD), which is a measure of the fluctuations in the optical phase (of the beatnote) at each noise frequency. Two spikes at 50 dB(Hz) and 53 dB(Hz) (Note: Y db(Hz) = 10 $\log_{10} \frac{XHz}{1Hz}$; 50 dB(Hz) = 100 kHz) are due to the Verdi-induced sidepeaks at $\pm$ 100 kHz and $\pm$ 200 kHz. Also calculated is the integrated phase jitter (IPJ), which indicates how much the noise at each frequency contributes to the total jitter in the lock.

Figure A.9 shows the phase noise analysis for three different locks. To date, the lowest IPJ obtained was 100 mrad (Figure A.9b); typical locks with the new electronics, specifically the new PIC201 lockbox, regularly have IPJs of $\leq$ 140 mrad (Figure A.9a), whereas the best IPJ obtained with the old lockbox was approximately 350 mrad. Even with the new electronics, the quality and duration of the locks varies daily. The longest achievable locks are on the order of 3 hours, while the shortest may be less than one minute, if locking is

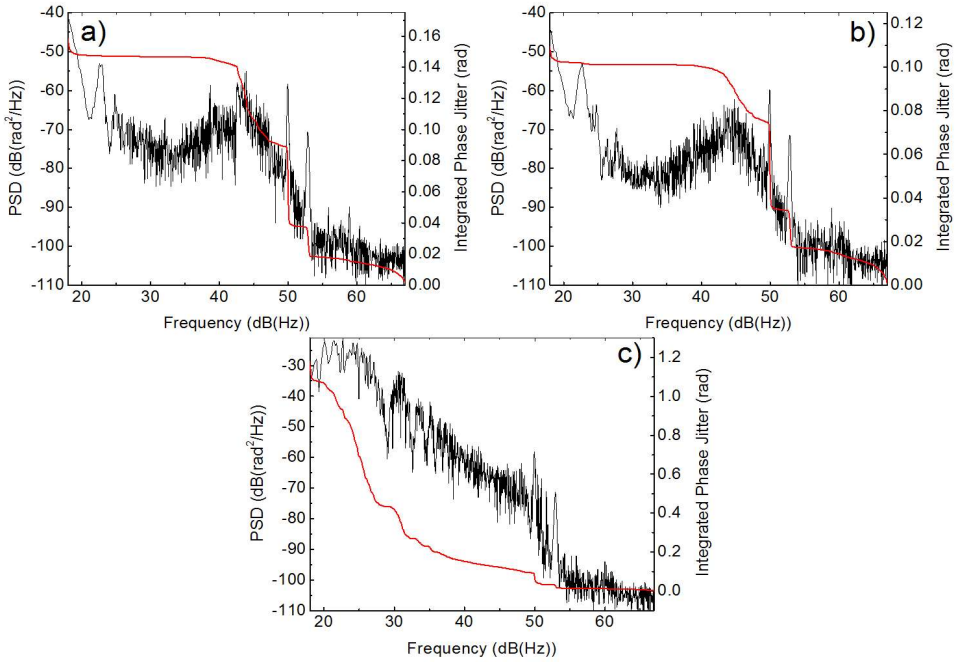

Figure A.9: Phase noise analysis for three locks. (a) A typical lock. (b) The lowest integrated phase jitter observed. (c) Lock with Pockels cell high voltage supply on, switching, and located in close proximity to the locking electronics rack.

even achieved. It is interesting to note that all of the locks represented in Figure A.7 have IPJ values of 120-140 mrad, so even ugly looking beatnotes may give reasonable locks for some amount of time.

The locking electronics are very sensitive to outside noise sources, and several measures have been taken to minimize the phase noise. First, the optical tables in the Chemistry lab sit on pneumatic isolators (support legs incorporating a layer of compressed air) in order to decouple the tables from any building vibrations. Secondly, vibration-dampening Sorbothane® [132] sheets have been placed under the main baseplate of the FC 8004. Additionally, air currents can have negative impacts on the lock stability, so foam weatherstripping was inserted into the gap between the breadboard and the FC8004 walls. It is necessary to keep the unit covered and the plastic curtains surrounding the optical tables closed for additional protection against dust and air currents. Turbo pumps were not found to be a source of noise. In order to reduce electrical noise, all of the locking electronics are plugged into a separate, clean-power outlet, and it is crucial that two photodiodes be used to derive independent signals for phase locking (to the FTD200) and for the master trigger for the Evolution and Pockels cell timing (to the DG535). Pockels cell drivers were found to be a major source of lock instability. Figure A.9c illustrates the phase noise analysis for a lock during which the Pockels cell high voltage supply was located close to the FC 8004 electronics rack; the integrated phase jitter easily surpasses 1 rad, 10 times larger than for average locking conditions. Relocating the high voltage supply further away from the locking electronics resolved this problem.

A.6 Conclusions

In the Chemistry lab, it is currently possible to stabilize the CE phase of the oscillator pulses using the FC 8004 optical frequency synthesizer from MenloSystems. The integrated phase jitter is regularly ≤ 140 mrad, although lock duration varies widely, as long as appropriate precautions are taken to reduce major sources of noise.

Appendix B

Momentum of a Charged Particle in an Oscillating Electric Field

B.1 Introduction

In this Appendix, we derive an expression for the momentum imparted to a charged particle by an oscillating electric field. This is then applied to an electron ionized from an atomic or molecular core, with a discussion of how the subsequent strong field processes are dependent upon the ionized electron's momentum. For further information, see [103, 108].

B.2 Particle in an Oscillating Electric Field

Consider an oscillating electric field (i.e. a laser field) linearly polarized along the $\hat{z}$ direction:

$$\vec{E}(t) = E_0(t) \sin \omega t \hat{z} \tag{B.1}$$

where $E_0(t)$ is the time-dependent field amplitude and ω is the oscillation (laser) frequency. A particle of charge q suddenly placed in this electric field will experience a force

$$\vec{F}(t) = q\vec{E}(t) = qE(t), \tag{B.2}$$

where we eliminate the vector notation and assume that we are always talking about the components along the field polarization. The force is also equal to the mass times the acceleration of the particle,

$$F(t) = ma(t), \tag{B.3}$$

and

$$a(t) = \ddot{x}(t) = \frac{\dot{p}(t)}{m} \tag{B.4}$$

where the *dot* notation refers to the derivative with respect to time. Combining Equations B.1-B.4:

$$\begin{aligned} F(t) &= ma(t) \\ &= m\frac{\dot{p}(t)}{m} \\ &= \dot{p}(t) \\ &= qE(t) \\ \dot{p}(t) &= qE_0(t)\sin(\omega t). \end{aligned} \tag{B.5}$$

Thus, the momentum at time t of a particle with mass m and charge q depends upon the time, t_0, at which it was placed in the electric field. To find $p(t, t_0)$, we integrate Equation B.5

$$p(t,t_0) = \int_{t_0}^{t} F(t')dt' = q\int_{t_0}^{t} E_0(t')\sin\omega t' dt' \tag{B.6}$$

After integration by parts, Equation B.6 becomes

$$p(t,t_0) = -\frac{q}{\omega}\left[E_0(t')\cos\omega t'\right]_{t_0}^{t} + \frac{q}{\omega}\int_{t_0}^{t}\frac{\partial E_0(t')}{\partial t'}\cos\omega t' dt' \tag{B.7}$$

This expression can be simplified by estimating $\partial E_0(t')/\partial t' \approx E_{max}/\tau$ where τ is the pulse duration:

$$p(t,t_0) = -\frac{q}{\omega}\left[E_0(t')\cos\omega t'\right]_{t_0}^{t} + \frac{q}{\omega^2}\frac{E_0}{\tau}\left[\sin\omega t'\right]_{t_0}^{t} \tag{B.8}$$

As long as the pulse duration is much longer than the period of the field oscillation, the standard slowly varying envelope approximation applies, and the second term can be neglected, giving

$$p(t,t_0) = -\frac{q}{\omega}\left[E_0(t)\cos\omega t - E_0(t_0)\cos\omega t_0\right]. \tag{B.9}$$

Here, the first term represents the particle's oscillatory motion in the electric field, which will go to zero when the laser pulse is gone, since $E_0(t) \to 0$ as $t \to \infty$. The second term is the remaining drift momentum imparted to the particle by the oscillating electric field. It is dependent upon the time at which the particle was "born" or liberated in the field:

$$p_{drift}(t_0) = \frac{q}{\omega}E_0(t_0)\cos\omega t_0 \tag{B.10}$$

$$= qA(t_0) \tag{B.11}$$

where $A(t_0)$ is the vector potential at the instant the particle is placed in the field. From Equation B.10, we see that the maximum drift momentum is obtained when the particle is set free at a zero-crossing of the electric field, $\omega t_0 \equiv \phi_0 = 0, 180°$... and

$$p_{max} = \frac{q}{\omega} E_0(t_0) = \frac{q}{\omega} E_{max}. \tag{B.12}$$

B.3 Ionization, Recollision, and Recoil Ion Momentum

Now let us apply this to the specific case of an electron being liberated from its ionic core, either atomic or molecular, by the laser field. When bound to the atom, the electron experiences little effect from the laser. However, upon tunneling from the binding potential, the electron is suddenly placed in the field, where it is "free" to move under the influence of the laser. For very strong fields, to lowest order, one can neglect the field due to the parent ion. This approximation is valid provided $1/R_0^2 \ll E_{max}$, where R_0 is the radial distance at which the electron emerges from the Coulomb + laser potential barrier. For an atom or molecule with ionization potential U_0,

$$R_0 = \frac{U_0}{E_{max}} = U_0 \sqrt{\frac{5.45}{I_0}} \tag{B.13}$$

in a laser field with max intensity I_0, or $R_0 \simeq 10 - 30a_0$ for $I_0 = 10^{14}$ W/cm^2. The time of the first ionization event, t_0, and the recollision time, t_1, should the electron return to the core, dictate the subsequent atomic or molecular processes. If the electron is ionized at a zero-crossing of the electric field, $\phi_0 = 0°$ (blue curve in Figure B.1), then it gains maximum drift momentum and the electron will escape from the region of the ion core, eliminating the possibility of rescattering. Tunnel ionization is most probable at the field maximum, $\phi_0 = 90°$. In this case, the electron gains no drift momentum, and returns to

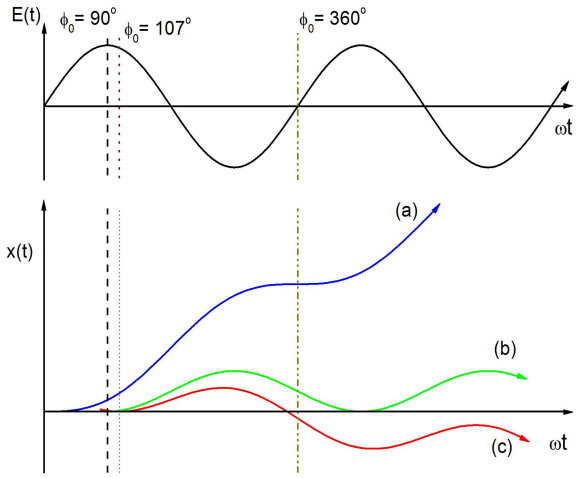

Figure B.1: Trajectories of an electron liberated from the ionic core at different phases, $\omega t_0 = \phi_0$, of an oscillating electric field. See Section B.3.1 for specifics on the calculations.

the ion core with too little energy to initiate further ionization (green curve). Ionization at phases $90° < \phi_0 < 180°$ and $270° < \phi_0 < 360°$ will cause the ionized electron to return to the core with finite momentum; specifically, ionization at $\phi_0 = 107°$ will lead to the maximal electron velocity upon return to the ion core, corresponding to a kinetic energy of $3.17U_p$ [27]. Now, the electron returns to the core near a zero-crossing of the electric field but may have sufficient momentum to liberate another one or more electrons (red curve). This second ionization process can occur immediately through direct ionization (so-called recollision-induced direct ionization (RIDI)), or by exciting one or more electrons that are tunnel ionized during a subsequent field oscillation (so-called recollision-induced excitation plus tunneling (RIET)).

Immediately after the recollision event at time t_1, the momentum of the ion core will be equal and opposite to that of the sum of the departing electrons,

$$p^{+n} = -\sum_{i=1}^{n} p_{e_i} \tag{B.14}$$

where we have assumed (for simplicity) that the ion was at rest at the time of recollision and that all of the first electron's energy was consumed in the instantaneous liberation of the subsequent $n-1$ electrons, i.e. RIDI with no excess electron kinetic energy. (Other ionization mechanisms and the possibility of excess kinetic energy are discussed in [103, 108] and in the following paragraph.) If the recollision occurs near the zero-crossing of the field, from Equation B.10, we know that all of the electrons and the ion will gain the maximum drift momentum. Thus,

$$p_{max}^{+n} = -\sum_{i=1}^{n} p_{e_i} = -\sum_{i=1}^{n} \frac{q_{=-1}}{\omega} E_0(t) \cos \omega t_1 = \frac{n}{\omega} E_{max}. \tag{B.15}$$

Recall that the electric field of the laser pulse can also be expressed in terms of the ponderomotive potential, or the cycle-averaged quiver energy of a free electron in the laser field:

$$U_p = \frac{E^2}{4\omega^2}. \tag{B.16}$$

From this, we can express the maximum momentum obtained by an ion of charge n as

$$p_{max}^{+n} = 2n\sqrt{U_p}. \tag{B.17}$$

This relationship can be used to calculate the laser intensity from the longitudinal momentum distribution of an ion species.

The cutoff momentum, p_{max}^{+n} actually depends upon the difference in the energy of the returning electron and the ionization potential of the remaining $n-1$ electrons. Specifically for nonsequential double ionization, $E_{exc} = \gamma U_p - I_p^+$ where γ is a multiplicative factor and I_p^+ is the ionization potential of the A^+ species. Thus,

$$p_{max}^{+2} = 4\sqrt{U_p} + 2\sqrt{\gamma U_p - I_p^+}. \tag{B.18}$$

For an electron returning with maximal kinetic energy, $\gamma = 3.17$; other theoretical work has suggested $\gamma = 2$ [133]. As a concrete example, for $I = 1.5 \times 10^{14}$ W/cm^2, $\lambda = 800$ nm, $I_p^+ = I_p(Ar^+) = 27.6$ eV $= 1.02$ a.u, and maximum kinetic energy, we find the correction to Equation B.17 $\delta_p = 2\sqrt{3.17U_p - I_p^+} = 0.2$ a.u., or $\delta_p/p_{\|}^{max} = 0.2/2.23 \simeq 9\%$.

B.3.1 Calculation of Electron Trajectories

Recognizing that $a(t) = \dot{v}(t) = \ddot{x}(t)$, we can solve Equation B.3 for $a(t)$ and integrate twice to find the electron's position as a function of time for a given time of birth:

$$\begin{aligned} a(t) &= \frac{F(t)}{m} \\ &= \frac{q}{m}E_(t) \\ a(t) &= \frac{q}{m}E_0(t)\sin\omega t. \end{aligned} \tag{B.19}$$

If we assume that the slowly varying envelope approximation holds, as we did in Equation B.9, then upon integration we get

$$\begin{aligned} v(t,t_0) &= \int_{t_0}^{t} a(t')dt' \\ &= \frac{qE_0}{m}\int_{t_0}^{t}\sin\omega t' dt' \\ v(t,t_0) &= -\frac{qE_0}{m\omega}\left(\cos\omega t - \cos\omega t_0\right) \end{aligned} \tag{B.20}$$

and

$$\begin{aligned} x(t,t_0) &= \int_{t_0}^{t} v(t,t_0)dt' \\ &= -\frac{qE_0}{m\omega}\int_{t_0}^{t}\left(\cos\omega t' - \cos\omega t_0\right)dt' \\ &= -\frac{qE_0}{m\omega^2}\left(\sin\omega t' - \omega t'\cos\omega t_0\right)_{t_0}^{t} \\ x(t,t_0) &= -\frac{qE_0}{m\omega^2}\left(\sin\omega t - \sin\omega t_0 - \omega t\cos\omega t_0 + \omega t_0\cos\omega t_0\right). \end{aligned} \tag{B.21}$$

Equation B.21 is evaluated for several values of ωt_0 and plotted in Figure B.1.

Appendix C

Kinetic Energy Release for all Observed N_2, O_2, and CO Channels

Table C.1: Kinetic Energy Release (KER, eV) for the dissociation channels of N_2, O_2, and CO. All single color data employed a near-IR Ti:Sapph laser, and the two-color experiment employed 400 nm + 800 nm pulses (see Chapter 3). The 8 fs data was estimated from KER vs. delay plots in [115].

Channel	40 fs Single Color UVA	Two Color UVA	5 fs Single Color MPQ	8 fs Single Color [115]
$N_2(1,0)$	1.32	0.8	1.5	2
$N_2(1,1)$	6.6	7		7.5-11
$N_2(1,1)$ main			7.6	
$N_2(1,1)$ upper			10.2	
$N_2(2,0)$	2	3.2	5.56	
$N_2(2,1)$	11	12		17-20
$N_2(2,1)$ main			16.6	
$N_2(2,1)$ upper			21.6	
$N_2(2,2)$	14.8			40-42
$N_2(2,2)$ lower			32.6	
$N_2(2,2)$ upper			39.6	
$N_2(3,1)$	17.8			
$N_2(3,2)$	25.8			
$O_2(1,0)$	1.2			2.7
$O_2(1,1)$	6.8			6-12
$O_2(2,0)$	1.9	2.1	8.9	
$O_2(2,1)$	10.6	9.3		13; 17-24
$O_2(2,1)$ lower			13.3	
$O_2(2,1)$ upper			16.4	
$O_2(3,1)$	17.3			20-35
CO(1,0)	1.4			
CO(0,1)	0.9			
CO(1,1)	5.7			5-7
CO(2,0)	2.9			
CO(0,2)	3	2.3		
CO(1,2)	11.4	11.4		14-17
CO(2,1)	9.8			14-17
CO(2,2)	14.5	15.2		24-27
CO(3,0)	4.2			
CO(3,1)	14.7			
CO(3,2)	19.3			

Bibliography

[1] A. Baltuška, Th. Udem, M. Uiberacker, M. Hentschel, E. Goulielmakis, Ch. Gohle, R. Holzwarth, V. S. Yakovlev, A. Scrinzi, T. W. Hänsch, and F. Krausz. Attosecond control of electronic processes by intense light fields. *Nature*, **421**:611, 2003.

[2] E. Goulielmakis, M. Schultze, M. Hofstetter, V. S. Yakovlev, J. Gagnon, M. Uiberacker, A. L. Aquila, E. M. Gullikson, D. T. Attwood, R. Kienberger, F. Krausz, and U. Kleineberger. Single-Cycle Nonlinear Optics. *Science*, **320**:1614, 2008.

[3] X. Liu, E. Eremina, W. Sander, E. Goulielmakis, K. O. Keeffe, M. Lezius, F. Krausz, F. Lindner, M. G. Schätzel, G. G. Paulus, and H. Walther. Nonsequential Double Ionization at the Single-Optical-Cycle Limit. *Phys. Rev. Lett.*, **93**:263001, 2004.

[4] G. G. Paulus, F. Grasbon, H. Walther, P. Villoresi, M. Nisoli, S. Stagira, E.. Priori, and S. De Silvestri. Absolute-phase phenomena in photoionization with few-cycle laser pulses. *Nature*, **414**:182, 2001.

[5] G. G. Paulus, F. Lindner, H. Walther, A. Baltuška, E. Goulielmakis, M. Lezius, and F. Krausz. Measurement of the Phase of Few-Cycle Laser Pulses. *Phys. Rev. Lett.*, **91**:253004, 2003.

[6] M. F. Kling, Ch. Siedschlag, A. J. Verhoef, J. I. Khan, M. Schultze, Th. Uphues, Y. Ni, M. Uiberacker, M. Drescher, F. Krausz, and M. J. J. Vrakking. Control of Electron Localization in Molecular Dissociation. *Science*, **312**:246, 2006.

[7] M. F. Kling, Ch. Siedschlag, I. Znakovskaya, A. J. Verhoef, S. Zherebtsov, F. Krausz, M. Lezius, and M. J. J. Vrakking. Strong-field control of electron localisation during molecular dissociation. *Mol. Phys.*, **106**:455, 2008.

[8] M. Kremer, B. Fischer, B. Feuerstein, V. L. B. de Jesus, V. Sharma, C. Hofrichter, A. Rudenko, U. Thumm, C. D. Schröter, R. Moshammer, and J. Ullrich. Electron Localization in Molecular Fragmentation of H_2 by Carrier-Envelope Phase Stabilized Laser Pulses. *Phys. Rev. Lett.*, **103**:213003, 2009.

[9] I. Znakovskaya, P. von den Hoff, S. Zherebtsov, A. Wirth, O. Herrwerth, M. J. J. Vrakking, R. de Vivie-Riedle, and M. F. Kling. Attosecond Control of Electron Dynamics in Carbon Monoxide. *Phys. Rev. Lett.*, **103**:103002, 2009.

[10] H. G. Muller, P. H. Bucksbaum, D. W. Schumacher, and A. Zavriyev. Above-threshold ionisation with a two-colour laser field. *J. Phys B*, **23**:2761, 1990.

[11] K. J. Schafer and K. C. Kulander. Phase-dependent effects in multiphoton ionization induced by a laser field and its second harmonic. *Phys. Rev. A*, **45**:8026, 1992.

[12] N. Dudovich, O. Smirnova, J. Levesque, Y. Mairesse, M. Yu. Ivanov, D. M. Villeneuve, and P. B. Corkum. Measuring and controlling the birth of attosecond XUV pulses. *Nature Phys.*, **2**:781, 2006.

[13] H. Niikura, N. Dudovich, D. M. Villeneuve, and P. B. Corkum. Mapping Molecular Orbital Symmetry on High-Order Harmonic Generation Spectrum Using Two-Color Laser Fields. *Phys. Rev. Lett.*, **105**:053003, 2010.

[14] B. Sheehy, B. Walker, and L. F. DiMauro. Phase Control in the Two-Color Photodissociation of HD^+. *Phys. Rev. Lett.*, **74**:4799, 1995.

[15] M. R. Thompson, M. K. Thomas, P. F. Taday, J. H. Posthumus, A. J. Langley, L. J. Frasinski, and K. Codling. One and two-color studies of the dissociative ionization and Coulomb explosion of H_2 with intense Ti:sapphire laser pulses. *J. Phys. B*, **30**:5755, 2001.

[16] D. Ray, F. He, S. De, W. Cao, H. Mashiko, P. Ranitovic, K. P. Singh, I. Znakovskaya, U. Thumm, G. G. Paulus, M. F. Kling, I. V. Litvinyuk, and C. L. Cocke. Ion-Energy Dependence of Asymmetric Dissociation of D_2 by a Two-Color Laser Field. *Phys. Rev. Lett.*, **103**:223201, 2009.

[17] E. Charron, A. Giusti-Suzor, and F. H. Mies. Two-color coherent control of H_2^+ photodissociation in intense laser fields. *Phys. Rev. Lett.*, **71**:692, 1993.

[18] E. Charron, A. Giusti-Suzor, and F. H. Mies. Coherent control of photodissociation in intense laser fields. *J. Chem. Phys.*, **103**:7359, 1995.

[19] H. Ohmura, T. Nakanaga, and M. Tachiya. Coherent Control of Photofragment Separation in the Dissociative Ionization of IBr. *Phys. Rev. Lett.*, **92**:113002, 2004.

[20] H. Ohmura, N. Saito, and M. Tachiya. Selective Ionization of Oriented Nonpolar Molecules with Asymmetric Structure by Phase-Controlled Two-Color Laser Fields. *Phys. Rev. Lett.*, **96**:173001, 2006.

[21] S. De, I. Znakovskaya, D. Ray, F. Anis, Nora G. Johnson, I. A. Bocharova, M. Magrakvelidze, B. D. Esry, C. L. Cocke, I. Litvinyuk, and M. F. Kling. Field-Free Orientation of CO Molecules by Femtosecond Two-Color Laser Fields. *Phys. Rev. Lett.*, **103**:153002, 2009.

[22] T. Kanai and H. Sakai. Numerical simulations of molecular orientation using strong, nonresonant, two-color laser fields. *J. Chem. Phys.*, **115**:5492, 2001.

[23] A. D. Bandrauk and S. Chelkowski. Asymmetric Electron-Nuclear Dynamics in Two-Color Laser Fields: Laser Phase Directional Control of Photofragments in H_2^+. *Phys. Rev. Lett.*, **84**:3562, 2000.

[24] S. Chelkowski, M. Zamojski, and A. D. Bandrauk. Laser-phase directional control of photofragments in dissociative ionization of H_2^+ using two-color intense laser pulses. *Phys. Rev. A*, **63**:023409, 2001.

[25] M. V. Ammosov, N. B. Delone, and V. P. Kraĭnove. Tunnel ionization of complex atoms and of atomic ions in an alternating electromagnetic field. *Sov. Phys. JETP*, **64**:1191, 1986.

[26] L. V. Keldysh. Ionization in the field of a strong electromagnetic wave. *Sov. Phys. JETP*, **20**:1037, 1965.

[27] P. B. Corkum. Plasma Perspective on Strong-Field Multiphoton Ionization. *Phys. Rev. Lett.*, **71**:1994, 1993.

[28] B. A. Sickmiller. *High Harmonic Generation from Transiently Aligned Molecules in a Hollow-core Waveguide*. PhD thesis, University of Virginia, 2008.

[29] P. Agostini, F. Fabre, G. Mainfray, G. Petite, and N. K. Rahman. Free-Free Transitions Following Six-Photon Ionization of Xenon Atoms. *Phys. Rev. Lett.*, **42**:1127, 1979.

[30] B. Yang, K. J. Schafer, B. Walker, K. C. Kulander, P. Agostini, and L. F. DiMauro. Intensity-Dependent Scattering Rings in High Order Above-threshold Ionization. *Phys. Rev. Lett.*, **71**:3770, 1993.

[31] G. G. Paulus, W. Nicklich, H. Xu, P. Lambropoulos, and H. Walther. Plateau in Above Threshold Ionization Spectra. *Phys. Rev. Lett.*, **72**:2851, 1994.

[32] W. Becker, F. Grasbon, R. Kopold, D. B. Miloševič, G. G. Paulus, and H. Walther. Above-threshold ionization: From classical features to quantum effects. *Advances in Atomic, Molecular, and Optical Physics*, **48**:35, 2002.

[33] A. l'Huillier, L. A. Lompre, G. Mainfray, and C. Manus. Multiply Charged Ions Formed by Multiphoton Absorption Processes in the Continuum. *Phys. Rev. Lett.*, **48**:1814, 1982.

[34] A. l'Huillier, A. Lompre, G. Mainfray, and C. Manus. Multiply charged ions induced by multiphoton absorption in rare gases at 0.53 μm. *Phys. Rev. A*, **27**:2503, 1983.

[35] K. C. Kulander, J. Cooper, and K. J. Schafer. Laser-assisted inelastic rescattering during above-threshold ionization. *Phys. Rev. A*, **51**:561, 1995.

[36] M. J. DeWitt, E. Wells, and R. R. Jones. Ratiometric Comparison of Intense Field Ionization of Atoms and Diatomic Molecules. *Phys. Rev. Lett.*, **87**:153001, 2001.

[37] L. J. Frasinkski, K. Codling, P. Hatherly, J. Barr, I. N. Ross, and W. T. Toner. Femtosecond Dynamics of Multielectron Dissociative Ionization by Use of Picosecond Laser. *Phys. Rev. Lett.*, **58**:2424, 1987.

[38] T. Seideman, M. Y. Ivanov, and P. B. Corkum. Role of Electron Localization in Intense-Field Molecular Ionization. *Phys. Rev. Lett.*, **75**:2819, 1995.

[39] S. Chelkowski and A. D. Bandrauk. Two-step Coulomb explosions of diatoms in intense laser fields. *J. Phys. B*, **28**:L723, 1995.

[40] E. Constant, H. Stapelfeldt, and P. B. Corkum. Observation of Enhanced Ionization of Molecular Ions in Intense Laser Fields. *Phys. Rev. Lett.*, **76**:4140, 1996.

[41] D. Strickland and G. Mourou. Compression of Amplified Chirped Optical Pulses. *Opt. Comm.*, **56**:219, (1985).

[42] Coherent, Santa Clara, CA. *Operator's Manual Verdi^{TM} V-2/V-5/V-6 Diode-Pumped Lasers*, 2005.

[43] Positive Light, Inc., Los Gatos, CA. *Evolution-30 User Manual*, 2001.

[44] Stanford Research Systems, Sunnyvale, CA. *Model DG535 Digital Delay/Pulse Generator*, 2000.

[45] FEMTOLASERS Productions GmbH, Vienna, Austria. *User's manual for FEMTOSOURCE Scientific Special Version 200MHz*, 2007.

[46] MenloSystems GmbH, Munich, Germany. *FC 8004 Optical Frequency Synthesizer*, 2007.

[47] Kapteyn-Murnane Laboratories, L.L.C., Boulder, CO. *Stretcher-Compressor Manual*, 2001.

[48] B. E. A. Saleh and M. C. Teich. *Fundamentals of Photonics*. Wiley, 1991.

[49] FEMTOLASERS Produktions GmbH, Vienna, Austria. *FEMTOPOWER compact pro Femtosecond Multi-pass Amplifier User's Manual Version V 3.2*, 2007.

[50] Photonics Industries International, Inc., Bohemia, NY. *DM Series High Power IR and Green Lasers Nd:YLF and Nd:YAG*, 2010.

[51] M. Nisoli, S. De Silvestri, and O. Svelto. Generation of high energy 10 fs pulses by a new pulse compression technique. *Appl. Phys. Lett.*, **68**:2793, (1996).

[52] TEM Messtechnik GmbH, Hannover, Germany. *Beamlock 2D/4D*, 2007.

[53] Ocean Optics, 2011. www.oceanopics.com.

[54] J.-C. Diels and W. Rudolph. *Ultrashort Laser Pulse Phenomena*. Academic Press, Inc., 1996.

[55] R. Trebino, K. W. DeLong, D. N. Fittinghoff, J. N. Sweetser, M. A. Krumbugel, B. A. Richman, and D. J. Kane. Measuring Ultrashort Laser Pulses in the Time-Frequency Domain Using Frequency-Resolved Optical Gating. *Rev. Sci. Inst.*, **68**:3277, (1997).

[56] Spiricon, Inc., Logan, UT. *Operator's Manual PC Laser Beam Analyzer Model LBA-PC Series*, 2000.

[57] Femtosoft Technologies. FROG version 3.05, 2000.

[58] Varian Vacuum Technologies, Torino, Italy. *Dual stage Rotary Vane Pumps Instruction Manual*, 1999.

[59] Varian Vacuum Products, Torino, Italy. *Turbo-V 1000HT Pumps Instruction Manual*, 1997.

[60] Varian Vacuum Products, Torino, Italy. *Turbo-V 1000HT Controller Instruction Manual*, 1998.

[61] Varian Vacuum Technologies, Lexington, MA. *Small Aluminum Block Valves Instruction Manual*, 2001.

[62] Varian Vacuum Products, Lexington, MA. *senTorr Gauge Controller Instruction Manual*, 1997.

[63] Varian Vacuum Technologies, Lexington, MA. *580 Nude Ionization Gauge Instruction Manual*, 1999.

[64] Stanford Research Systems, Sunnyvale, CA. *Models RGA100, RGA200, and RGA300 Residual Gas Analyzer Operating Manual and Programming Reference*, 1999.

[65] R. Dörner, V. Mergel, O. Jagutzki, L. Spielberger, J. Ullrich, R. Moshammer, and H. Schmidt-Böcking. Cold Target Recoil Ion Momentum Spectroscopy: a 'momentum microscope' to view atomic collision dynamics. *Physics Reports*, **330**:95, 2000.

[66] F. B. Dunning and R. G. Hulet, editors. *Atomic, Molecular, and Optical Physics: Atoms and Molecules*. Academic Press, 1996.

[67] W. C. Wiley and I. H. McLaren. Time-of-Flight Mass Spectrometer with Improved Resolution. *Rev. Sci. Inst.*, **26**:1150, 1955.

[68] M. B. Williams. *A Photon Counting Imaging Detector using MCPs with Delay Line Readout*. PhD thesis, University of Virginia, 1990.

[69] Stanford Research Systems, Sunnyvale, CA. *Fast Gated Integrators and Boxcar Averagers*, 1993.

[70] T. Wittmann, B. Horvath, W. Helml, M. B. Schätzel, X. Gu, A. L. Cavalier, G. G. Paulus, and R. Kienberger. Single-shot carrier-envelope phase measurement of few-cycle laser pulses. *Nature Physics*, **5**:357, 2009.

[71] Ortec, Oak Ridge, TN. *Model 935 Quad Constant-Fraction 200-MHz Discriminator*, Manual Revision G.

[72] Phillips Scientific, Ramsey, NJ. *NIM Model 794 Quad Gate/Delay Generator*, 1996.

[73] Phillips Scientific, Ramsey, NJ. *NIM Model 752 Quad Two-Fold Logic Unit*, 1996.

[74] RoentDek Handels GmbH, Kelkheim-Ruppertshain, Germany. *CoboldPC User Manual Version 6.0.1.8 B77.*

[75] CAEN, Viareggio, Italy. *Mod. V1290-VX1290 A/N, 32/16 C. Multihit TDC*, 2009.

[76] CAEN, Viareggio, Italy. *Mod. V785, 16.32 Channel Peak Sensing ADC*, 2007.

[77] J. Hoffmann, N. Kurz, and M. Richter. TRIVA 5, VME Trigger Module, 2009.

[78] H. G. Essel and N. Kurz. GSI Multi-Branch System User Manual, 2003.

[79] C. Conover. TakeData Version 1.0 C++, 2001. computer program.

[80] J. Adamczewski-Musch, M. Al-Turany, D. Bertini, H.G. Essel, and S. Linev. The Go4 Analysis Framework Introduction V3.4, 2008.

[81] R. Brun and F. Rademakers. ROOT - An object oriented data analysis framework. *Nucl. Instrum. Meth. A*, **389**:81, 1997.

[82] C. Chen, Y. Y. Yin, and D. S. Elliott. Interference between optical transitions. *Phys. Rev. Lett.*, **64**:507, 1990.

[83] A. de Bohan, P. Antoine, D. B. Milošević, and B. Piraux. Phase-Dependent Harmonic Emission with Ultrashort Laser Pulses. *Phys. Rev. Lett.*, **81**:1837, 1998.

[84] M. Kremer, B. Fischer, B. Feuerstein, V. L. B. de Jesus, V. Sharma, C. Hofrichter, A. Rudenko, U. Thumm, C. D. Schröter, R. Moshammer, and J. Ullrich. Electron Localization in Molecular Fragmentation of H_2 by Carrier-Enevelope Phase Stabilized Laser Pulses. *Phys. Rev. Lett.*, **103**:213003, 2009.

[85] D. Ray, F. He, S. De, W. Cao, H. Mashiko, P. Ranitovic, K. P. Singh, I. Znakovskaya, U. Thumm, G. G. Paulus, M. F. Kling, I. V. Litvinyuk, and C. L. Cocke, 2010. Private Communication.

[86] D. W. Pinkham. *Ultrafast Control of the Dynamics of Diatomic Molecules.* PhD thesis, University of Virginia, 2008.

[87] H. Ohmura, N. Saito, H. Nonaka, and S. Ichimura. Dissociative ionization of a large molecule studied by intense phase-controlled laser fields. *Phys. Rev. A*, **77**:053405, 2008.

[88] D. W. Pinkham and R. R. Jones. Intense laser ionization of transiently aligned CO. *Phys. Rev. A*, **72**:023418, 2005.

[89] G. Lagmago Kamta and A. D. Bandrauk. Effects of molecular symmetry on enhanced ionization by intense laser pulses. *Phys. Rev. A*, **75**:041401(R), 2007.

[90] T. Zuo and A. D. Bandrauk. Phase control of molecular ionization: H_2^+ and H_3^{2+} in intense two-color laser fields. *Phys. Rev. A*, **54**:3254, 1996.

[91] G. Lagmago Kamta and A. D. Bandrauk. Nonsymmetric molecules driven by intense few-cycle laser pulses: Phase and orientation dependence of enhanced ionization. *Phys. Rev. A*, **76**:053409, 2007.

[92] J. P. Nibarger, S. V. Menon, and G. N. Gibson. Comprehensive analysis of strong-field ionization and dissociation of diatomic nitrogen. *Phys. Rev. A*, **63**:053406, 2001.

[93] D. Ray, F. He, S. De, W. Cao, H. Mashiko, P. Ranitovic, K. P. Singh, I. Znakovskaya, U. Thumm, G. G. Paulus, M. F. Kling, I. V. Litvinyuk, and C. L. Cocke, 2011. Private Communication.

[94] R. Dörner, 2011. Private Communication.

[95] C. Li, E. Moon, H. Wang, H. Mashiko, C. M. Nakamura, J. Tackett, and Z. Chang. Determining the phase-energy coupling coefficient in carrier-envelope phase measurements. *Opt. Lett.*, **32**:796, 2007.

[96] N. G. Johnson, O. Herrwerth, A. Wirth, S. De, I. Ben-Itzhak, M. Lezius, B. Bergues, M.F. Kling, A. Senftleben, C. D. Schröter, R. Moshammer, J. Ullrich, K. J. Betsch, R. R. Jones, A. M. Sayler, T. Rathje, K. Rühle, W. Müller, and G. G. Paulus. Single-shot carrier-envelope-phase-tagged ion-momentum imaging of nonsequential double ionization of argon in intense 4-fs laser fields. *Phys. Rev. A*, **83**:013412, 2011.

[97] S. Micheau, Z. Chen, A.-T. Le, and C. D. Lin. Quantitative rescattering theory for nonsequential double ionization of atoms by intese laser pulses. *Phys. Rev. A*, **79**:013417, 2009.

[98] M. F. Kling, J. Rauschenberger, A. J. Verhoef, E. Hasović, T. Uphues, D. B. Milošević, H. G. Muller, and M. J. J. Vrakking. Imaging of carrier-envelope phase effects in above-threshold ionization with intense few-cycle laser fields. *New J. Phys.*, **10**:025024, 2008.

[99] Z. Chen, T. Wittmann, B. Horvath, and C. D. Lin. Complete real-time temporal waveform characterization of single-shot few-cycle laser pulses. *Phys. Rev. A*, **80**:061402(R), 2009.

[100] A. M Sayler, T. Rathje, W. Müller, K. Rühle, R. Kienberger, and G. G. Paulus. Precise, real-time, every-single-shot, carrier-envelope phase measurement of ultrashort laser pulses. *Opt. Lett.*, **36**:1, 2011.

[101] G. G. Paulus, A. M. Sayler, T. Rathje, and W. Müller, May 5, 2005. German patent pending 10-2010-019-814.5.

[102] F. Lindner, G. G. Paulus, H. Walther, A. Baltuška, E. Goulielmakis, M. Lezius, and F. Krausz. Gouy Phase Shift for Few-Cycle Laser Pulses. *Phys. Rev. Lett.*, **92**:113001, 2004.

[103] A. Rudenko, K. Zrost, V. L. B. de Jesus, C. D. Schröter, R. Moshammer, and J. Ullrich. Correlated Multielectron Dynamics in Ultrafast Laser Pulse Interactions with Atoms. *Phys. Rev. Lett.*, **93**:253001, 2004.

[104] O. Herrwerth, A. Rudenko, M. Kremer, V. L. B. de Jesus, B. Fischer, G. Gademann, K. Simeonidis, A. Achtelik, Th. Ergler, B. Feuerstein, C. D. Schröter, R. Moshammer, and J. Ullrich. Wavelength dependence of sub-laser-cycle few-electron dynamics in strong-field multiple ionization. *New J. Phys.*, **10**:025007, 2008.

[105] S. Micheau, Z. Chen, A.-T. Le, and C. D. Lin. Quantitative rescattering theory for nonsequential double ionization of atoms by intense laser pulses. *Phys. Rev. A*, **79**:013417, 2009.

[106] A.-J. Verhoef, A. Fernández, M. Lezius, K. O'Keeffe, M. Uiberacker, and F. Krausz. Few-cycle carrier-envelope phase-dependent stereo detection of electrons. *Opt. Lett.*, **31**:3520, 2006.

[107] J. Rauschenberger, T. Fuji, M. Hentschel, A.-J. Verhoef, T. Udem, C. Gohle, T. W. Hänsch, and F. Krausz. Carrier-envelope phase-stabilized amplifier system. *Laser Phys. Lett.*, **3**:37, 2006.

[108] B. Feuerstein, R. Moshammer, and J. Ullrich. Nonsequential multiple ionization in intense laser pulses: interpretation of ion momentum distributions within the classical 'rescattering' model. *J. Phys. B*, **33**:L823, 2000.

[109] Y. Liu, D. Ye, J. Liu, A. Rudenko, S. Tschuch, M. Dürr, M. Siegel, U. Morgner, Q. Gong, R. Moshammer, and J. Ullrich. Multiphoton Double Ionization of Ar and Ne Close to Threshold. *Phys. Rev. Lett.*, **104**:173002, 2010.

[110] A. S. Alnaser, D. Comtois, A. T. Hasan, D. M. Villeneuve, J.-C. Kieffer, and I. V. Litvinyuk. Strong-field non-sequential double ionization: wavelength dependence of ion momentum distributions for neon and argon. *J. Phys. B*, **41**:031001, 2008.

[111] H. Rottke, X. Liu, E. Eremina, W. Sander, E. Goulielmakis, K. O. Keeffe, M. Lezius, F. Krausz, F. Lindner, Schätzel, G. G. Paulus, and H. Walther. Non-sequential double

ionization in a few-cycle laser pulse: the influence of the carrier-envelope phase. *J. Mod. Optics*, **53**:149, 2006.

[112] K. Zrost, A. Rudenko, Th. Ergler, B. Feuerstein, V. L. B. de Jesus, C. D. Schröter, R. Moshammer, and J. Ullrich. Multiple ionization of Ne and Ar by intense 25 fs laser pulses: few-electron dynamics studied with ion momentum spectroscopy. *J. Phys. B.*, **39**:S371, 2006.

[113] K. J. Betsch, D. W. Pinkham, and R. R. Jones. Directional Emission of Multiply Charged ions During Dissociative Ionization in Asymmetric Two-Color Laser Fields. *Phys. Rev. Lett.*, **105**:223002, 2010.

[114] J. H. Posthumus, A. J. Giles, M. R. Thompson, and K. Codling. Field-Ionization, Coulomb Explosion of diatomic molecules in intense laser fields. *J. Phys. B*, **29**:5811, 1996.

[115] I. A. Bocharova, A. S. Alnaser, U. Thumm, T. Niederhausen, D. Ray, C. L. Cocke, and I. V. Litvinyuk. Time-resoloved Coulomb explosion imaging of nulcear wave-packet dynamics induced in diatomic molecules by intense few-cycle laser pulses. *Phys. Rev. A*, **83**:013417, 2011.

[116] I. A. Bocharova. *Laser Coulomb Explosion Imaging of Molecular Dynamics*. PhD thesis, Kansas State University, 2009.

[117] E. Baldit, S. Saugout, and C. Cornaggia. Coulomb explosion of N_2 using intense 10- and 40-fs laser pulses. *Phys. Rev. A*, **71**:021403(R), 2005.

[118] K. Codling, L. J. Fraskinski, and P. A. Hatherly. On the field ionisation of diatomic molecules by intense laser fields. *J. Phys. B*, **22**:L321, 1989.

[119] T. Zuo and A. D. Bandrauk. Charge-resonance-enhanced ionization of diatomic molecular ions by intense lasers. *Phys. Rev. A*, **52**:R2511, 1995.

[120] L. D. Landau and E. M. Lifschitz. *Mechanics*. Oxford, 1976.

[121] Optical Frequency Synthesizer FC8004 Data Sheet, 2009. www.menlosystems.com.

[122] J. C. Knight, T. A. Birks, P. St. J. Russell, and D. M. Atkin. All-Silica Single-Mode Optical Fiber with Photonic Crystal Cladding. *Opt. Lett.*, **21**:1547, (1996).

[123] M. J. Gander, R. McBride, J. D. C. Jones, D. Mogilevstev, T. A. Birks, J. C. Knight, and P. St. J. Russell. Experimental Measurement of Group Velocity Dispersion in Photonic Crystal Fibre. *Electron. Lett.*, **35**:63, (1999).

[124] J. K. Ranka, R. S. Windeler, and A. J. Stentz. Visible Continuum Generation in Air-Silica Microstructure Optical Fibers with Anomalous Dispersion at 800 nm. *Opt. Lett.*, **25**:25, (2000).

[125] W. J. Wadsworth, J. C. Knight, A. Ortigosa-Blanc, J. Arriaga, E. Silvestre, and P. St. J. Russell. Soliton Effects in Photonic Crystal Fibres at 850 nm. *Electron. Lett.*, **36**:53, (2000).

[126] IntraAction Corp., Bellwood, IL. *Model ME-405K Light Modulator Signal Processor Instruction Manual*, 2007.

[127] IntraAction Corp., Bellwood, IL. *Model AFT-405A1 Acousto-optic Modulator Instruction Manual*, 2007.

[128] A. Yariv. *Optical Electronics*. Holt, Rinehart and Winston, 1985.

[129] Menlo Systems. PhaseNoise Version 1.6, 2008. Computer Program.

[130] Hewlett Packard, Rohnert Park, CA. *8568B Spectrum Analyzer 100 Hz - 1.5 GHz Operating and Programming Manual*.

[131] Tektronix, Inc., Wilsonville, OR. *TDS3000 Series Digital Phosphor Oscilloscopes User Manual*, 1984.

[132] Inc. Sorbothane, 2011. www.sorbothane.com.

[133] A. Becker and F. H. M. Faisal. Interpretation of Momentum Distribution of Recoil Ions from Laser Induced Nonsequential Double Ionization. *Phys. Rev. Lett.*, **84**:3546, 2000.